Investigation and Utilization of Molybdenum Disulfide as Decoupling Layer on Au(111)

NILS KRANE

Dissertation
zur Erlangung des Grades eines
Doktors der Naturwissenschaften

am Fachbereich Physik
der Freien Universität Berlin

August 2019

Diese Arbeit entstand in der Arbeitsgruppe von Prof. Dr. Katharina J. Franke am Fachbereich Physik der Freien Universtät Berlin.

Berlin, der 09.08.2019

Erstgutachterin: Prof. Dr. Katharina J. Franke

Zweitgutachter: Prof. Dr. Martin Weinelt

Tag der Disputation: 02. Dezember 2019

Abstract

This thesis describes the investigation of the MoS_2/Au(111) interface and its decoupling properties for molecular adsorbates by means of scanning tunneling microscopy (STM) and atomic force microscopy (AFM).

In the first part, we grow single-layer MoS_2 on a Au(111) substrate and investigate its structural and electronic properties. Using STM and AFM, we can distinguish between three different sites of the MoS_2/Au(111) moiré pattern and assign each of them to a certain stacking pattern of the MoS_2/Au(111) interface. We observe a certain orientation of the MoS_2 islands with respect to the underlying Au layers. The electronic properties are probed by scanning tunneling spectroscopy (STS). These spectra reveal a strong hybridization of MoS_2 with the Au(111) surface with the most pronounced effect occurring at the $\bar{\Gamma}$ point of the valence band. By measuring the decay constant of the tunneling current, we find an unoccupied state of MoS_2 around the $\bar{\Gamma}$ point 0.4 eV above the conduction band minimum. This state occurs most probably due to the MoS_2/Au(111) interface. Under certain growth conditions, we can produce nanometer-sized vacancy islands below the MoS_2. Here, the hybridization with the Au(111) substrate is lifted, causing a patch of nearly unperturbed single-layer MoS_2. In combination with electroluminescence measurements we find a vanishing density of state within the electronic band gap of quasi freestanding MoS_2.

In the second part 2,5-bis(3-dodecylthiophen-2-yl)thieno[3,2-b]-thiophene (BTTT) molecules are deposited on the MoS_2/Au(111) sample and investigated by STS measurements. We observe excellent decoupling properties of MoS_2 yielding an energy resolution of less then 6 meV. This allows us to resolve a variety of vibronic states in the positive ion resonance (PIR) of BTTT. These vibronic fingerprints enable us to distinguish between rotational isomers of the BTTT molecule, which differ by the rotation of a single thienothiophene group. Density functional theory (DFT) calculations are performed, which fully reproduce the observed vibronic spectra in accordance to the Franck-Condon principle. In the last section, we utilize the high energy resolution to investigate the perturbation potential of different STM tips, acting on the electronic states of the delocalized BTTT molecule. The effect of the inhomogeneous potential distribution in the junction is qualitatively reproduced by a simple electrostatic model of the double barrier junction. By comparing the energy shift of elastic and inelastic resonances of the PIR, we are able to disentangle the perturbation potential of a dipolar tip and the applied voltage.

Kurzfassung

Diese Dissertation beschreibt die Untersuchungen von der MoS_2/Au(111) Grenzfläche sowie ihren entkoppelnden Eigenschaften für molekulare Adsorbate mittels Rastertunnel- (RTM) und Rasterkraftmikroskopie (RKM).

Im ersten Teil wachsen wir eine Monolage MoS_2 auf einer Au(111) Oberfläche und untersuchen ihre strukturellen and elektronischen Eigenschaften. Mit Hilfe von RTM und RKM können wir zwischen drei verschiedenen Bereichen im MoS_2/Au(111) Moiré-Muster unterscheiden und diese dann verschiedenen Stapelfolgen an der MoS_2/Au(111) Grenzfläche zuordnen. Wir beobachten des Weiteren auch eine bestimmte Orientierung der MoS_2 Inseln zu den unterliegenden Au Lagen. Die elektronischen Eigenschaften von MoS_2/Au(111) werden dann mit Rastertunnelspektroskopie (RTS) untersucht. Die Spektren weisen auf eine starke Hybridisierung zwischen dem MoS_2 und der Au(111) Oberfläche hin, wobei der stärkste Effekt am $\bar{\Gamma}$ Punkt des Valenzbandes auftritt. Messungen der Abklingkonstante des Tunnelstroms zeigen einen unbesetzten Zustand des MoS_2 am $\bar{\Gamma}$ Punkt, der etwa 0.4 eV oberhalb des Leitungsbandminimums ist und wahrscheinlich durch die MoS_2/Au(111) Grenzfläche entsteht. Unter bestimmten Präparationsbedingungen können wir nanometergroße Fehlstelleninseln wachsen. An diesen Stellen ist die Hybridisierung mit dem Au(111) Substrat aufgehoben. In Kombination mit Elektrolumineszenzmessungen beobachten wir dort ein Verschwinden jeglicher Zustandsdichte in der elektronischen Bandlücke von MoS_2.

Im zweiten Teil werden 2,5-bis(3-dodecylthiophen-2-yl)thieno[3,2-b]-thiophene (BTTT) Moleküle auf der MoS_2/Au(111) Probe aufgebracht und mit RTS Messungen untersucht. Wir beobachten dabei herrausragende Entkopplungseigenschaften von MoS_2, die eine Energieauflösung von unter 6 meV erlauben. Dadurch ist es uns möglich eine Vielzahl an vibronischen Zuständen der positiven Ionenresonanz (PIR) von BTTT aufzulösen. Dieser vibronische Fingerabdruck erlaubt es uns zwischen verschiedenen Rotameren von BTTT zu unterscheiden, wobei sich diese nur durch Rotation einer Thienothiophengruppe unterscheiden. Rechnungen mit Dichtefunktionaltheorie (DFT) von BTTT in Gasphase können die beobachteten vibronischen Spektren vollständig und in Übereinstimmung mit dem Franck-Condon-Prinzip reproduzieren. Im letzten Abschnitt benutzen wir die neu gewonnene hohe Energieauflösung, um das Störpotential von verschiedenen RTM Spitzen zu untersuchen, welches auf die elektronischen Zustände der BTTT Moleküle einwirkt. Der Effekt der inhomogenen Potentialverteilung im Tunnelkontakt kann qualitativ mit Hilfe eines einfachen elektrostatischen Models der Doppelbarriere reproduziert werden. Durch den Vergleich der Energieverschiebungen des elastischen und eines inelastischen Peaks können wir zwischen den Störpotentialen unterscheiden, die durch eine dipolare Spitze oder die an der Probe angelegte Spannung entstehen.

Contents

— Chapter 1 —

Introduction

In the year 1965 Gordon Moore wrote an article and formulated the observation that the number of transistors on an integrated circuit board doubled about every two years. He also predicted this growth rate to continue for the next decade. This formulation became known as "Moore's law" and proved to be correct for the next 50 years. In the last years, however, the sizes of transistors have been reaching a scale of a few nanometers, where quantum mechanical limits are reached, *e.g.* current leakage by tunneling.

On the other hand, the need for smaller and more energy conserving transistors is everlasting in the rapidly growing digitalization of the world, so new solutions have to be found. A possible new way is to utilize molecular nanotechnology as functional molecules can be used as building blocks of an electronic circuit. Even though such functional molecules were subject of many studies [1–3], molecular electronics is still far from industrial scale. One hurdle to take is the fact, that the molecule has to be placed on some sort of substrate to be contacted. The interaction with the surface, however, leads to changes of structure or electronic properties of the molecule. Hence, some candidates, that were promising for molecular electronics in gas or liquid phase, turned out to be challenging upon adsorption on a substrate.

In order to reduce the interaction between molecules and substrates the need for decoupling layers arose. In 2004 X. H. Qiu *et al.* created an ultrathin Al_2O_3 layer by oxidizing the surface of the NiAl(110) surface. It enhanced the energy resolution of tunneling spectroscopy measurements sufficiently that vibronic states of copper phthalocyanine molecules could be observed [4]. A year later J. Repp *et al.* demonstrated for pentacene molecules on a NaCl layer, that one can image the molecular orbitals with scanning tunneling microscopy [5]. NaCl was also used as a decoupling layer when L. Gross *et al.* resolved the chemical structure of a molecule with atomic force microscopy [6]. Over the time many other decoupling layers have been introduced, such as MgO [7, 8], graphene [9–11], or hexagonal boron nitride [12–15], each with some benefits and downsides.

In this work we present MoS_2 as a valuable addition to the field of decoupling layers. In Chapter 2 the physics of molecular adsorbates are discussed and from that the requirements for a good decoupling layer are derived. Furthermore, the material MoS_2 is introduced, as well

as the benefits of using a single-layer MoS_2 as a decoupling layer. Then Chapter 3 and 4 give a brief introduction to the experimental and theoretical techniques used in this work and also to the experimental setup.

The results of the investigations were published in four articles, which are presented and discussed in Chapter 5. This chapter is thematically divided into two parts, with two publications each. In the first part we investigate the structural and electronic properties of the MoS_2/Au(111) interface by means of scanning tunneling and atomic force microscopy. MoS_2 forms a moiré pattern on the Au(111) structure with different stacking sequences of the atomic layers at the interface. We assign the different sites of the moiré pattern to those stacking orders and find a certain orientation of the MoS_2 islands with respect to the underlying Au(111) surface. The electronic properties are probed by scanning tunneling spectroscopy. We investigate the influence of the Au(111) layer to the MoS_2 and find a strong hybridization and an unoccupied state that most likely occurs due to the MoS_2/Au(111) interface. These results are then compared to the electronic properties of quasi-freestanding MoS_2.

In the second part of Chapter 5 we use MoS_2 as a decoupling layer for oligothiophene-based molecules. We achieve an energy resolution of a few millielectronvolts for the molecule's electronic states. Enhancing the sensitivity or resolution of an experimental technique often reveals formerly hidden features and is, therefore, a major driving force to a new or better understanding of the underlying physical principles. In scanning tunneling microscopy the spatial resolution is already exceptionally high, which we will then combine with the newly gained energy resolution. We perform vibrational analysis of two rotamers of the 2,5-bis(3-dodecylthiophen-2-yl)thieno[3,2-b]-thiophene (BTTT) molecule, that differ only by the rotation of the thienothiophene group in the center. Using DFT calculations we compare these results to the vibronic fingerprint of BTTT in gas phase and fully reproduce the measured spectra. In the last section we investigate the perturbation potential of the tip. The potential distribution in a tunneling junction is generally inhomogeneous in a plane parallel to the surface, due to the curvature of the tip apex. Using the high energy resolution, we probe this inhomogeneity acting as a perturbation potential on the delocalized electronic states of the BTTT molecule. With a simple electrostatic model we reproduce our observation qualitatively and distinguish between the perturbation potential caused by the applied bias voltage and the bias-independent perturbation potential of a dipolar tip.

— Chapter 2 —

Theoretical Background

The motivation to use molybdenum disulfide (MoS_2) as a decoupling layer, originates from the interactions between a molecular adsorbate and the underlying substrate. In this chapter we will discuss these interactions and then introduce MoS_2 as a potential candidate for a decoupling layer.

2.1. Molecular Adsorbates

The investigation of molecules with a scanning tunneling microscope (STM) requires the molecules to be adsorbed on a substrate, which has to be made of a conducting material. In most cases metal samples are used, which have the disadvantage, that they modify the electronic properties of the molecular adsorbate, due to various interactions like screening or hybridization, leading to energy level broadening and possibly partial charge transfer . The strength of these interactions depends on the nature of the adsorption: in case of the weak physisorption the molecule is only bound by van der Waals forces, barely perturbing the electronic structure. In contrast to that does the stronger chemisorption involve a chemical bond formation between adsorbate and surface. The transition between these adsorption types is gradual, as hybridization does already occur with physisorption but much weaker.

The screening effect, on the other hand, is not as dependent on the adsorption strength. To understand its origin, we have to consider the functional principle of STM. In tunneling microscopy or tunneling spectroscopy we usually assume a low tunneling current, *i.e.* single-electron tunneling. Depending on the sign of the applied bias voltage, a single electron tunnels from the tip to the molecular adsorbate or vice versa. In both cases, the probed molecule is left for a short time in a different charge state, before it relaxes to its (neutral) ground state. This usually occurs by charge transfer with the underlying surface . At typical parameters, the tunneling rate between molecule and surface is much higher than the rate between tip and molecules, ensuring that the molecule is most of the time in its ground state. Without a conducting surface, the charge would be stabilized in the molecule and no further tunneling would occur due to Coloumb blockade [16, 17].

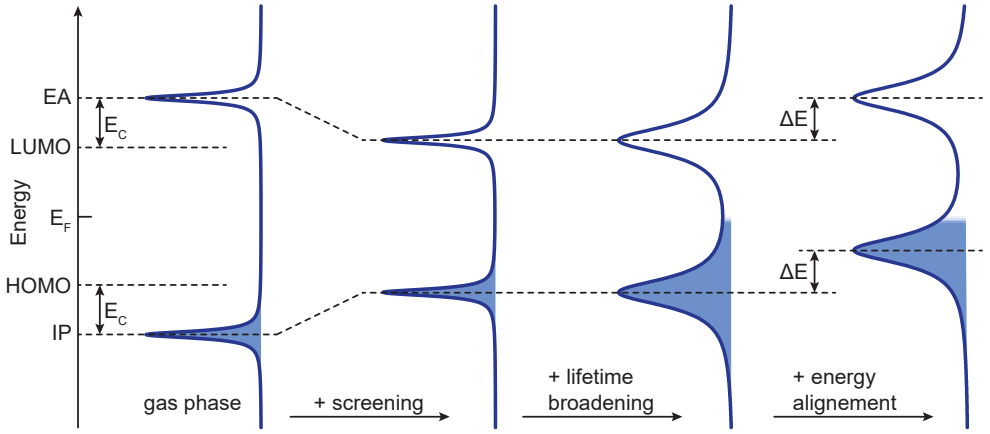

Figure 2.1.: Change of the electronic states of a molecule upon adsorption on a metal surface. In the gas phase (left) the energy difference between the electron affinity (EA) and ionization potential (IP) is larger than the HOMO-LUMO gap due to the Coloumb repulsion E_C. Screening effects of the metal substrate reduce E_C and thus shift the charge states towards the Fermi energy E_F. The shorter lifetime of the electronic states leads to a broadening and possible energy alignment might cause a rigid shift of the states with respect to E_F

When the electronic state of an adsorbate is investigated by tunneling spectroscopy, the frontier orbitals of molecules are usually of interest, often referred to as highest occupied molecular orbital (HOMO) and lowest unoccupied molecular orbital (LUMO). During the tunneling process, the adsorbate becomes charged and the observed states are not of the neutral molecule, but are the cationic and anionic states. They are observed at higher absolute bias voltages, shifted by the Coulomb repulsion energy E_C which is required to charge the molecule, as shown in Figure 2.1. These states correspond to the electron-affinity level (EA) and ionization potential (IP), and are also referred to as negative ion resonance (NIR) or positive ion resonance (PIR) in tunneling spectroscopy.

In the case of a molecule adsorbed on a metal surface, the Coulomb repulsion is counteracted by the sea of electrons in the sample. The electric field of the charged molecule is screened by image charges in the substrate and E_C is strongly reduced. Hence, the observed ionic resonances in a tunneling spectrum are shifted towards the Fermi energy E_F as depicted in Figure 2.1. This screening can also be enhanced by neighboring molecules, reducing the Coulomb repulsion even further [18].

Another effect of a metal substrate is the energy broadening of the electronic states. As described above, the temporarily charged state usually relaxes by charge transfer between adsorbate and substrate. Due to the high tunneling rate between adsorbate and substrate, the lifetime of the charged state is very small, which determines the width of a lorentzian energy broadening, in accordance to the time-energy uncertainty relation. Especially on metal substrates can the electronic states of the molecule hybridize strongly with the energy bands

of the metal, reducing the lifetime down to a few femtoseconds and causing a broadening of tens or even hundreds of millielectronvolts [19].

The hybridization can also lead to an energy level alignment, shifting the molecular electronic states with respect to the Fermi level of the substrate. Such a shift is usually also accompanied by a partial charge transfer between adsorbate and substrate.

2.1.1. Vibronic States

The investigation of a molecule's electronic states often implies the excitation of its vibrational modes, sometimes causing a complex arrangement of resonances in a spectrum. The combined excitations of electronic and vibrational states are referred to as vibronic excitations and are described by the Franck-Condon principle [20, 21]: Starting with Fermi's golden rule, the transition rate between a ground state Ψ and the excited state Ψ' is:

$$\Gamma = \frac{2\pi}{\hbar} \left|\langle \Psi' | H' | \Psi \rangle\right|^2 \delta\left(E' - E\right), \tag{2.1}$$

with E and E' being the energies of the ground and excited states and H' the perturbing hamiltonian, depending on the kind of electronic excitation. In accordance with the Born-Oppenheimer approximation we can separate the total wave functions into electron wave function Ψ_e and vibrational wave function Ψ_ν, which depends on the position of the nuclei:

$$\Gamma = \frac{2\pi}{\hbar} \left|\langle \Psi'_e \Psi'_\nu | H' | \Psi_\nu \Psi_e \rangle\right|^2 \delta\left(E' - E\right). \tag{2.2}$$

Please note, that we are not considering the spin of the particles. In the following we assume, that our perturbing hamiltonian can also be split into a part H'_e acting on the electron wave function and a part H'_N acting on the nuclei wave function. This holds true for dipole transition via photon absorption, as well as for electron tunneling (where $H'_N = 0$). Equation 2.2 can then be approximated by:

$$\Gamma = \frac{2\pi}{\hbar} \left|\langle \Psi'_e | H'_e | \Psi_e \rangle \langle \Psi'_\nu | \Psi_\nu \rangle + \langle \Psi'_e | \Psi_e \rangle \langle \Psi'_\nu | H'_N | \Psi_\nu \rangle\right|^2 \delta\left(E' - E\right). \tag{2.3}$$

As the electronic wave functions are orthogonal, *i.e.* $\langle \Psi'_e | \Psi_e \rangle = 0$, the equation simplifies to:

$$\Gamma = \frac{2\pi}{\hbar} \left|\langle \Psi'_e | H'_e | \Psi_e \rangle\right|^2 \left|\langle \Psi'_\nu | \Psi_\nu \rangle\right|^2 \delta\left(E' - E\right). \tag{2.4}$$

The first integral gives the probability to excite the molecule electronically and corresponds for tunneling spectroscopy to the tunneling matrix element described in Section 3.1.2. The second integral $\langle \Psi'_\nu | \Psi_\nu \rangle$ is the overlap integral of the vibrational wave functions and is often referred to as Franck-Condon factor.

In the following we describe the vibrational wave functions in vibrational normal coordinates, giving $\Psi_{k,n}$ for the nth excitation of the vibrational normal mode k and Ψ_g for the initial

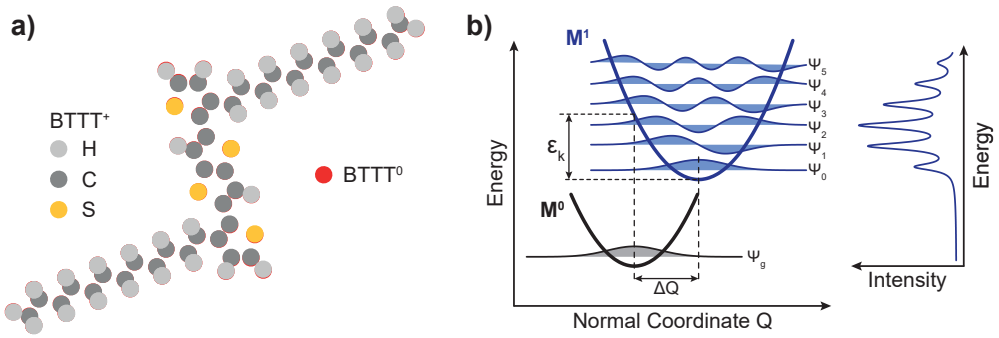

Figure 2.2.: a) Comparison of the structure between the uncharged $BTTT^0$ (red) and positively charged $BTTT^+$ (color) molecule. **b)** Model of the Franck-Condon principle: After electronic excitation, the molecule has a new relaxed structure that leads to a shift ΔQ of the equilibrium position in normal vibrational coordinates. The relative intensity of a vibronic peak in a spectrum is determined by the overlap between the vibratonal wave functions of the initial state (gray) and the final state (blue).

ground state. Assuming the positions of the nuclei do not change upon electronic excitation, the overlap integral would be

$$\langle \Psi_{n,k} | \Psi_g \rangle = \begin{cases} 1 & \text{for} \quad n = 0 \\ 0 & \text{for} \quad n > 0 \end{cases} \tag{2.5}$$

and no vibrational modes would be excited.

However, molecules usually deform upon electronic excitation (*i.e.* charging) as depicted for a BTTT molecule in Figure 2.2a. In vibrational normal coordinates, this deformation expresses itself as a shift of the equilibrium position. Thus the overlap of the ground state with the vibrational states is no longer zero and excitation of vibronic states becomes possible, as shown in Figure 2.2b. The relative intensity between the vibronic states can be described (for harmonic oscillators) by the Poisson distribution [22]:

$$\left| \langle \Psi_{k,n} | \Psi_g \rangle \right|^2 = e^{-S_k} \frac{S_k^n}{n!}, \tag{2.6}$$

with S_k being the so called Huang-Rhys factor of the vibrational mode k. It is determined by its energy $\hbar\omega_k$ and relaxation energy ε_k (see Figure 2.2b):

$$S_k = \frac{\varepsilon_k}{\hbar\omega_k} \tag{2.7}$$

The total relaxation energy ε_{rel} of the molecule is then given by:

$$\varepsilon_{\text{rel}} = \sum_k \varepsilon_k = \sum_k S_k \cdot \hbar\omega_k. \tag{2.8}$$

The Franck-Condon principle allows to calculate the intensity and energy of the vibronic resonances in a $\mathrm{d}I/\mathrm{d}V$ spectrum. For this the relaxed structure of a molecule in its charged

and neutral state, as well as its vibrational normal modes, have to be known, *e.g.* by DFT calculations, as shown in *ACS Nano* ***12*** *(2018) 11698*. However, in STM such vibronic states are no visible most of the time, due to the broadening of the energy levels.

2.1.2. Energy Broadening and Decoupling Layers

The resonances of a molecule's electronic states are not only subject to lifetime broadening, but to many different broadening mechanisms. They can be due to external sources of noise – both electrical and mechanical – as well as experimental conditions, *e.g.* broadening due to finite temperatures. Most often a lock-in amplifier is used in order to improve the signal-to-noise ratio in tunneling spectroscopy measurements, which itself also broadens the $\mathrm{d}I/\mathrm{d}V$ signal with its modulation voltage. However, all these origins can be reduced to a certain extent by optimizing the setup, using smaller modulation amplitudes of the lock-in amplifier or reducing the temperature. In some cases the origins can even be avoided, *e.g.* by using a superconducting tip to reduce the effect of the temperature broadening [23].

The lifetime broadening, on the other hand, is an intrinsic broadening of the investigated system, that can only be reduced by modifying that system. A popular approach is to introduce a second tunneling barrier between adsorbate and substrate in the form of a decoupling layer. It should reduce the interaction between the molecule and the substrate, while also having a minimal interaction with the molecule itself. This implies, that the decoupling layer should be chemically inert, so the molecules do not hybridize with the states of the decoupling layer.

There are different mechanisms for an excited state to relax after the tunneling event, so there are also several properties that determine the decoupling quality of a material. The most prominent way of relaxation is, as described above, the discharging of the molecule back to its neutral state (assuming this is the ground state). Hence, a decoupling layer is required to have a band gap around the $\bar{\Gamma}$ point at the energy of the excited state. This prohibits a discharging into the decoupling layer. Additionally it should have a certain thickness, in order to reduce the tunneling rate between molecule and substrate by a larger vertical distance between them.

Another important point to consider is the possibility of the molecule not only being charged by the tunneling event, but also becoming vibrationally excited. These vibronic states have been observed for many molecules on different decoupling layers [4, 5, 10, 11, 14, 24–26], thus they are not negligible in our consideration of the lifetime. The relaxation of such vibronic states occurs either by discharging (as described above) or by relaxation of the excited vibrational mode. The latter can happen by the formation of electron-hole pairs in the substrate at the Fermi energy to drain the vibrational energy of the molecule. Accordingly, a decoupling layer with a real band gap (not only at $\bar{\Gamma}$) would suppress this relaxation path of the vibronic state. This real band gap does not need to be large enough to include the electronic state as required for the quasi band gap around $\bar{\Gamma}$, its size only needs to be larger than the energy of the vibrational modes, in order to prevent the formation of electron-hole pairs.

The excitation of vibrations brings an additional aspect to the broadening of electronic resonances. A decoupling layer with a high electron-phonon coupling might get vibrationally excited itself, possibly causing additional features or a gaussian broadening of the peaks in the tunneling spectrum [27]. This is an important factor for ionic materials like NaCl or Al_2O_3. Fatayer *et al.* showed that charging a naphthalocyanine (NPc) molecule on a NaCl layer causes a deformation of the NaCl lattice that is responsible for 97 % of the total relaxation energy of the system [17]. In order to minimize this effect, a non-ionic decoupling layer with a low electron-phonon coupling is preferred.

A promising material that meets all these requirement, as we will show in this work, is molybdenum disulfide. It is a naturally occurring material, that gained much attention recently and is now subject of many studies, in particular its monolayer.

2.2. Molybdenum Disulfide

Molybdenum disulfide (MoS_2) is a transition metal dichalcogenide (TMD) with a layered structure, similar to that of graphite. The single layers consist of Mo atoms, sandwiched between two layers of S atoms, forming a two dimensional structure. In bulk these layers are only held together by weak van der Waals forces and, just like graphite, these weakly bound layers cause a low friction coefficient. This makes MoS_2 a good dry lubricant, as which it has been used for a long time already. Furthermore, it also found use in petrochemistry and organic synthesis as a (co-)catalyst. Whereas the surface of MoS_2 is rather inert, the edges of the layers (and possible defects) can serve as active sites, *e.g.* for hydrodesulfurization of hydrocarbons [28, 29].

The unit cell of MoS_2 is typically trigonal prismatic (see Figure 2.3a), where the sulfur atoms of the upper and lower layer are on top of each other. Under certain conditions, *e.g.* intercalation of alkali metals, the meta stable octahedral unit cell has also been observed, where one sulfur layer is rotated by 180° [30]. MoS_2 with an octahedral unit cell is metallic and in bulk its layers stack in the 1T phase, as depicted in Figure 2.3b. The trigonal prismatic unit cell, on the other hand, is semiconducting and has two phases. In the more common 2H phase every second layer is rotated by 180° and the molybdenum site is positioned above the sulfur site of the next layer (see Figure 2.3c). The less common 3R phase can also been found in nature and consists of MoS_2 layers that are not rotated with respect to each other, but laterally shifted as shown in Figure 2.3d.

The electronic structure of bulk 2H-MoS_2 shows an indirect band gap of 1.23 eV(see Figure 2.4a) [31]. The maximum of the valence band is located at the $\bar{\Gamma}$ point and with an additional local valence band maximum at the $\bar{K}$ point. The minimum of the conduction band on the other hand is located between the $\bar{\Gamma}$ and the $\bar{K}$ point [32, 33]. However, for freestanding single-layer MoS_2 the band structure is different.

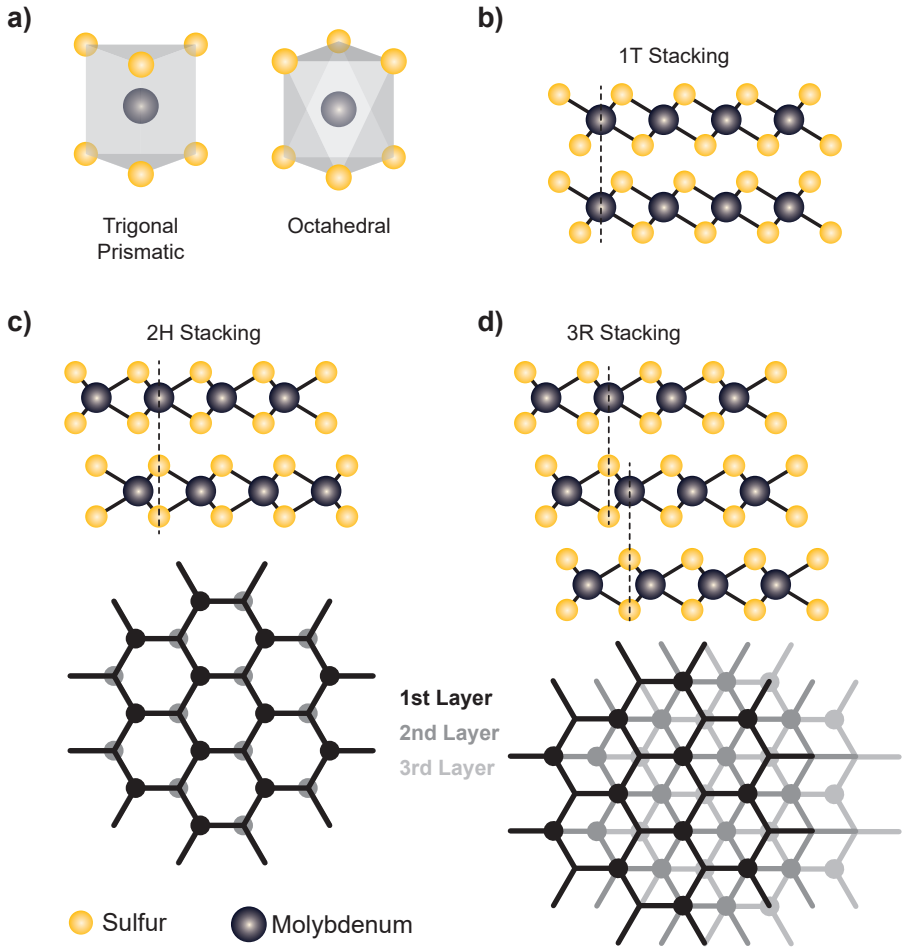

Figure 2.3.: a) Two possible unit cells of MoS_2. **b)** 1T phase of octahedral MoS_2 in side view. **c,d)** Stacking phases of trigonal prismatic MoS_2 in side view (top) and top view (bottom). The layers in the 2H phase are rotated with respect to each other, whereas they are only shifted in the 3R phase. In the top view, only the Mo atoms are depicted as circles and the bonds with the S atoms as lines.

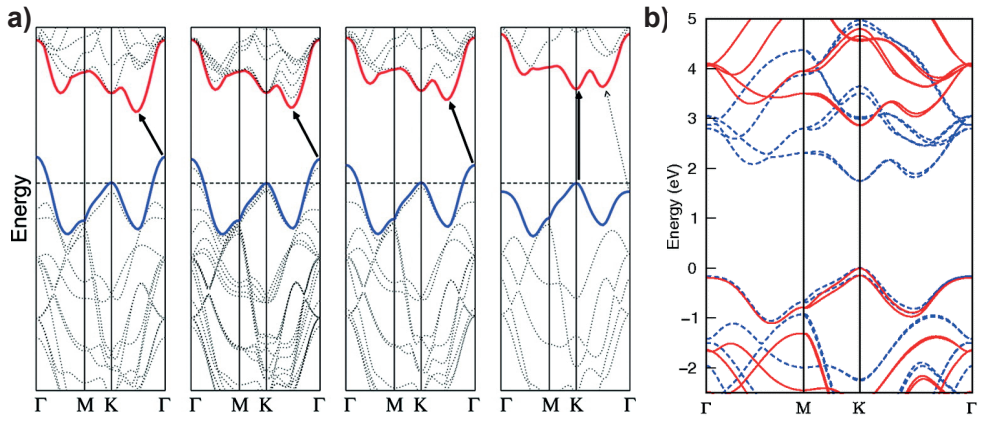

Figure 2.4.: a) Evolution of the band structure of 2H-MoS_2 when thinned down to a monolayer (from [35]). From left to right: bulk, quadrilayer, bilayer and single-layer MoS_2. **b** LDA (blue dotted) and GW (solid red) band structure of single-layer $MoS_2$with spin-orbit coupling (from [39]). Due to the strong spin-orbit coupling, MoS_2 features a strong spin-split at the VBM and the conduction band.

2.2.1. Single-Layer MoS_2

The indirect band gap of MoS_2 is strongly dependent on the number of layers or their relative distance to each other [34]. With decreasing layer number the indirect band gap of MoS_2 increases, due to the higher quantum confinement, up to the point that single-layer MoS_2 becomes a direct-gap semiconductor (see Figure 2.4a) [35, 36].

The new direct band gap at the $\bar{K}$ point exhibits a very high exciton binding energy of ≈1 eV [37–39]. This allows for a long exciton lifetime even at high temperatures and increases the luminescence quantum efficiency by a factor of more than 10^4 compared to bulk MoS_2 [36]. The long exciton lifetime and high quantum efficiency makes single-layer MoS_2 an interesting material for photonic devices.

Furthermore, a strong spin-orbit coupling leads to a large spin-splitting of the valence and the conduction band (see Figure 2.4b). At the valence band maximum around the $\bar{K}$ valleys, a spin-splitting of nearly 150 meV has been predicted [39, 40], with a spin reversal between the $\bar{K}$ and -$\bar{K}$ point, due to the broken inversion symmetry of MoS_2. A recent study was able to confirm these predictions experimentally for single-layer MoS_2 on a Au(111) surface [41], opening up MoS_2 as a promising material for spin- and valleytronics and other spin-devices.

Another – at first sight rather mundane – field of application for such 2D materials is the role as decoupling layer. For STM studies a broad range of decoupling layers have already been investigated and are in use, such as Graphene [9–11], hexagonal boron nitride (h-BN) [12–15], Xe [26], RbI [26], NaCl [5, 42–44] or Al_2O_3 [4, 24, 45–48], each with its own advantages and disadvantages. MoS_2 can be a valuable addition to this field, as it combines a certain set of features that constitute a good decoupling layer, as described above in Section 2.1.2. It

is thicker than graphene or h-BN and thus decouples the adsorbate better from the metal substrate. It also has a band gap, which prohibits a fast relaxation of the excited adsorbate state via the decoupling layer itself. These requirements are also met by NaCl or Al_2O_3, but MoS_2 combines them with a covalently bound structure. Its non-ionic nature reduces the electron-phonon coupling and inhibits the possible broadening due to phonon excitations in the decoupling layer.

This combination of decoupling properties distinguishes MoS_2 from the other materials and allows for new kinds of STM investigations with unprecedented energy resolution, as we will show in this work.

— Chapter 3 —

Methods

The experimental methods used for this work were a combination of scanning tunneling microscopy (STM), scanning tunneling spectroscopy (STS), and atomic force microscopy (AFM). They are often summarized as scanning probe microscopy (SPM) and allow for the investigation of surfaces in real space on an atomic scale. The STM is sensitive to electronic states of a conducting surface and in combination with STS a powerful tool to probe the electronic properties of the sample around the Fermi energy with high spatial resolution. An AFM on the other hand is not restricted to conducting surfaces as it relies on forces in the SPM junction. Thus it provides more reliable information about the topography of the sample and is capable of resolving the atomic structure of a single molecule [6, 49].

To complement the experimental results, density functional theory (DFT) calculations have been performed. It is a useful method to calculate *ab intio* the electronic structure of many-body systems, such as molecules.

In the following chapter the methods, which are used in this work, are introduced and their underlying theory discussed.

3.1. Scanning Tunneling Microscopy

When Binnig and Rohrer introduced the first scanning tunneling microscope (STM) with atomic resolution in 1982 [50], they opened the doors for a variety of new surface science techniques. The STM allows the investigation of single structures, without relying on periodic ordering or having to average over a large area. It is based on the quantum mechanical tunneling effect, in which a quantum particle crosses a potential barrier of higher energy. As the tunneling probability between two electrodes is strongly distance dependent, it can be used to measure the electronic topography of a sample with a nanoscopic probe. Today, STM has become a versatile tool to investigate many phenomena beyond structure, such as molecular vibrations [4, 24, 51–53], electroluminiscence [54–60], and spin states [45, 61, 62].

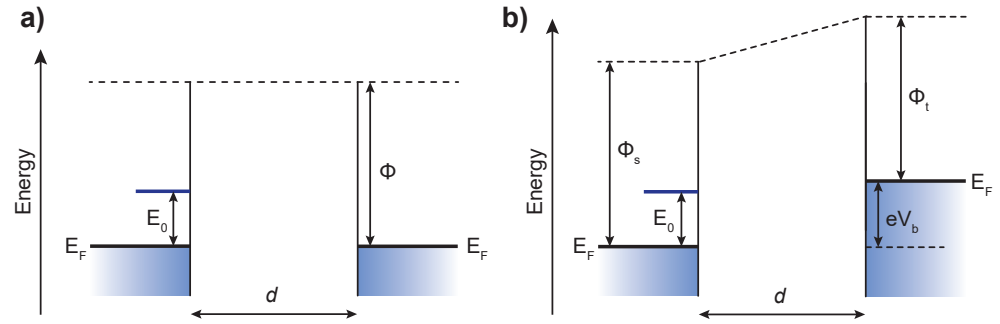

Figure 3.1.: a) Simple rectangular potential barrier, with an electronic state of energy E_0 (blue). **b)** Barrier between sample and tip with different work functions and applied bias voltage.

3.1.1. Simple Tunneling Theory

The simplest way to describe the tunneling process is by using the textbook case of a rectangular potential barrier with height ϕ and thickness d, as depicted in Figure 3.1. This problem can be solved analytically with the one-dimensional stationary Schrödinger equation resulting in a tunneling probability for a particle with energy $E < \phi$ and mass m:

$$T(E,z) \propto \exp\left[-2d\sqrt{\frac{2m}{\hbar^2}(\phi - E)}\right]. \tag{3.1}$$

Even though this is only a very simple picture, it already shows an important characteristic of the tunneling effect: For typical values of ϕ around 5 eV the tunneling probability – and therefore the tunneling current – are reduced by one order of magnitude when the width of the barrier is increased by 1 Å. Assuming different work functions between tip and sample, and an applied bias voltage V_b to the sample, the tunneling probability becomes in first approximation:

$$T(E,V_\mathrm{b},z) \propto \exp\left[-2d\sqrt{\frac{2m}{\hbar^2}\left(\frac{\phi_t + \phi_s + eV_\mathrm{b}}{2} - E\right)}\right]. \tag{3.2}$$

This simple picture does not consider the electronic structures of the two leads. To include those, a many-particle point of view is required.

3.1.2. The Tersoff and Hamann Approach

A complex but more accurate model of the tunneling current has been introduced by Tersoff and Hamann in 1983 [63]. In their work they used Bardeen's approach, in which he assumed a potential barrier between z_a and z_b with two metals a and b at the sides [64]. He considered two many-particle states of the entire system, Ψ_0 and $\Psi_{\mu\nu}$, where $\Psi_{\mu\nu}$ differs from Ψ_0 by the transfer of one electron from state μ in metal a to state ν in metal b. For an elastic tunneling

process without energy loss this gives for the tunneling matrix element:

$$M_{\mu\nu} = \frac{\hbar^2}{2m} \int \mathrm{d}\mathbf{S} \left[\Psi_0^* \nabla \Psi_{\mu\nu} - \Psi_{\mu\nu} \nabla \Psi_0^* \right], \tag{3.3}$$

with m being the electron mass and $\mathbf{S}$ an arbitrary surface within the tunneling junction.

Tersoff and Hamann used this matrix element to calculate the tunneling current in first order perturbation theory:

$$I = \frac{2\pi e}{\hbar} \sum_{\mu\nu} f\left(E_\mu\right) \left[1 - f\left(E_\nu\right)\right] |M_{\mu\nu}|^2 \delta\left(E_\nu - eV_\mathrm{b} - E_\mu\right), \tag{3.4}$$

where $f(E)$ is the Fermi-Dirac distribution, V_b the applied bias voltage and E_μ and E_ν are the energies of states the Ψ_μ and Ψ_ν.

In case of an STM junction, these wave functions correspond to the sample and the tip. For the latter, Tersoff and Hamann assumed an s-wave tip with a local spherical wave function at $\mathbf{r}_0$:

$$\Psi_\mu = \frac{C_\mu}{\sqrt{\Omega_t}} \frac{e^{-\kappa|\mathbf{r}-\mathbf{r}_0|}}{\kappa|\mathbf{r}-\mathbf{r}_0|}. \tag{3.5}$$

C_μ is a normalization factor, Ω_t the volume of the probing tip, $\kappa = \sqrt{2m\phi/\hbar^2}$ the inverse decay length and ϕ the work function of the tip. For the surface wave function they assumed a Bloch wave that decays exponentially in the vacuum in normal direction z:

$$\Psi_\nu = \sum_{\mathbf{G}} a_\mathbf{G} \, \exp\left[-\sqrt{\kappa^2 + |\mathbf{k}_\parallel + \mathbf{G}|^2} \cdot z \right] \cdot \exp\left[i \left(\mathbf{k}_\parallel + \mathbf{G}\right) \cdot \mathbf{r}_\parallel \right], \tag{3.6}$$

where $\mathbf{k}_\parallel$ is the surface Bloch wave vector of the state, $\mathbf{G}$ the surface reciprocal-lattice vector, $a_\mathbf{G}$ a normalization factor, and κ the inverse decay length as described above. For simplicity, the work functions for tip and sample are assumed to be equal.

Tersoff and Hamann showed, that inserting these wave functions in equation 3.3 yields:

$$M_{\mu\nu}(\mathbf{r}_0) \propto \frac{1}{\sqrt{\Omega_t}} \cdot \Psi_\nu(\mathbf{r}_0). \tag{3.7}$$

In the following we consider possible tunneling in both directions, depending on the applied bias voltage. Thus, the factor with the Fermi-Dirac distributions simplifies to $f\left(E_\mu\right) - f\left(E_\nu\right)$. Including equation 3.7 in 3.4 results in:

$$I(V, \mathbf{r}_0) \propto \sum_{\mu\nu} \left[f\left(E_\mu\right) - f\left(E_\nu\right) \right] \frac{1}{\Omega_t} \cdot |\Psi_\nu(\mathbf{r}_0)|^2 \cdot \delta\left(E_\nu - eV_\mathrm{b} - E_\mu\right) \tag{3.8}$$

In oder to express the tunneling current as an integral we define $\rho_t(E)$ as the density of states (DoS) of the tip and $\rho_s(E, \mathbf{r}_0)$ as the local density of states (LDoS) of the sample at position $\mathbf{r}$,

with

$$\rho_t(E) \equiv \sum_{\mu} \Omega_t^{-1} \delta(E - E_\mu) \tag{3.9}$$

$$\rho_s(E, \mathbf{r}) \equiv \sum_{\nu} |\Psi_\nu(\mathbf{r})|^2 \, \delta(E - E_\nu) \tag{3.10}$$

For low temperatures we can further assume the Fermi-Dirac distribution to be a step function and obtain for the tunneling current:

$$I(V, \mathbf{r}_0) \propto \int_{-\infty}^{+\infty} \mathrm{d}\epsilon \;\; \left[f(E_F) - f(E_F + eV_\mathrm{b}) \right] \rho_t(\epsilon - eV_\mathrm{b}) \cdot \rho_s(\epsilon, \mathbf{r}_0) \tag{3.11}$$

$$\propto \int_{0}^{eV_\mathrm{b}} \mathrm{d}\epsilon \;\; \rho_t(E_F + \epsilon - eV_\mathrm{b}) \cdot \rho_s(E_F + \epsilon, \mathbf{r}_0) \,. \tag{3.12}$$

Thus, the tunneling current is directly dependent on the DoS $\rho_t(E)$ of the tip and the LDoS $\rho_s(E, \mathbf{r}_0)$ of the sample at position $\mathbf{r}_0$ of the tip. The exponential decay of the tunneling current is included in the spatial dependence of ρ_s, as defined in equation 3.6. Considering different work functions and the applied bias voltage, the decay rate can be described equivalent to equation 3.2. By controlled tip forming (see Section 4.1.1), the tip's DoS can be optimized to be constant for small bias voltages. This leaves only the sample DoS and the applied bias as variable parameter.

Please note, that the assumption of an s-wave tip is chosen as a good approximation for most metal tips but not for all tips. For some metals, e.g. tungsten, the d-orbitals contribute major portions to the tunneling current [65]. Furthermore, studies with CO functionalized tips have shown, that the p-wave orbital of the CO molecule allows to investigate the divergence of the sample wave function [44].

3.1.3. Scanning Images

The great strength of an STM is its feature to scan small areas in real space and resolve single structures of atomic size. To perform this, the probing tip is usually mounted to one or more piezo elements, which allows its movement in all directions with picometer precision. Thus an image of the surface can be recorded by scanning the area line by line and measuring the tunneling current.

There are two basic modes of STM, the constant-height and the constant-current mode. In the constant-height mode the tip scans the surface at a fixed height and the tunneling current is recorded. The constant-current mode on the other hand uses a feedback loop to adjust the tip height during the scan and keeps the tunneling current constant. It is slightly slower than the constant-height mode, but less prone to tip crashes, as the surface most often is not perfectly flat. Hence, the constant-current mode is the default mode in STM nowadays.

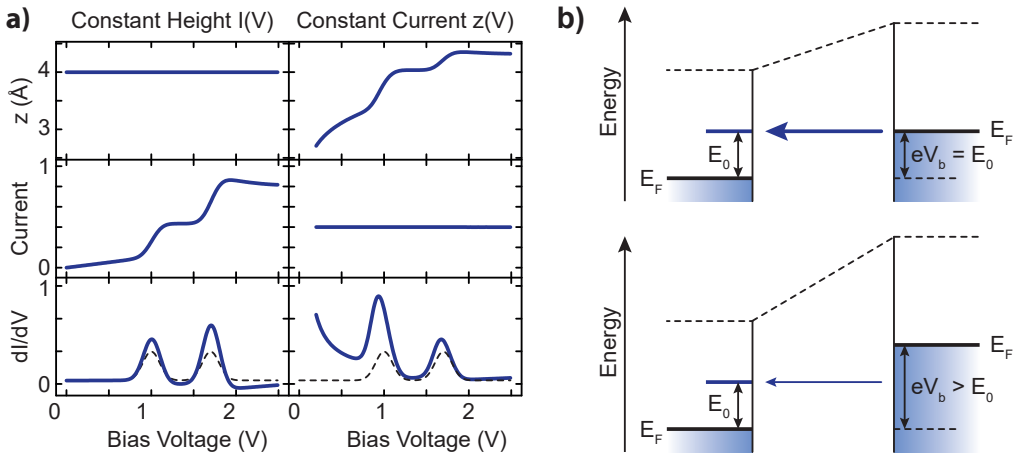

Figure 3.2.: a) Sketch of tip-sample distance z, tunneling current and its derivative for constant-height (left column) and constant-current mode (right column). The actual density of states (DoS) is added as dotted black line in the bottom panels. Due to applied bias voltage and a varying z, the $\mathrm{d}I/\mathrm{d}V$ signal is not fully proportional to the DoS. **b)** For an electron tunneling into a state with energy E_0, the tunneling barrier increases with the applied bias voltage. Thus the tunneling current into that state decreases with higher bias voltage, potentially giving rise to a negative differential conductance at energies just above E_0, as can be seen in a).

However, as described above, the tunneling current depends on both the topography and the DoS of the surface making it difficult to disentangle these two effects in the image (see Section 5.2). Therefore, the constant height mode is generally used for the mapping of the $\mathrm{d}I/\mathrm{d}V$ signal or Δf in AFM (see Section 3.3). These data are easier to analyze and to compare with calculations.

3.2. Scanning Tunneling Spectroscopy

Scanning tunneling spectroscopy (STS) is a powerful tool to investigate the electronic structure of surfaces or single adsorbates. Usually a lock-in amplifier is used to directly measure the derivative of the current with a high signal-to-noise ratio. As we assume the DoS of the tip to be constant for small voltages, equation 3.12 yields for the derivative:

$$\frac{\mathrm{d}\,I\,(V_\mathrm{b},\mathbf{r}_0)}{\mathrm{d}V} \propto \rho\,(E_F + eV_\mathrm{b},\mathbf{r}_0)\,. \tag{3.13}$$

This means the tunneling conductance is directly proportional to the DoS of the sample. By keeping the tip position $\mathbf{r}_0$ fixed and ramping the bias voltages, electronic states like molecular orbitals appear as resonant peaks in the $\mathrm{d}I/\mathrm{d}V$ spectrum. It is, however, an approximation for low temperatures and small bias voltages, as a large V_b distorts the vacuum barrier and changes the tunneling probability.

The position $\mathbf{r}_0$ of the tip in STS does not have to be fixed, though. Analogous to STM, the feedback loop for the tip height can be opened or closed while ramping the bias voltage. In the constant current $z(V_\mathrm{b})$ spectroscopy, the $(\partial I/\partial V)_I$ signal is recorded with closed feedback loop. It adjusts the tip height to keep the current at a predefined set point. This has the benefit of preventing damage in the junction due to high currents, but it requires a minimal bias voltage to maintain the set point current. The constant current also makes the renormalization easier for κ measurements (see Section 3.2.1).

On the other hand, the constant height $I(V_\mathrm{b})$ spectroscopy is taken with an opened feedback loop. The resulting $\mathrm{d}I/\mathrm{d}V$ signal is thus recorded with fixed $\mathbf{r}_0$ and not subject to a change of the vacuum barrier (for small bias voltages). Furthermore, it enables measurements around $V_\mathrm{b} = 0$ with bias voltages of a few mV or less, which is not possible with $z(V_\mathrm{b})$ spectroscopy.

In addition, the $\mathrm{d}I/\mathrm{d}V$ signal can be recorded at a fixed bias voltage in dependence of tip height ($I(z)$ spectroscopy) or by scanning the sample at fixed bias voltage and height ($\mathrm{d}I/\mathrm{d}V$ maps).

In systems with low background conductance, *e.g.* due to a decoupling layer, also a negative differential conductance (NDR) may occur, as can be seen around 2 V in the left column of Figure 3.2a. For an electron tunneling into a state with energy E, the tunneling barrier increases with the applied bias voltage. Thus the tunneling current into this state decreases at higher bias voltages. If there are no or only a few new states at higher energy to tunnel into (a low background DoS) the total tunneling current decreases, even though the bias voltage increases. Hence, the measured differential conductance $\mathrm{d}I/\mathrm{d}V$ becomes negative.

3.2.1. Probing the Bandstructure with STM

Even though STM has the benefit of a very high resolution in the real space, it is not simple to gain information with it about the reciprocal space. For a start, it is mostly sensitive to states at the $\bar{\Gamma}$ point in the Brillouin zone, which is due to the decay constant of the investigated states. In the simple picture of equation 3.2 the parallel momentum of states is most often omitted. For localized structures with only localized states (molecules or point defects) this picture is sufficient to describe the system. In the case of delocalized states, *e.g.* bulk or 2D materials with band structure, the parallel momentum $k_\parallel$ of a state with energy E needs to be taken into account for its decay constant:

$$\kappa = \sqrt{\frac{2m}{\hbar^2}\left(\phi + \frac{eV_\mathrm{b}}{2} - E\right) + k_\parallel^2}. \tag{3.14}$$

For simplicity we assume here the same work function for tip and sample. As can be seen, the higher the $k_\parallel$ of a state, the faster it decays into the vacuum. A state around E_F with $k_\parallel = 1\,\text{Å}^{-1}$ measured at a typical tip-sample distance of 5 Å would have about 40 times less intensity as an identical state with $k_\parallel = 0$ (see Figure 3.3a). Thus, the tunneling current is usually dominated by tunneling into states around the $\bar{\Gamma}$ point.

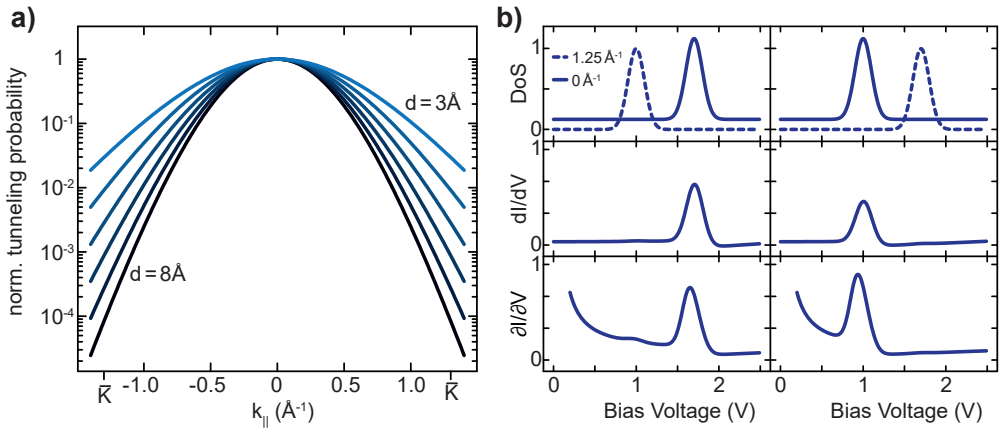

Figure 3.3.: a) Normalized tunneling probability in dependence of the $k_\parallel$ of the state and tip-sample distance d. For the height of the potential barrier $\phi = 5\,\mathrm{eV}$ are assumed. The ticks labeled $\bar{K}$ correspond to the $k_\parallel = 1.3\,\text{Å}^{-1}$ at the $\bar{K}$ point of MoS_2. **b)** $\mathrm{d}I/\mathrm{d}V$ and $(\partial I/\partial V)_I$ signal for two states with $k_\parallel = 0$ and $1.25\,\text{Å}^{-1}$ and a background DoS without $k_\parallel$. The state with non-vanishing $k_\parallel$ can only be reliably observed with $(\partial I/\partial V)_I$ spectroscopy and if it is lower in energy than the state without $k_\parallel$.

In order to detect a state with high $k_\parallel$, the tip has to be brought very close to the sample, posing the risk of damaging the junction, as a state of similar energy without any $k_\parallel$ would lead to a high tunneling current. To avoid this problem in constant height $\mathrm{d}I/\mathrm{d}V$ spectroscopy, a large tip sample distance would be required, which in turn means the state with high $k_\parallel$ is no longer detectable. In constant current $(\partial I/\partial V)_I$ spectroscopy, the variable tip sample distance allows the probing of the state as long as it is within the quasi-gap at $\bar{\Gamma}$. In case of a state without $k_\parallel$ at lower energies, the tip is already too far away from the sample to detect the high $k_\parallel$ state, as shown in Figure 3.3b.

In 2015 Zhang *et al.* introduced a method to measure the decay constant κ of the tunneling current and to detect states with high $k_\parallel$ [66]. Using a lock-in amplifier, the tip height was modulated to get the derivative of the tunneling current $\mathrm{d}I/\mathrm{d}z$. This is directly proportional to the decay constant:

$$\kappa(V_\mathrm{b}, k_\parallel) = -\frac{1}{2I_0} \cdot \frac{\mathrm{d}I(V_\mathrm{b})}{\mathrm{d}z}. \tag{3.15}$$

As they used this techniques with a closed feedback loop, I_0 represents the constant set point current. From the measured κ signal it is possible to deduce information about the $k_\parallel$ of a state according to equation 3.14 and, thus, to roughly localize it in the band structure.

3.2.2. Inelastic Tunneling

Up to this point only elastic tunneling has been considered where the initial and final state of the electron have the same energy. In inelastic tunneling the electron looses some or all of its energy in the junction by different mechanisms, enabling it to tunnel into a final

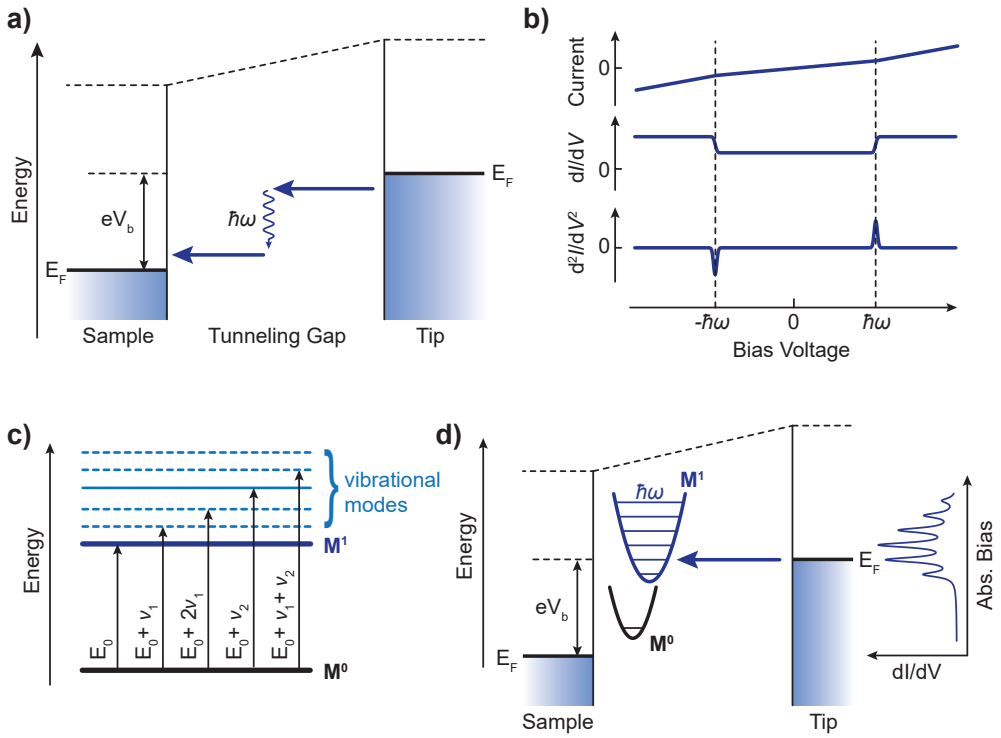

Figure 3.4.: a) Sketch of the tunneling junction for inelastic tunneling. Due to various mechanisms, the electron can loose energy in the junction and tunnel into a final state with less energy than the initial state. **b)** Off-resonant inelastic tunneling appears as steps in the differential conductance at a threshold energy (here: $\hbar\omega$) symmetrically around zero bias voltage. In the second derivative of the tunneling current, these steps appear as peaks and dips. **c)** In resonant inelastic tunneling, the molecule is excited vibrationally and electronically. The excitation of several vibrational modes is possible. **d)** The resonant tunneling into vibronic states leads to peaks in the conductance spectrum with constant energy spacing $\hbar\omega$ (assuming only one mode is excited). The relative intensity of the peaks is given by the Poisson distribution..

state with lower energy than the initial state. These mechanisms can be the excitation of vibrational modes in resonant [4, 24, 52] and off-resonant tunneling [51, 52, 67], by spin-excitations [45, 61, 62], or by emitting a photon [54–60].

In the following, the mechanisms for vibrational excitation of molecules as well as light emission from the tunneling junction will be discussed.

Vibronic States of Molecules

The term inelastic tunneling spectroscopy (IETS) usually refers to the off-resonant loss of a certain energy in the tunneling junction, as depicted in Figure 3.4a. This can be due to excitations of spin states or molecular vibrations with energy $\hbar\omega$. If the bias exceeds this

energy threshold an additional tunneling channel is opened that increases the conductance of the tunneling junction. In the $\mathrm{d}I/\mathrm{d}V$ spectrum such an excitation appears as two step functions symmetrically around zero bias at energies of $\pm\hbar\omega$. They are most of the time rather small compared to the elastic conductance background, making their detection challenging in the first derivative of the current. In the second derivative $\mathrm{d}^2I/\mathrm{d}V^2$ the inelastic features appear as clear peaks and dips at the corresponding energies, as shown in Figure 3.4b.

In IETS, the energy resolution of the conductance steps does not depend directly on the energy broadening of the molecule's electronic states, but on the broadening of the tip and substrate states. In a low-temperature STM ($T \approx 4.5\,\mathrm{K}$) this yields an energy resolution down to 1-2meV, enough to detect even small changes in the vibrational energy, *e.g.* due to different isotopes in the molecule [68] or external forces which can provide intramolecular resolution of other adsorbates [67].

Another mechanism is the excitation of molecular vibrations while tunneling resonantly into an electronic state of that molecule. After the tunneling event, the molecule is excited, both, vibrationally and electronically, also referred to as "vibronically". In contrast to the IETS described above, vibronic states appear as peaks in the $\mathrm{d}I/\mathrm{d}V$ spectrum and several vibrational modes can be excited at once, as sketched in Figure 3.4c. This includes the multiple excitation of a single mode as well as the combined excitation of different vibrational modes ("progression of progressions") [47]. The probability to excite these modes—and thus their intensity—is given by the Franck-Condon principle [20, 21], as described in Section 2.1.1. However, the vibronic states are subject to the energy level broadening of the electronic states, which most of the time prohibits the observation of the vibronic resonances.

Light Emission in STM

Another inelastic mechanism is the excitation of the surface plasmon in the STM junction, which then emits a photon [69, 70]. These photons from the junction are measured in light emission STM (LE-STM), often with a spectrometer, giving further insights into the electronic properties of the sample [54–60]. The surface plasmon strongly depends on the shape of the junction and thusly on the tip [71], therefore the measurements have to be normalized to the tip-dependent plasmon enhancement function, which can be determined by reference measurements.

3.3. Atomic Force Microscopy

The investigation of isolating surfaces is not possible with an STM, since it relies on a conducting substrate for the tunneling current. Another technique that fills this gap is the atomic force microscope (AFM) which detects the effective forces in the junction and does not rely on a tunneling current. For this, the tip is attached to a flexible cantilever and its deflection is recorded during the measurement.

There are different approaches to probe this deflection, depending on the type of cantilever. For the widely used silicon cantilevers, most of the time a laser beam is reflected from their backside. A displacement or twisting of the cantilever diverts the laser beam, which can be detected by a quadrant photodiode or interferometer. The disadvantage of this method is, that it requires a large distance between cantilever and photodiode to detect small amplitudes.

Another approach uses a piezoelectrical quartz as cantilever [72]. A bending of the quartz causes a small current which can be detected with a simple operational amplifier. These cantilevers are usually much stiffer than their silicon counterparts but the sensor is more compact and capable of measuring deflections down to picometers.

3.3.1. Theory of Dynamic AFM

The choice of cantilever goes hand in hand with the choice of its mode of operation. There are, in general, two different ways to operate an AFM. In the contact mode the tip scratches over the surface and is deflected due to Pauli repulsion (see 3.3.2). This deflection depends linearly on the force and, thus, on the topography of the sample. A very soft and flexible cantilever is required for this mode, in order to prevent changing or damaging the investigated surface. With contact mode AFM, it is rather difficult to achieve a high resolution since the tip often has a large contact area with the surface.

In the non-contact mode (ncAFM or dynamic AFM) the cantilever is oscillating at a given frequency without touching the surface. Assuming the cantilever to be a damped harmonic oscillator driven by an external force F_D its equation of motion is:

$$m\ddot{x} - 2\gamma m\dot{x} + k_0 x = F_D \cos(\omega t), \tag{3.16}$$

with γ being the damping constant, k_0 the spring constant of the cantilever and $F_D = k_D A_D$ the driving force with angular frequency ω. The solution of this equation yields the oscillation amplitude in dependence of ω and driving amplitude A_D:

$$A(\omega) = A_D \frac{\omega_0^2}{\sqrt{4\gamma^2\omega^2 + (\omega_0^2 - \omega^2)^2}}. \tag{3.17}$$

The angular frequency $\omega_0 = \sqrt{k_0/m}$ represents for strongly underdamped systems ($\gamma \ll \omega_0$) also their resonance frequency $f_0 = \omega_0/2\pi$. In the case of a resonant driving force ($\omega = \omega_0$) the equation simplifies to

$$A(\omega_0) = A_D \cdot Q, \tag{3.18}$$

with $Q = \omega_0/2\gamma$ as the quality factor of the cantilever. The phase shift between driving force and oscillator is then given by:

$$\varphi(\omega) = \arctan\left(\frac{2\omega\gamma}{\omega^2 - \omega_0^2}\right). \tag{3.19}$$

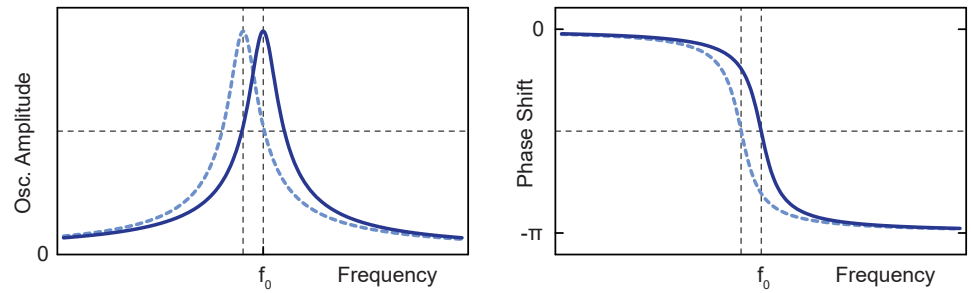

Figure 3.5.: Oscillation amplitude (a) and phase shift (b) of the AFM cantilever in dependence of the driving frequency with (dotted) and without (solid) external force gradient.

The quality factor Q can be determined in experiment by measuring the full width Δf_Q of the resonance curve at height $A_Q = A(\omega_0)/\sqrt{2}$ and by using the relation $Q = f_0/\Delta f_Q$. Another way is by scanning the phase shift $\varphi(\omega)$ and fitting it at resonance frequency with a linear function, as the slope is given by:

$$\left.\frac{\mathrm{d}\varphi}{d\omega}\right|_{\omega_0} = -\frac{2Q}{\omega_0} \tag{3.20}$$

If the cantilever is now subject to an external force gradient $\partial F/\partial z$, it causes an effective change of the spring constant which leads to a change of its resonance frequency. For small oscillation amplitudes, this can be expressed as:

$$f' = \frac{1}{2\pi}\sqrt{\frac{k_0 - \frac{\partial F}{\partial z}}{m}}. \tag{3.21}$$

Assuming that the external force gradient is small compared to the spring constant, a good approximation for the frequency shift is given by [73]:

$$\Delta f = f' - f_0 \approx -\frac{f_0}{2k_0}\frac{\partial F}{\partial z} \tag{3.22}$$

As can be seen, the shift of resonance frequency is directly proportional to the force gradient. Thus, ncAFM can obtain information of the sample without touching or damaging it with the tip. The absolute force acting on the tip can be approximated by measuring the frequency shift $\Delta f(z)$ in dependence of tip height and integrating over z. A more precise method is to deconvolute the force and the tip oscillation [74, 75].

In this work, a frequency modulation AFM (FM-AFM) is used to detect the frequency shift, which is the main observable in ncAFM. A phase-locked loop (PLL) adjusts the driving frequency to keep the phase shift between cantilever and driving force at a constant value of $\varphi = \pi/2$. In this way, the cantilever is always excited at resonance frequency. A second feedback loop is applied to the amplitude of the driving signal in order to keep the oscillation amplitude of the tip constant. A change in this driving amplitude also gives information about possible dissipations due to tip-sample interactions [76–79].

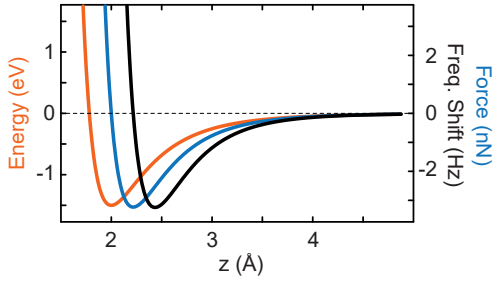

Figure 3.6.: Energy (orange), force (blue) and frequency shift (black) for a Lennard-Jones potential with $\varepsilon = 1.5\,\text{eV}$ and $z_m = 2\,\text{Å}$. For the cantilever a spring constant of $k = 1.8\,\text{kN}\,\text{m}^{-1}$ and center frequency of $f_0 = 27\,\text{kHz}$ was assumed.

3.3.2. Forces in AFM

The probed force gradient in the AFM junction is caused by a combination of different origins. In the following, the three main forces are discussed.

Chemical Forces

The chemical forces are extremely short ranged forces, that occurs between the atom at the very apex of the tip and the sample. A common model for the interaction between two neutral atoms is given by the Lennard-Jones potential [80]:

$$E_{\text{LJ}} = \varepsilon \left[\left(\frac{z_m}{z} \right)^{12} - 2 \left(\frac{z_m}{z} \right)^{6} \right], \tag{3.23}$$

where z_m is the equilibrium distance and ε is the depth of the energy well at z_m. The chemical force can be described by differentiation of the potential:

$$F_{\text{LJ}} = -\frac{\partial E_{LJ}}{\partial z} = 12 \frac{\varepsilon}{z_m} \left[\left(\frac{z_m}{z} \right)^{13} - \left(\frac{z_m}{z} \right)^{7} \right] \tag{3.24}$$

The first term is caused by the Pauli principle: At very close distances (in the range of typical STM junctions) the orbitals of the two atoms overlap. However, the Pauli principle forbids two fermions to occupy the same quantum state, forcing the electrons to states with higher energies. Thus the total energy in the system is increased and causes a repulsive force (Pauli repulsion). On the other hand, at larger distances an attractive van der Waals force acts on the two atoms, caused by fluctuating and/or permanent dipoles.

In Figure 3.6 the Lennard-Jones potential is displayed together with the resulting force and frequency shift. The frequency shift is, in contrast to the tunneling current, non-monotonic with tip-sample distance, like the potential or the force. When the Δf signal is used for the feedback loop of the tip height, it is only possible on one side of the minimum, usually in the attractive regime. The repulsive regime is often used in constant height maps at very close distances, as its short ranged nature yields the best spatial resolution [6].

Mesoscopic van der Waals Force

As the probing tip does not only consist of a single atom, its whole volume has to be taken into account. The Pauli repulsion is too short ranged and can be neglected at larger distances. The van der Waals (vdW) force on the other hand causes a strong attractive background force. A good approximation of an SPM junction is a sphere in front of a flat infinite surface. The vdW force between these two can be calculated by integrating over both volumes, which gives [81]:

$$F_{\mathrm{vdW}} = -\frac{A}{6}\frac{R}{z^2}, \tag{3.25}$$

with A being the material specific Hamaker constant, R the radius of the sphere and z the distance between sphere and surface. The vdW force is usually attractive and causes a large background force, that depends on shape and size of the tip.

Electrostatic Forces

The electrostatic force is the force with the longest range. As the SPM junction is effectively a capacitor with an applied bias voltage, the electric field causes an attractive force of

$$F_{\mathrm{el}} = \frac{\partial E_{el}}{\partial z} = \frac{\partial}{\partial z}\left(\frac{1}{2}CV^2\right) = \frac{1}{2}\frac{\partial C}{\partial z}V^2. \tag{3.26}$$

Approximating the junction again with a sphere of radius R that is significantly larger than the distance z to the surface, the force can be derived from the capacitance [82]:

$$F_{\mathrm{el}} = -\pi\epsilon_0\frac{R}{z}V^2 \tag{3.27}$$

The ability to detect electrostatic forces with an AFM allows for a variety of further measurement techniques. In Kelvin probe force microscopy (KPFM) the electrostatic forces in the junction are minimized by an applied bias voltage. Thus, it is possible to measure the local contact potential difference (LCPD) of the sample. Furthermore, this enables the detection of single-electron charging events [16, 83, 84], the charge state of single atoms [85] or the probing of the intramolecular charge distribution [86, 87].

3.4. Density Functional Theory

Density functional theory (DFT) is a computational method to investigate the electronic structure of a many-body system, *e.g.* a molecule in gas phase. It is based on the two Hohenberg-Kohn theorems, which state that for a given electron density $\rho(\mathbf{r})$ the potential $V(\mathbf{r})$ is uniquely determined [88]. The ground state of a system can thus be described with only three spatial coordinates for $\rho(\mathbf{r})$ instead of $3N$ variables, with N being the number of electrons.

The so called Kohn-Sham potential of the system is described as a functional of the electron density and consists of an external potential due to the charged nuclei, the coulomb interaction between the electrons (Hartree term), and the so called exchange-correlation potential [89]. The last potential includes the many-particle interaction and its functional is, in general, not known in DFT, so it has to be approximated by local-density approximation (LDA) and the generalized gradient approximation (GGA). In so called hybrid functionals these approximations are used together with the exact exchange potential from Hartree-Fock theory. A well known hybrid functional is the "Becke, 3-parameter, Lee-Yang-Parr" functional (B3LYP) [90, 91]. To describe the electronic wave functions of the single atoms, a set of functions is used, the so called "basis set". The resulting molecular orbitals are then described by a linear combination of those functions.

The relaxed structure of a system, *e.g.* a molecule, can be found by minimizing the Kohn-Sham potential with respect to the position of the nuclei in an iterative process. First the second derivative matrix (Hessian) is calculated from the potential and then the position of the nuclei adjusted accordingly and the new potential calculated. These steps are repeated until convergence.

In the relaxed configuration, the Hessian matrix can also be used to calculate the vibrational normal modes of the molecule [92]. By comparing the relaxed structure of the ground state and an electronically excited state (*e.g.* charged) of a molecule in the normal coordinates of these vibrational normal modes, the vibronic spectrum of the molecule can be calculated, as described in *ACS Nano* ***12*** *(2018) 11698*. In this work we performed DFT calculations of single 2,5-bis(3-dodecylthiophen-2-yl)thieno[3,2-b]-thiophene (BTTT) molecules in gas phase, using the Gaussian 09 package [93] with the B3PW91 hybrid functional and 6-31G(d,p) as a basis set for all atoms.

— Chapter 4 —

Experimental Setup

All measurements in this work were done using a combined STM/AFM system in ultra high vacuum (UHV) and at low temperatures (LT), shown in Figure 4.1a. The setup consists of two connected UHV chambers, a preparation chamber and a scanning probe microscope (SPM) chamber, separated by a gate valve. The preparation chamber is equipped with a quadrupole mass spectrometer, two leak valves, a sputter ion gun and three load locks for transfers or mounting evaporators. After preparation the sample can be transferred *in-situ* into the SPM chamber, where a liquid helium (LHe) cryostat keeps the SPM head at a constant temperature of 4.6 K. Both chambers are equipped with ion pumps, keeping UHV conditions (low 10^{-10} mbar) during the experiment without causing mechanical noise. Additionally a titan sublimation pump and a turbo molecular pump are attached to the preparation chamber. The whole setup is suspended on air dampers to further minimize the mechanical coupling between machine and building.

4.1. Scanning Probe Microscope

The scanning probe microscope (SPM) unit is a modified Besocke beetle-type scanner from *SPS-Createc GmbH*. Resting on three outer piezo tubes is a circular copper ramp, with the sensor holder, depicted in Figure 4.1b. Using slip stick motion, the copper ramp can be coarsely moved horizontally and by rotation also vertically, with a maximal lift height of 0.6 mm. The sensor holder is mounted in the middle of the copper ramp to the inner piezo tube and features three electrodes to contact the sensor: two for the piezo current of the tuning fork (see below) and one for the tunneling current. The sensor itself is attached to the sensor holder with two magnets, ensuring the correct orientation of the sensor. The setup also allows for the usage of a simple STM tip holder without tuning fork.

During scanning, the tip position is controlled by the outer piezo tubes. In order to prevent any unwanted slip stick motions, low pass filters are then applied to these piezos. The inner piezo is only used for driving the AFM cantilever, in order to minimize potential cross talk between STM and AFM signal. The whole SPM head is suspended by springs to further reduce mechanical noise from the building.

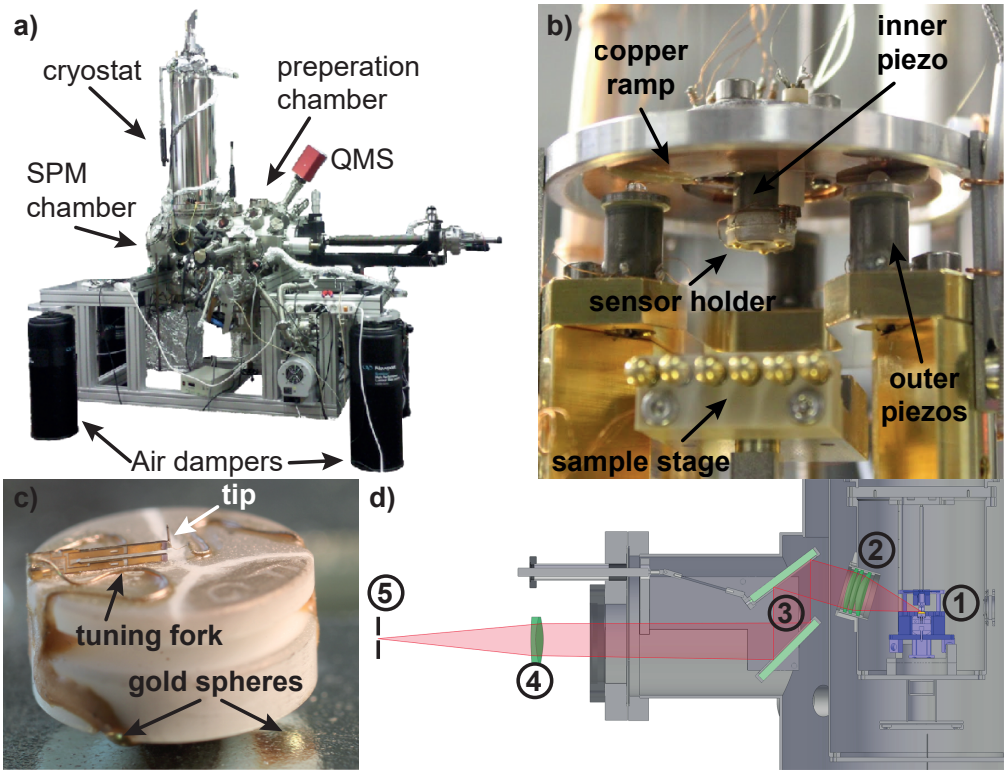

Figure 4.1.: a) SPM system comprising SPM and preparation chamber as well as a liquid helium cryostat, resting on four air dampers. **b)** Besocke beetle-type SPM with the three outer piezo tubes and copper ramp. In this modified version, the inner (main) piezo drives the cantilever of the AFM, whereas the movement is done with the outer piezos. In the bottom, there is the sample stage with six contact pins. **c)** Home-made qPlus tuning fork sensor. The quartz tuning fork is glued onto the macor substrate and contacted via gold wires to two gold spheres. An etched tungsten tip is glued at the end of the free prong and contacted with a very thin gold wire to the third gold sphere. The magnets can be seen as dark areas in the reflexion at the bottom. **d)** Light-Emission setup, similar to the one used in this work. Photons emitted from the STM junction (1) are collected by a lens (2), guided through a borosilicate glass in the LN_2 shield and with two mirrors (3) reflected to a second lens (4) that focuses the beam into the slit of the spectrograph (5). The figure was adapted from [94] and modified.

The SPM is controlled by a *Nanonis SPM controller*. It consists of a realtime controller (RC4) with a digital signal processor (DSP), connected to the following modules:

- Signal Conditioning module (SC4) with analog inputs/outputs connected to the SPM
- Oscillation Controller (OC4) with integrated phase-locked loop (PLL) for AFM
- Adaptation Kit for Createc SPMs

4.1.1. Sensor

The employed sensor is home-made, following the qPlus tuning fork design from Giessibl [95] and shown in Figure 4.1c. It consists of a macor substrate with two magnets for attachment to the sensor holder, and a commercially available 32 768 Hz quartz tuning fork firmly glued on top of the macor, so its upper prong acts as the AFM cantilever. It is contacted to two of the three gold spheres at the bottom, which connect to the electrodes on the sensor holder. At the very end of the cantilever a tungsten tip with 25 µm in diameter is attached with non-conducting glue. The tunneling current is tapped by a 12.5 µm gold wire and contacted to the third gold sphere. Typical values of the qPlus sensors are a spring constant of $1.8\,\mathrm{kN\,m^{-1}}$, center frequency around 28 kHz, and a quality factor in the range of $Q \approx 10\,000$.

Before measurement, the tip is prepared by controlled indentation into the substrate and its quality assured by reference spectra of the clean Au(111) surface.

4.1.2. Light Emission Setup

The setup for the Light-Emission STM (LE-STM) consists of an optical path from the STM junction out of the vacuum chamber to the spectrograph with a CCD camera, as shown in Figure 4.1d. Photons emitted from the junction are collected with an achromatic lens with 45 mm focal length mounted in the He-shield. Through a borosilicate glass shutter in the LN_2 shield the photons are guided by two mirrors out of the SPM chamber. A second achromatic lens focuses the beam into the Princeton Instruments Acton SP-2150i spectrograph with 150 lines/mm and 300 lines/mm gratings. The photons are detected by the LN_2 cooled CCD of the Princeton Instruments Pylon 100BR eXelon.

In this work, the 150 lines/mm grating has been used with an 800 nm blaze. Thus, single photons can be detected within an energy range of 1.2 eV to 2.3 eV.

4.2. Sample Preparation

The substrate we used is a Au single crystal with a polished surface in the (111) direction. Gold is a very inert coinage metal with the (111) surface being the least reactive face. This makes it

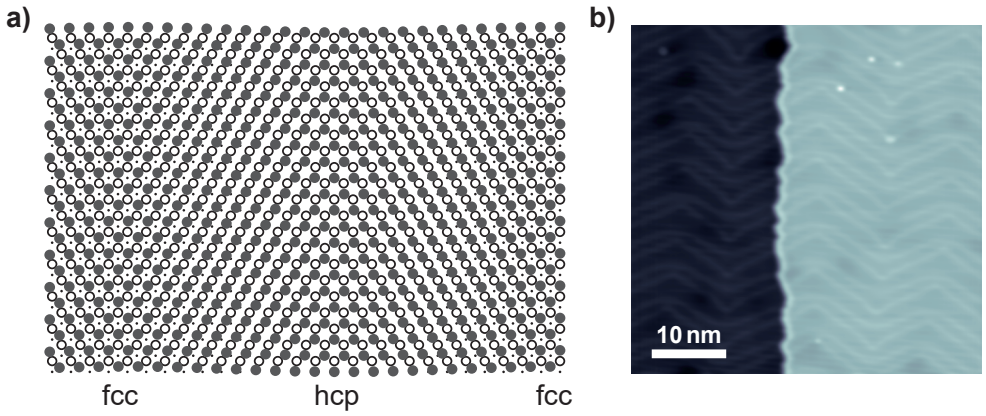

Figure 4.2.: a) Sketch of the herringbone reconstruction of Au(111). A surplus of Au atoms in the top layer leads to fcc and hcp stacking sites of the upper three layers (top layer: gray circles, second layer: black rings, third layer: dots). **b)** STM image of a clean Au(111) surface. The herringbone reconstruction is clearly visible by the bright soliton lines. (1 V/150 pA)

easy to get an atomically clean surface, that couples only weakly to adsorbates.

The crystal was prepared by repeated cycles of sputtering with Ne^+ ions ($p = 10^{-6}$mbar, $V = 1$ kV) and annealing to 820 K. The quality of the sample was confirmed by STM as shown in Fig 4.2b. The pristine Au(111) surface features the characteristic herringbone reconstruction where the upper layer of Au atoms transition between face-center-cubic (fcc) and hexagonal-closed-packed (hcp) stacking (see Figure 4.2a). The areas between these stacking sites are called soliton lines and appear in STM as protruding lines along the $[11\bar{2}]$ direction.

Subsequently, MoS_2 was prepared by backfilling the chamber with H_2S at about 10^{-5}mbar and a submonolayer of molybdenum was deposited from an Omicron EFM-3 metal evaporator onto the Au(111) surface. The sample was then annealed in an H_2S atmosphere for 30 min at about 820 K. The exact parameters varied between preparations to obtain MoS_2 islands of different quality and size.

A submonolayer of 2,5-bis(3-dodecylthiophen-2-yl)thieno[3,2-b]-thiophene (BTTT) molecules was deposited on the MoS_2/Au(111) surface from a Knudsen cell evaporator at 365 K. In order to reduce the mobility of the BTTT molecules on the surface, the sample was kept at 200 K during the deposition.

— Chapter 5 —

MoS_2 as Decoupling Layer

This work consist of two parts to introduce MoS_2 as a decoupling layer on the Au(111) surface. In the first part we investigate the structural and electronic properties of MoS_2 islands grown on a Au(111) surface and the interaction between MoS_2 and the substrate. In the second part, we then use MoS_2 as a decoupling layer for oligothiophene-based molecules. Utilizing the high energy resolution of this system, we perform vibrational analysis with STS and investigate the perturbation potential of an STM tip acting on molecular orbitals.

5.1. MoS_2 on Au(111)

There are several techniques to obtain single-layer islands of MoS_2 on a substrate. Due to its layered structure, it can be exfoliated – similar to graphene – and then placed on the desired surface. This poses an easy way to produce large flakes of MoS_2 with micrometer size in ambient conditions. For high quality MoS_2 on an atomically clean metal surface, a bottom-up-approach by growing MoS_2 in UHV conditions is more feasable. Helveg *et al.* used physical vapour deposition (PVD) to grow small nanoclusters of MoS_2 on a Au(111) surface using an H_2S atmosphere and elementary molybdenum [96]. The resulting triangular MoS_2 nanoclusters were a few nanometer in size and allowed for the study of edge states [97], but were not sufficiently large to investigate the band structure of two dimensional MoS_2. A further improvement of the preparation parameters and conditions allowed for the growth of large MoS_2 islands, tens of nanometer in size, not only on Au(111) [98, 99] but also on Ag(111) [100]. A good control of the coverage, island size and also quality of the MoS_2 islands is now possible, which opened up the investigation of MoS_2/Au(111) by means of surface science techniques, such as ARPES [101, 102], LEED [98] or STM [98, 99, 103].

It also enables the use of MoS_2 as a decoupling layer for adsorbates, such as organic molecules of a few nanometer in size. For this use, a proper understanding is required about how the metal influences the electronic properties of the MoS_2 islands, as well as the structure of the MoS_2/Au(111) interface.

5.1.1. Structural Properties

Epitaxially grown MoS_2 on the Au(111) surface exhibits a moiré pattern which has been observed by LEED and STM techniques [98, 99]. It occurs due to the lattice missmatch between Au(111) ($a_{Au} = 2.88$ Å) and pristine MoS_2 ($a_{MoS_2} = 3.15$ Å), leading to three different stacking areas of the MoS_2/Au(111) interface, as depicted in Figure 5.1: one top-site area, where the bottom sulfer atoms of MoS_2 are placed directly on top of the Au atoms of the uppermost Au layer, and two hollow-site areas where the Mo atoms are either above the upper Au atoms (hcp) or also at a hollow-site (fcc). In STM, the moiré pattern appears as a corrugation of different heights with the top-site being a few pm higher than the two hollow-sites [98]. However, STM provides an energy (bias) dependent apparent topographic height of the sample allowing for only tentative assignements.

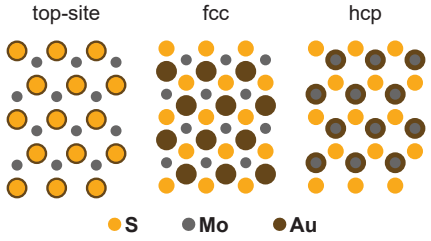

Figure 5.1.: Three different stacking sites in the moiré pattern of MoS_2 on Au(111). In the top-site stacking, the bottom sulfer atoms of MoS_2 are placed on top of the top layer Au atoms. The fcc and hcp structures correspond to two different kinds of hollow-site stacking.

In addition to the moiré structure, also domain boundaries were observed between islands that are rotated by 180° [99]. The presence of two rotated domains complicates a closer investigation with averaging techniques like LEED. By combining AFM and STM one might get a better insight into the exact structure of the MoS_2/Au(111) interface.

In the first part of our publication *Surface Science* ***678*** *(2018) 136-142* we investigated the stacking and orientation of MoS_2 islands on the Au(111) surface. Using AFM we found a topographic height difference between the two hollow-sites, with the hcp site being closer to the Au surface. The apparent height difference between the two hollow-sites in STM on the other hand depends strongly on the applied bias voltage, with the fcc site appearing lower than the hcp site when measuring within the MoS_2 band gap and vice versa when measuring out-of-gap.

Furthermore, we found a unique orientation of the MoS_2 islands with respect to the upper two Au layers of the substrate. Because of the herringbone reconstruction, the Au(111) surface provides two different crystallographic stacking sequences of its upper two layers, namely fcc and hcp terminated regimes separated by so called soliton lines. This leads to MoS_2 islands with two different orientations, rotated by 180°. By tuning the preparation conditions accordingly it is possible to exploit the unique stacking order of MoS_2/Au(111) and allow for the growth of large singly orientated MoS_2 islands. This technique has been introduced shortly after publication of our work [41].

5.1.2. Electronic Properties

The electronic properties of MoS_2 are well studied for the bulk, but also few and single layer MoS_2 have been investigated by experimental [35, 36, 96, 98, 99, 103, 105] and theoretical techniques [34, 37–40]. When grown on Au(111), however, MoS_2 causes some challenges for a theoretical study. Due to the moiré structure the unit cell is too large for a feasable calculation. Some works circumvented this problem by stressing the underlying Au(111) surface [106, 107] or rotating the MoS_2 in order to reduce the size of the unit cell [103, 108]. The band structure obtained in this way exhibits good agreement of the calculated valance bands with experimental observations from ARPES [101]. These experiments show that the valence band minimum (VBM) at the $\bar{K}$ point is located at −1.39 eV below the Fermi energy. Due to a lack of Au states in this area of the Brillouin zone, the VBM is nearly unperturbed and exhibits a clear spin splitting of 145 meV at the $\bar{K}$ valleys, similar to free standing MoS_2 [101]. Additionally, the band at $\bar{K}$ is a mixture of the Mo $d_{x^2-y^2}$, d_{xy} and the S p_x, p_y orbitals, giving it an overall in-plane character, which reduces the interaction with the Au(111) substrate further. Even the buckling due to the Moiré structure has no influence on the VBM [101]. The valence band around the $\bar{\Gamma}$ point on the other hand is strongly hybridized with the Au d-bands, due to its out-of-plane character [101, 103]. This interaction should be strongly affected by the buckling of the Moiré structure, but couldn't be observed in ARPES due to the broadening of the band.

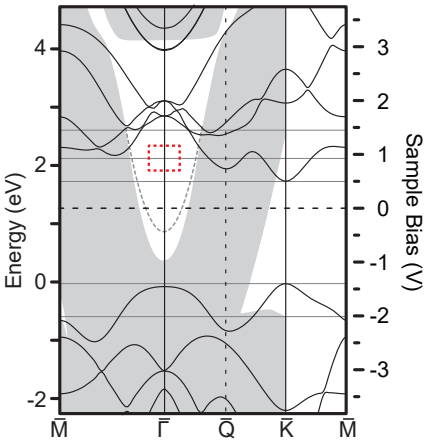

Figure 5.2.: Calculated band structure of MoS_2 without spin-orbit coupling. In the background the Au(111) states are sketched in gray [104]. The sample bias scale on the right is adjusted to match the VBM at −1.4 V and the CBM at 0.5 V.

The conduction band (CB) of MoS_2/Au(111) is not as well studied as the valence band, since it is challenging to measure unoccupied states with ARPES techniques. Using time resolved ARPES, the conduction band minimum (CBM) is determined to be at the $\bar{K}$ point with an energy of 0.5 eV above E_F [102], which is – similar to the VBM – located within a gap of the Au(111) bands. Otherwise, only theoretical studies have given an insight into the band structure of the conduction bands of MoS_2/Au(111) so far. An STM is the perfect tool to measure these unoccupied states of MoS_2/Au(111) as well as the valence band at the $\bar{\Gamma}$ point with spatial resolution. A recent study by Zhang *et al.* introduced an STS measurement technique to gain information about the parallel momentum of an electronic state, thus allowing for the exploration of the Brillouin zone by means of STS [66]. For a more detailed explaination of this technique see Methods 3.2.1.

We used this method in the second part of *Surface Science* ***678*** *(2018) 136-142* to investigate the band structure of the occupied and unoccupied states of MoS_2/Au(111) with spatial resolution

in the real and reciprocal space. For the valence band we confirmed the strong hybridization between the MoS_2 and Au(111) states at $\bar{\Gamma}$[101, 103]. These states are indeed influenced by the moiré pattern, as the VB at $\bar{\Gamma}$ is shifted by 300 meV towards the Fermi energy for both hollow-sites compared to the state at top-site. This shift could be due to a stronger hybridization with the Au(111) surface or a stronger electronic screening [109]. The VBM at the $\bar{K}$ point proved not to be detectable with an STM, as the tunneling current at its energy is dominated by the Au states around $\bar{\Gamma}$.

For the unoccupied states, we were able to detect the CBM at 0.5 eV and found the CBs at the $\bar{\Gamma}$ point at 1.4 eV. This also hints towards an interaction of the CB with the Au(111) states, as the bands at $\bar{\Gamma}$ are predicted to be at higher energy compared to the CBM. Additionally, we found a state at 0.9 eV located at the $\bar{\Gamma}$ point marked by the red box in Figure 5.2. As no calculation has predicted an additional band at energies halfway between the CBM and the CBs at $\bar{\Gamma}$, it probably originates from the complex interaction with the Au(111) substrate. Moreover, it appears to be sensitive to the stacking order by showing slight differences between all three stacking sites, which strengthens the assumption that it probably occurs due to the MoS_2/Au(111) interface.

All these results point towards a complex interaction between MoS_2 and the Au(111) substrate. While the electronic bands are mostly intact, the underlying metal shifts the bands at some points in the Brillouin zone and in some areas even hybridizes. A comparison to quasi-freestanding monolayer MoS_2 without a Au layer directly under it would therefore be of great interest.

5.2. Quasi-Freestanding MoS_2

Defects in MoS_2 are of great interest and topic of many studies [110–117]. Particularly intrinsic defects like sulfur or molybdenum vacancies or substitute impurities have been investigated both experimentally and theoretically. These kinds of defects can also be found in MoS_2 grown epitaxially on Au(111) and will be discussed in further publications. In this work, we will focus on the MoS_2/Au(111) interaction and defects occuring at the interface.

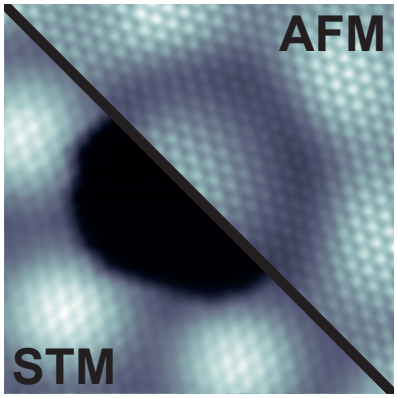

Figure 5.3.: Constant height image of quasi-freestanding MoS_2 depicting the current channel (STM) and frequency shift (AFM). $V_b = 5\,\text{meV}$ during the scan and feedback opened at $V_b = 0.8\,\text{V}/I = 200\,\text{pA}$.

Dependig on the preparation parameters, we find highly symmetric areal defects in our MoS_2, which are investigated in *Nano Lett.* ***8*** *(2016) 5163–5168*. Using the combination of conductance, force gradient, and electroluminescence measurements we found the areal defects to be patches of quasi-freestanding MoS_2. During the growth process, vacancy islands in the Au(111) substrate of a few nm in size can form and are then stabilized under the MoS_2. These patches of quasi-freestanding MoS_2 do not provide any density of states within the electronic gap, making them nearly invisible for STM at low bias voltages. Constant height AFM images on the other hand revealed an unperturbed complete upper sulfer layer, and hence intact MoS_2, as shown in Figure 5.3. The missing density of states is explained by the lack of hybridization with the Au(111) bands, partially restoring the unperturbed band structure of freestanding single layer MoS_2. The former strongly-hybridized valence band around $\bar{\Gamma}$ is not broadened anymore but appears as a sharp peak in the $\mathrm{d}I/\mathrm{d}V$ spectrum, as shown in Figure 5.4. Additionally, the band gap at the $\bar{\Gamma}$ point becomes gradually larger when measured along such a quasi-freestanding patch of MoS_2.

The results from the tunneling spectroscopy were backed by the electroluminescence, which showed no density of states within the quasi band gap. Also, no features of constant photon energy—independent from the bias voltage—were found, ruling out radiative relaxations of excitons in the junction.

The state at 0.9 eV described in Section 5.1.2 seems to disappear when there is a vacancy island under the MoS_2, supporting the assumption that it occurs due to the MoS_2/Au(111) interface. This is, however, a tentative conclusion, as the data are not unambiguous enough to proof the vanishing of the state at 0.9 eV.

As we are interested in the utilization of MoS_2 as decoupling layer for molecular adsorbates, these quasi-freestanding patches are of special interest. The almost completely vanishing density of states within the band gap could further amplify the decoupling properties of MoS_2.

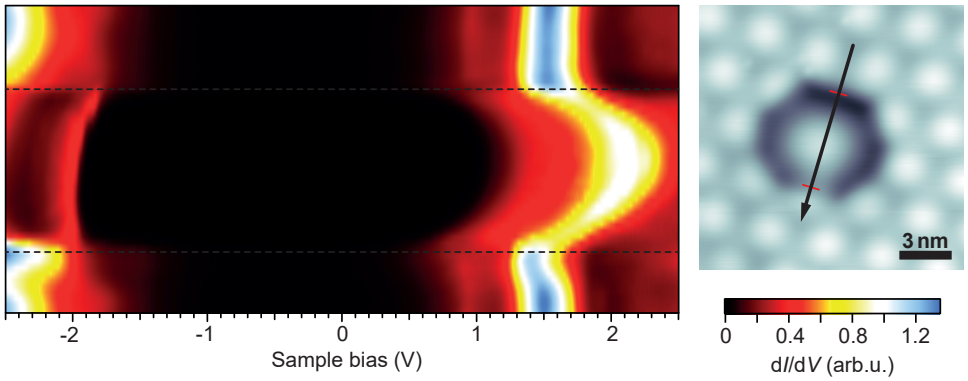

Figure 5.4.: Color plot of spatially resolved tunneling conductance, taken by 50 dI/dV spectra across a “pit’, as shown in the topography image taken at 2.5 V/2 nA). The feedback was opened before each spectrum at 2.5 V/2 nA. The dotted lines in the color plot correspond to the red dotted lines in the topography image and mark the edges of the ”pit“. A clear shift of the conduction bands to higher energies is visible, as well as the sharpening of the valence band around −2 V.

5.3. Utilizing MoS_2/Au(111) for Vibrational Analysis

Probing the electronic states of a molecular adsorbate via tunneling spectroscopy can excite the molecule vibrationally due to inelastic tunneling. These so called vibronic resonances are usually hard to detect, as they are, like the elastic resonance, subject to lifetime broadening. Vibrational energies of molecules are in the range of a few millielectronvolts (meV) up to a couple of hundreds of meV, being in the same order of magnitude as the energy broadening of the peaks. Thus, it is very challenging to investigate the vibronic features of a molecule with an STM.

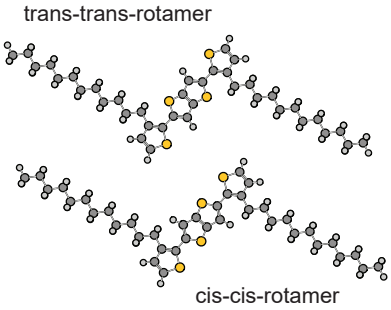

Figure 5.5.: Two possible rotamers of BTTT, which differ by the orientation of the thienothiophene group in the center.

Utilizing decoupling layers between molecule and substrate increases the energy resolution to tens of meV, enabling the measurement of single prominent vibronic resonances in molecules [4, 10, 11, 14, 24–26, 47, 48, 118, 119]. The resolution can be further enhanced by measuring the second derivative of the tunneling current, similar to inelastic tunneling spectroscopy (IETS) measurements around the Fermi energy [4, 24]. By fitting equidistant peaks (usually gaussian or lorentzian) to the spectrum, the vibrational energy $\hbar\omega$ is determined and can be compared to DFT calculation, in order to estimate the corresponding vibrational mode. However, the low energy modes are still not distinguishable by tunneling spectroscopy. The analysis gets more challenging, when several vibrational modes are contributing to the vibronic spectrum, leading to a "progression of progressions" [47].

This is why most of the time the vibrational analysis in STS does not gain as much insight about the molecular adsorbate as compared to optical techniques. For example, the low energy resolution prohibits to use the vibronic fingerprint in a spectrum in order to distinguish between similar molecules, which differ by rotation of a single bond or include different isotopes. To do this kind of analysis in STM, an even higher energy resolution is required.

In *ACS Nano* ***12*** *(2018) 11698* we show that MoS_2 proves to be an excellent decoupling layer, providing the necessary energy resolution for vibrational analysis. As molecular adsorbate the oligothiophene-based molecule 2,5-bis(3-dodecylthiophen-2-yl)thieno[3,2-b]-thiophene (BTTT; shown in Figure 5.5) [120] was deposited on the MoS_2/Au(111) substrate. We observed on this system the – to our knowledge – unprecedented energy resolution of less than 6 meV in the tunneling spectrum. It enabled the observation of many vibronic states of the positive ion resonance (often referred to as HOMO) of BTTT. These vibronic spectra with resonances of varying height and spacings could indeed be used as a vibronic fingerprint, that allows to distinguish between two types of rotamers of BTTT, that only differ by the rotation of a thienothiophene group (see Figure 5.5). Using gas-phase DFT calculations of single BTTT

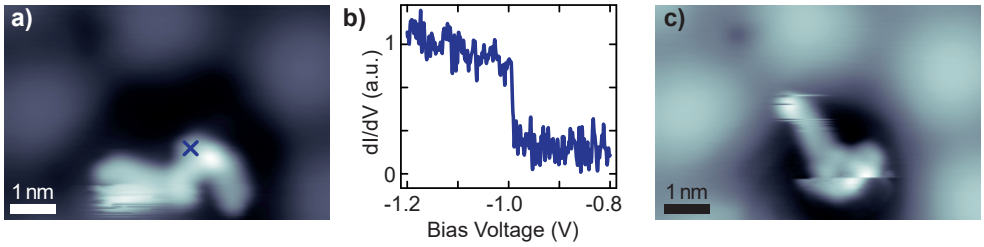

Figure 5.6.: A single BTTT molecule on a patch of quasi-freestanding MoS_2 before (a) and after (c) the attempt to take a dI/dV spectrum (b). Without the stabilization of neighboring molecules, a single BTTT is too mobile to perform dI/dV spectroscopy.

molecules, we were able to fully reproduce the vibronic spectra of the two rotamers, identifying them unambiguously.

The direct comparison between the measurements of BTTT on MoS_2/Au(111) and the DFT calculation of BTTT in gas-phase gives further proof that MoS_2 is an excellent decoupling layer. By fitting only the low-energy flank of the elastic peak, the lifetime of the excited state could be estimated to be at least 300 fs. Furthermore, no additional peaks arising from MoS_2 were found in the vibronic spectra, which indicates a negligible electron-phonon coupling of the material.

Unfortunately, no measurements could be performed on single BTTT molecules on a quasi-freestanding patch of MoS_2 (see Section 5.2). The high relaxation energy of BTTT and thus the easily excited vibrational modes cause a very unstable junction. As can be seen in Figure 5.6 single BTTT molecules move and rotate during the dI/dV spectra, as they are not stabilized by neighboring molecules. To investigate the decoupling properties of quasi-freestanding MoS_2 a technique has to be developed to grow or move ordered molecular islands onto such a patch or use different molecules that are not prone to change during spectroscopy.

5.4. Investigation of the Perturbation Potential Caused by STM Tip

The extraordinarily high energy resolution due to the MoS_2 decoupling layer allows us to investigate effects which are otherwise hidden or not unambiguously identified. In such a case common approximations may not be sufficient anymore and a more refined model has to be considered. One example is the approximation of constant potential along the surface ("plate capacitor model"). For most cases it is sufficient to consider only the vertical axis of the junction. In reality, however, the tip has a certain (often unknown) shape that leads to an inhomogeneous potential in all three Cartesian axes. For AFM, which is sensitive to the long range electrostatic forces, this effect is well known and studied, *i.e.* in the case of Kelvin probe measurements [121, 122]. In STM and STS it has also been observed in the form of so called "charging rings" at field induced charging events of adsorbates or impurities [24, 123–125]. This is most often the case if the adsorbate is not lying directly on the metal substrate but on a decoupling layer. In this case, the STM junction has to be considered as a double tunneling barrier with the applied bias voltage dropping over both the vacuum between tip and adsorbate, and the decoupling layer (see Figure 5.7). Assuming a realistic tip model, the ratio between these two barriers varies with the vertical as well as with the lateral tip-adsorbate distances. The voltage drop directly depends on this ratio, which leads to the observation of those "charging rings" in the $\mathrm{d}I/\mathrm{d}V$ maps. The effect of the voltage drop in a double barrier junction can also be observed as an apparent shift of the adsorbates ion resonances in the $\mathrm{d}I/\mathrm{d}V$ spectrum. This, however, has only been reported in dependence of the vertical tip-adsorbate distance, assuming the plate capacitor model [4, 24, 126, 127].

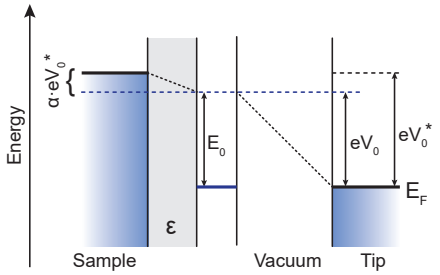

Figure 5.7.: Energy scheme of a double barrier junction with applied voltage V^* and decoupling layer with permittivity ε. A part α of the voltage drops over the decoupling layer, reducing the applied potential to an adsorbate. Hence a higher voltage than E_0/e is required, in order to tunnel into an electronic state of energy E_0.

In *Phys. Rev. B* ***100*** *(2019) 035410* we investigate the perturbation potential due to the inhomogeneous electric potential in the STM junction, *i.e.* its dependency on the lateral tip-adsorbate distance. Again using BTTT molecules adsorbed on MoS_2/Au(111), we utilize their delocalized positive ion resonance (PIR) along the thiophene-based backbone. Due to the inhomogeneity of the electric potential, we measured an apparent intramolecular shift in energy of the PIR along the BTTT. Furthermore, we showed that the electric potential applied to the adsorbate might not only be caused by the bias voltage. Additional charges in the junction, for example due to a dipole located at the tip, can also contribute a non-negligible electrostatic potential. By functionalizing the tip with a Cl atom, we created such a tip dipole and investigated its perturbation potential to the PIR. These two origins of the perturbation potential can be distinguished by comparing the energies of elastic and vibronic satellite states of the PIR. As

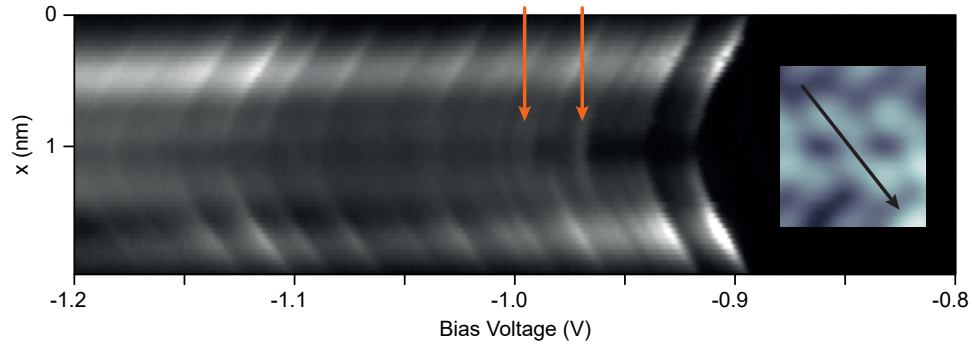

Figure 5.8.: Line of 50 dI/dV spectra taken at constant height along the backbone of a BTTT molecule (see inset). In the center of the molecule, additional peaks appear (marked by red arrows) that do not match the calculated vibronic modes. Feedback opened at the end of the thiophene backbone at −1.2 V/300 pA.

such, it becomes a useful tool to characterize an STM tip and measure the effect of possible static charges in the junction.

Please note, that this shift due to a tip position dependent perturbation potential could in general also be observed with less energy resolution on other substrates. However, in those cases it is hard to distinguish between a shift of all vibronic peaks (as discussed above) or a relative change of intensity, that might shift the centroid [26]. Both of these effects are observed for BTTT on MoS_2/Au(111) and are distinguishable.

As can be seen in Figure 5.8 there are additional resonances in the dI/dV spectrum when the tip is placed in the center of the BTTT. These peaks appear to be additional vibrational modes of the molecule, that are excited by a different mechanism (compared to the vibronic states), which is possibly similar to inelastic tunneling spectroscopy (IETS). The exact nature of these additional resonances is subject to further investigations.

— Chapter 6 —

Conclusion & Outlook

In this thesis, we have introduced molybdenum disulfide (MoS_2) as a decoupling layer for adsorbates on the Au(111) surface. The investigations were performed with a combined scanning tunneling and atomic force microscope (STM/AFM) at low temperatures and supported by density functional theory (DFT) calculations.

In the first part, we investigated the structural and electronic properties of MoS_2 on the Au(111) surface. We found that MoS_2 islands always have the same orientation with respect to the underlying Au surface and assigned the exact stacking sequences to three different sites of the well known moiré pattern of MoS_2/Au(111). These different stacking sequences proved to have an effect on the electronic band structure of MoS_2. One conduction band was found around the $\bar{\Gamma}$ point at energies 0.4 eV above the conduction band minimum and occurs most likely due to the MoS_2/Au(111) interface. Comparison with quasi freestanding MoS_2 patches confirmed the influence of the underlying Au(111) substrate. Tunneling spectroscopy and electroluminescence experiments showed that the vacancy islands beneath the MoS_2 monolayer lift the hybridization with the Au(111) surface and lead to a vanishing of all density of state within the expected band gap of MoS_2.

In the second part of this work, we used MoS_2 as a decoupling layer and explored the possibilities, gained by the higher energy resolution. In the first publication, we performed vibrational analysis with tunneling spectroscopy and distinguished single rotamers of the 2,5-bis(3-dodecylthiophen-2-yl)thieno[3,2-b]-thiophene (BTTT) molecule by their vibronic fingerprint in the positive ion resonance (PIR). Furthermore, we demonstrated that the tunneling spectrum could be fully reproduced with DFT calculations by the simple Franck-Condon picture. In the second publication, we used the high energy resolution to map the perturbation potential of different tips, acting on the electronic states of the BTTT molecules. Comparison between the vibronic states and the elastic state enabled us to distinguish between bias-dependent perturbation potentials (due to a voltage drop over the MoS_2) and bias-independent perturbation potentials caused by static tip dipoles.

This already establishes MoS_2 as an excellent decoupling layer and opens the door for further investigations, *i.e.* the mechanisms of tunneling inelastically into a molecular orbital.

The newly gained high energy resolution allows for the observation of additional peaks in the middle of the BTTT molecule (see Figure 5.8), which are not predicted by the Franck-Condon principle. Further research might lead to a tunneling model merging the on-resonant (vibronics) and off-resonant (IETS) tunneling mechanisms.

Of special interest are, of course, the quasi freestanding MoS_2 patches, also referred to as "pits". The most obvious utilization would be for an even better decoupling than the normal MoS_2/Au(111) interface. However, first measurements with BTTT showed a high mobility of the molecule on such a "pit", making the tunneling spectroscopy challenging (see Figure 5.6). With better suited molecules or anchoring mechanisms the decoupling properties of freestanding MoS_2 might lead to an even better energy resolution.

Another field of topic might be to use the patches as chemically inert defects to locally perturb the electronic structure of one dimensional adsorbates. One-dimensional quantum dots in graphene nanoribbons (GNR) are a system of high interest and are usually achieved by varying the width of the GNR or by introducing substituents [128–130]. By placing a GNR on top of such a "pit", the change of environment might lead to such confined states without changing the structure of the GNR.

We have already performed first experiments with armchair graphene nanoribbons (AGNR) on MoS_2/Au(111). The zigzag ends of AGNR have spin-polarized edge states, where the occupied edge state (OES) and the unoccupied edge state (UES) on the same end are of opposite spin [131, 132]. At positive bias voltages the OES of the AGNR on MoS_2 is shifted above the Fermi energy of the substrate and thus depopulated, due to the potential drop in the MoS_2. These charging events can be observed as a parabola in Figure 6.1a, marked by the red arrow. We find the UES localized at the GNR termination at higher bias voltages around 1.7 V, outside of the MoS_2 band gap. The calculated and measured $\mathrm{d}I/\mathrm{d}V$ maps of the edge states are displayed in Figure 6.1b.

Additionally, a second resonance is found around 200 meV below the UES. Its spatial distribution in the $\mathrm{d}I/\mathrm{d}V$ map differs from the expected shape of an edge state and shows an additional nodal plane. A possible origin for this state is the combination of the electron in the UES and the hole in the OES to an excitonic state, as sketched in Figure 6.1c. Due to the spin polarization of the edge states, such an excitonic state could not relax by recombination. These excitons are also referred to as dark excitons. Around 1.9 V another resonance can be found at the end of the AGNR and might be an interband excitonic state [133]. In this picture, the hole of the OES forms an interband exciton with the conduction band. In order to prove this tentative explanation of the additional states, time dependent DFT measurements are required, to calculate the wave functions of the excitons and compare them with the experimental results.

The utilization of MoS_2 as a decoupling layer for molecular adsorbates bids for many more investigations of many different systems. The high energy resolution allows us to gain a closer look at their underlying mechanisms and should help us in our journey to explore the fascinating world of nanophysics.

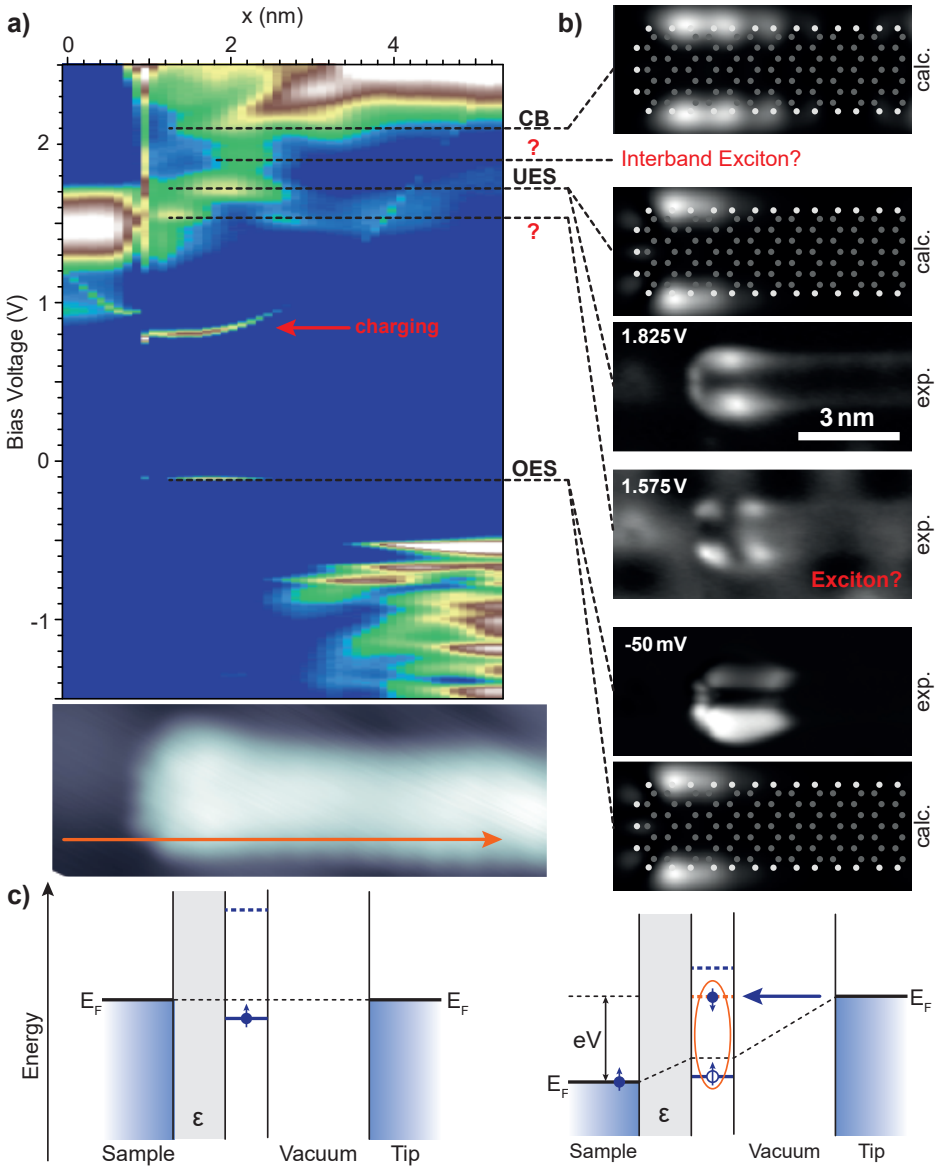

Figure 6.1.: a) Line of dI/dV spectra taken along a GNR on MoS_2/Au(111). The occupied edge state (OES) is located around −0.1 V and can be charged at positive bias voltage (red arrow). The valence bands can be seen at energies below −0.5 V. At higher positive bias voltages, the unoccupied edge state (UES) is visible around 1.7 V and the conduction bands (CB) above 2 V. Two additional resonances are found at energies about 200 meV below the UES and CB and might correspond to excitonic states. (FB opened before each spectrum at 2.5 V/300 pA). **b)** Constant current (300 pA) dI/dV maps and calculated constant height dI/dV maps (with atomic structure) from another GNR are shown to the right, corresponding to the features marked in the map. **c)** Energy scheme of the charging event and formation of the excitonic state. The OES (blue solid line) is shifted above the E_F of the sample, due to the potential drop in the MoS_2, and filled with a hole as the electron tunnels into the substrate. An electron tunneling into the UES could form an excitonic state (orange dotted line) at energies below the UES (blue dotted line).

Bibliography

[1] W. R. Browne and B. L. Feringa. Light Switching of Molecules on Surfaces. *Annu. Rev. Phys. Chem.*, 60(1):407–428, 2009. doi:10.1146/annurev.physchem.040808.090423.

[2] B. K. Pathem, S. A. Claridge, Y. B. Zheng, and P. S. Weiss. Molecular Switches and Motors on Surfaces. *Annu. Rev. Phys. Chem.*, 64(1):605–630, 2013. doi:10.1146/annurev-physchem-040412-110045.

[3] J. L. Zhang, J. Q. Zhong, J. D. Lin, W. P. Hu, K. Wu, G. Q. Xu, A. T. S. Wee, and W. Chen. Towards single molecule switches. *Chem. Soc. Rev.*, 44:2998–3022, 2015. doi:10.1039/C4CS00377B.

[4] X. H. Qiu, G. V. Nazin, and W Ho. Vibronic States in Single Molecule Electron Transport. *Phys. Rev. Lett.*, 92(20):206102, 2004. doi:10.1103/PhysRevLett.92.206102.

[5] J. Repp, G. Meyer, S. M. Stojković, A. Gourdon, and C. Joachim. Molecules on Insulating Films: Scanning-Tunneling Microscopy Imaging of Individual Molecular Orbitals. *Phys. Rev. Lett.*, 94(2):026803, 2005. doi:10.1103/PhysRevLett.94.026803.

[6] L. Gross, F. Mohn, N. Moll, P. Liljeroth, and G. Meyer. The Chemical Structure of a Molecule Resolved by Atomic Force Microscopy. *Science*, 325(5944):1110–1114, 2009. doi:10.1126/science.1176210.

[7] M. Sterrer, T. Risse, U. Martinez Pozzoni, L. Giordano, M. Heyde, H.-P. Rust, G. Pacchioni, and H.-J. Freund. Control of the Charge State of Metal Atoms on Thin MgO Films. *Phys. Rev. Lett.*, 98:096107, 2007. doi:10.1103/PhysRevLett.98.096107.

[8] F. Donati, S. Rusponi, S. Stepanow, C. Wäckerlin, A. Singha, L. Persichetti, R. Baltic, K. Diller, F. Patthey, E. Fernandes, J. Dreiser, Ž. Šljivančanin, K. Kummer, C. Nistor, P. Gambardella, and H. Brune. Magnetic remanence in single atoms. *Science*, 352(6283):318–321, 2016. doi:10.1126/science.aad9898.

[9] J. Cho, J. Smerdon, L. Gao, Ö. Süzer, J. R. Guest, and N. P. Guisinger. Structural and Electronic Decoupling of C_{60} from Epitaxial Graphene on SiC. *Nano Lett.*, 12(6):3018–3024, 2012. doi:10.1021/nl3008049.

[10] A. Riss, S. Wickenburg, L. Z. Tan, H-Z. Tsai, Y. Kim, J. Lu, A. J. Bradley, M. M. Ugeda, K. L. Meaker, K. Watanabe, T. Taniguchi, A. Zettl, F. R. Fischer, S. G. Louie, and M. F. Crommie. Imaging and Tuning Molecular Levels at the Surface of a Gated Graphene Device. *ACS Nano*, 8(6):5395–5401, 2014. doi:10.1021/nn501459v.

[11] S. Wickenburg, J. Lu, J. Lischner, H-Z. Tsai, A. A. Omrani, A. Riss, C. Karrasch, A. Bradley, H. S. Jung, R. Khajeh, D. Wong, K. Watanabe, T. Taniguchi, A. Zettl, A. H. C. Neto, S. G. Louie, and M. F. Crommie. Tuning Charge and Correlation Effects for a Single Molecule on a Graphene Device. *Nat. Commun.*, 7(13553):1, 2016. doi:10.1038/ncomms13553.

[12] P. Järvinen, S. Hämäläinen, K. Banerjee, P. Häkkinen, M. Ijäs, A. Harju, and P. Liljeroth. Molecular Self-Assembly on Graphene on SiO_2 and h-BN Substrates. *Nano Lett.*, 13(7):3199–3204, 2013. doi:10.1021/nl401265f.

[13] S. Joshi, F. Bischoff, R. Koitz, D. Ecija, K. Seufert, A. P. Seitsonen, J. Hutter, K. Diller, J. I. Urgel, H. Sachdev, J. V. Barth, and W. Auwärter. Control of Molecular Organization and Energy Level Alignment by an Electronically Nanopatterned Boron Nitride Template. *ACS Nano*, 8(1):430–442, 2013. doi:10.1021/nn406024m.

[14] F. Schulz, R. Drost, S. Hämäläinen, and P. Liljeroth. Templated Self-Assembly and Local Doping of Molecules on Epitaxial Hexagonal Boron Nitride. *ACS Nano*, 7(12):11121–11128, 2013. doi:10.1021/nn404840h.

[15] F. D. Natterer, F. Patthey, and H. Brune. Distinction of Nuclear Spin States with the Scanning Tunneling Microscope. *Phys. Rev. Lett.*, 111(17):175303, 2013. doi:10.1103/PhysRevLett.111.175303.

[16] W. Steurer, J. Repp, L. Gross, I. Scivetti, M. Persson, and G. Meyer. Manipulation of the Charge State of Single Au Atoms on Insulating Multilayer Films. *Phys. Rev. Lett.*, 114(3):036801, 2015. doi:10.1103/PhysRevLett.114.036801.

[17] S. Fatayer, B. Schuler, W. Steurer, I. Scivetti, J. Repp, L. Gross, M. Persson, and G. Meyer. Reorganization Energy upon Charging a Single Molecule on an Insulator Measured by Atomic Force Microscopy. *Nat. Nanotechnol.*, 13:376–380, 2018. doi:10.1038/s41565-018-0087-1.

[18] I. Fernández Torrente, K. J. Franke, and J. I. Pascual. Spectroscopy of C60 single molecules: the role of screening on energy level alignment. *J. Phys.: Condens. Matter*, 20(18):184001, 2008. doi:10.1088/0953-8984/20/18/184001.

[19] L. Bartels, G. Meyer, K.-H. Rieder, D. Velic, E. Knoesel, A. Hotzel, M. Wolf, and G. Ertl. Dynamics of Electron-Induced Manipulation of Individual CO Molecules on Cu(111). *Phys. Rev. Lett.*, 80(9):2004–2007, 1998. doi:10.1103/PhysRevLett.80.2004.

[20] J. Franck and E. G. Dymond. Elementary processes of photochemical reactions. *Trans. Faraday Soc.*, 21:536–542, 1926. doi:10.1039/TF9262100536.

[21] E. Condon. A Theory of Intensity Distribution in Band Systems. *Phys. Rev.*, 28(6):1182–1201, 1926. doi:10.1103/PhysRev.28.1182.

[22] J. W. Gadzuk. Inelastic Resonance Scattering, Tunneling, and Desorption. *Phys. Rev. B.*, 44(24):13466, 1991. doi:10.1103/PhysRevB.44.13466.

[23] K. J. Franke, G. Schulze, and J. I. Pascual. Competition of Superconducting Phenomena and Kondo Screening at the Nanoscale. *Science*, 332(6032):940–944, 2011. doi:10.1126/science.1202204.

[24] G. V. Nazin, S. W. Wu, and W Ho. Tunneling rates in electron transport through double-barrier molecular junctions in a scanning tunneling microscope. *Proc. Natl. Acad. Sci. U.S.A.*, 102(25):8832–8837, 2005. doi:10.1073/pnas.0501171102.

[25] S. Wang, W. Wang, Y. Hong, B. Zhong, and N. Lin. Vibronic State Assisted Resonant Transport in Molecules Strongly Anchored at an Electrode. *Phys. Rev. B.*, 83(11):115431, 2011. doi:10.1103/PhysRevB.83.115431.

[26] N. Pavliček, I. Swart, J. Niedenführ, G. Meyer, and J. Repp. Symmetry Dependence of Vibration-Assisted Tunneling. *Phys. Rev. Lett.*, 110(13):136101, 2013. doi:10.1103/PhysRevLett.110.136101.

[27] J. Repp, G. Meyer, S. Paavilainen, F. E. Olsson, and M. Persson. Scanning Tunneling Spectroscopy of Cl Vacancies in NaCl Films: Strong Electron-Phonon Coupling in Double-Barrier Tunneling Junctions. *Phys. Rev. Lett.*, 95(22):225503, 2005. doi:10.1103/PhysRevLett.95.225503.

[28] H. Topsøe, B. S. Clausen, and F. E. Massoth. *Hydrotreating Catalysis*, pages 1–269. Springer Berlin Heidelberg, 1996. doi:10.1007/978-3-642-61040-0_1.

[29] J. V. Lauritsen, S. Helveg, E. Lægsgaard, I. Stensgaard, B. S. Clausen, H. Topsøe, and F. Besenbacher. Atomic-Scale Structure of Co–Mo–S Nanoclusters in Hydrotreating Catalysts. *J. Catal.*, 197(1):1 – 5, 2001. doi:https://doi.org/10.1006/jcat.2000.3088.

[30] D. Yang, S. Jiménez Sandoval, W. M. R. Divigalpitiya, J. C. Irwin, and R. F. Frindt. Structure of single-molecular-layer MoS_2. *Phys. Rev. B*, 43(14):12053–12056, 1991. doi:10.1103/PhysRevB.43.12053.

[31] K. K. Kam and B. A. Parkinson. Detailed photocurrent spectroscopy of the semiconducting group VIB transition metal dichalcogenides. *J. Phys. Chem.*, 86(4):463–467, 1982. doi:10.1021/j100393a010.

[32] R. Coehoorn, C. Haas, J. Dijkstra, C. J. F. Flipse, R. A. de Groot, and A. Wold. Electronic structure of $MoSe_2$, MoS_2, and WSe_2. I. Band-structure calculations and photoelectron spectroscopy. *Phys. Rev. B*, 35(12):6195–6202, 1987. doi:10.1103/PhysRevB.35.6195.

[33] Katsuyoshi Kobayashi and Jun Yamauchi. Electronic structure and scanning-tunneling-microscopy image of molybdenum dichalcogenide surfaces. *Phys. Rev. B*, 51(23):17085–17095, 1995. doi:10.1103/PhysRevB.51.17085.

[34] T. Li and G. Galli. Electronic Properties of MoS_2 Nanoparticles. *J. Phys. Chem. C*, 111(44):16192–16196, 2007. doi:10.1021/jp075424v.

[35] A. Splendiani, L. Sun, Y. Zhang, T. Li, J. Kim, C. Chim, G. Galli, and F. Wang. Emerging Photoluminescence in Monolayer MoS_2. *Nano Lett.*, 10(4):1271, 2010. doi:10.1021/nl903868w.

[36] K. F. Mak, C. Lee, J. Hone, J. Shan, and T. F. Heinz. Atomically Thin MoS_2: A New Direct-Gap Semiconductor. *Phys. Rev. Lett.*, 105(13):136805, 2010. doi:10.1103/PhysRevLett.105.136805.

[37] T Cheiwchanchamnangij and W. R. L. Lambrecht. Quasiparticle band structure calculation of monolayer, bilayer, and bulk MoS_2. *Phys. Rev. B*, 85(20):205302, 2012. doi:10.1103/PhysRevB.85.205302.

[38] H. Komsa and A. V. Krasheninnikov. Effects of confinement and environment on the electronic structure and exciton binding energy of MoS_2 from first principles. *Phys. Rev. B*, 86(24):241201, 2012. doi:10.1103/PhysRevB.86.241201.

[39] D. Y. Qiu, F. H. da Jornada, and S. G. Louie. Optical Spectrum of MoS_2: Many-Body Effects and Diversity of Exciton States. *Phys. Rev. Lett.*, 111(21):216805, 2013. doi:10.1103/PhysRevLett.111.216805.

[40] Z. Y. Zhu, Y. C. Cheng, and U. Schwingenschlögl. Giant spin-orbit-induced spin splitting in two-dimensional transition-metal dichalcogenide semiconductors. *Phys. Rev. B*, 84(15):153402, 2011. doi:10.1103/PhysRevB.84.153402.

[41] H. Bana, E. Travaglia, L. Bignardi, P. Lacovig, C. E. Sanders, M. Dendzik, M-Michiardi, M. Bianchi, D. Lizzit, F. Presel, D. De Angelis, N. Apostol, P. Kumar Das, J. Fujii, I. Vobornik, R. Larciprete, A. Baraldi, P. Hofmann, and S. Lizzit. Epitaxial growth of single-orientation high-quality MoS_2 monolayers. *2D Mater.*, 5(3):035012, 2018. doi:10.1088/2053-1583/aabb74.

[42] C. Bombis, F. Ample, L. Lafferentz, H. Yu, S. Hecht, C. Joachim, and L. Grill. Single Molecular Wires Connecting Metallic and Insulating Surface Areas. *Angew. Chem., Int. Ed.*, 48(52):9966–9970, 2009. doi:10.1002/anie.200904645.

[43] C. J. Villagomez, T. Zambelli, S. Gauthier, A. Gourdon, S. Stojkovic, and C. Joachim. STM images of a large organic molecule adsorbed on a bare metal substrate or on a thin insulating layer: Visualization of HOMO and LUMO. *Surf. Sci.*, 603:1526–1532, 2009. doi:10.1016/j.susc.2008.10.057.

[44] L. Gross, N. Moll, F. Mohn, A. Curioni, G. Meyer, F. Hanke, and M. Persson. High-Resolution Molecular Orbital Imaging Using a *p*-Wave STM Tip. *Phys. Rev. Lett.*, 107(5):086101, 2011. doi:10.1103/PhysRevLett.107.086101.

[45] A. J. Heinrich, J. A. Gupta, C. P. Lutz, and D. M. Eigler. Single-Atom Spin-Flip Spectroscopy. *Science*, 306(5695):466–469, 2004. doi:10.1126/science.1101077.

[46] S. Li, D. Yuan, A. Yu, G. Czap, R. Wu, and W. Ho. Rotational Spectromicroscopy: Imaging the Orbital Interaction between Molecular Hydrogen and an Adsorbed Molecule. *Phys. Rev. Lett.*, 114(20):206101, 2015. doi:10.1103/PhysRevLett.114.206101.

[47] N. A. Pradhan, N. Liu, and W. Ho. Vibronic Spectroscopy of Single C_{60} Molecules and Monolayers with the STM. *J. Phys. Chem. B*, 109(17):8513, 2005. doi:10.1021/jp045289b.

[48] S. W. Wu, G. V. Nazin, X. Chen, X. H. Qiu, and W. Ho. Control of Relative Tunneling Rates in Single Molecule Bipolar Electron Transport. *Phys. Rev. Lett.*, 93(23):236802, 2004. doi:10.1103/PhysRevLett.93.236802.

[49] P. Hapala, G. Kichin, C. Wagner, F. S. Tautz, R. Temirov, and P. Jelínek. Mechanism of high-resolution STM/AFM imaging with functionalized tips. *Phys. Rev. B*, 90(8):085421, 2014. doi:10.1103/PhysRevB.90.085421.

[50] G. Binnig, H. Rohrer, Ch. Gerber, and E. Weibel. Surface Studies by Scanning Tunneling Microscopy. *Phys. Rev. Lett.*, 49(1):57–61, 1982. doi:10.1103/PhysRevLett.49.57.

[51] B. C. Stipe, M. A. Rezaei, and W. Ho. Single-molecule vibrational spectroscopy and microscopy. *Science*, 12(5370):1732–1735, 1998. doi:10.1126/science.280.5370.1732.

[52] K. J. Franke and J. I. Pascual. Effects of Electron-Vibration Coupling in Transport through Single Molecules. *J. Phys.: Condens. Matter*, 24(39):394002, 2012. doi:10.1088/0953-8984/24/39/394002.

[53] J. van der Lit, M.P. Boneschanscher, D. Vanmaekelbergh, M. Ijäs, A. Uppstu, M. Ervasti, A. Harju, P. Liljeroth, and I. Swart. Suppression of electron–vibron coupling in graphene nanoribbons contacted via a single atom. *Nat. Commun.*, 4(2023):1, 2013. doi:10.1038/ncomms3023.

[54] X. H. Qiu, G. V. Nazin, and W. Ho. Vibrationally Resolved Fluorescence Excited with Submolecular Precision. *Science*, 299(5606):542–546, 2003. doi:10.1126/science.1078675.

[55] H. Imada, K. Miwa, M. Imai-Imada, S. Kawahara, K. Kimura, and Y. Kim. Real-space investigation of energy transfer in heterogeneous molecular dimers. *Nature*, 538:364, 2016. doi:10.1038/nature19765.

[56] Y. Zhang, Y. Luo, Y. Zhang, Y. Yu, Y. Kuang, L. Zhang, Q.-S. Meng, Y. Luo, J.-L. Yang, Z.-C. Dong, and J. G. Hou. Visualizing coherent intermolecular dipole–dipole coupling in real space. *Nature*, 531:623, 2016. doi:10.1038/nature17428.

[57] B. Doppagne, M. C. Chong, E. Lorchat, S. Berciaud, M. Romeo, H. Bulou, A. Boeglin, F. Scheurer, and G. Schull. Vibronic Spectroscopy with Submolecular Resolution from STM-Induced Electroluminescence. *Phys. Rev. Lett.*, 118:127401, 2017. doi:10.1103/PhysRevLett.118.127401.

[58] H. Imada, K. Miwa, M. Imai-Imada, S. Kawahara, K. Kimura, and Y. Kim. Single-molecule investigation of energy dynamics in a coupled plasmon-exciton system. *Phys. Rev. Lett.*, 119:013901, 2017. doi:10.1103/PhysRevLett.119.013901.

[59] B. Doppagne, M. C. Chong, H. Bulou, A. Boeglin, F. Scheurer, and G. Schull. Electrofluorochromism at the single-molecule level. *Science*, 361(6399):251–255, 2018. doi:10.1126/science.aat1603.

[60] K. Kimura, K. Miwa, H. Imada, M. Imai-Imada, S. Kawahara, J. Takeya, M. Kawai, M. Galperin, and Y. Kim. Selective triplet exciton formation in a single molecule. *Nature*, 570:210, 2019. doi:10.1038/s41586-019-1284-2.

[61] C. F. Hirjibehedin, C. P. Lutz, and A. J. Heinrich. Spin Coupling in Engineered Atomic Structures. *Science*, 312(5776):1021–1024, 2006. doi:10.1126/science.1125398.

[62] N. Tsukahara, K. Noto, M. Ohara, S. Shiraki, N. Takagi, Y. Takata, J. Miyawaki, M. Taguchi, A. Chainani, S. Shin, and M. Kawai. Adsorption-Induced Switching of Magnetic Anisotropy in a Single Iron(II) Phthalocyanine Molecule on an Oxidized Cu(110) Surface. *Phys. Rev. Lett.*, 102:167203, 2009. doi:10.1103/PhysRevLett.102.167203.

[63] J. Tersoff and D. R. Hamann. Theory and Application for the Scanning Tunneling Microscope. *Phys. Rev. Lett.*, 50(25):1998, 1983. doi:10.1103/PhysRevLett.50.1998.

[64] J Bardeen. Tunnelling from a Many-Particle Point of View. *Phys. Rev. Lett.*, 6(2):57, 1961. doi:10.1103/PhysRevLett.6.57.

[65] J. Buisset. *Tieftemperatur Rastertunnelmikroskopie*. Wissenschaft & Technik Verlag, 1996.

[66] C. Zhang, Y. Chen, A. Johnson, M.-Y. Li, L.-J. Li, P. C. Mende, R. M. Feenstra, and C.-K. Shih. Probing Critical Point Energies of Transition Metal Dichalcogenides: Surprising Indirect Gap of Single Layer WSe_2. *Nano Letters*, 15(10):6494–6500, 2015. doi:10.1021/acs.nanolett.5b01968.

[67] C.-l. Chiang, C. Xu, Z. Han, and W. Ho. Real-space imaging of molecular structure and chemical bonding by single-molecule inelastic tunneling probe. *Science*, 344(6186):885–888, 2014. doi:10.1126/science.1253405.

[68] A. J. Heinrich, C. P. Lutz, J. A. Gupta, and D. M. Eigler. Molecule Cascades. *Science*, 298(5597):1381–1387, 2002. doi:10.1126/science.1076768.

[69] J. K. Gimzewski, B. Reihl, J. H. Coombs, and R. R. Schlittler. Photon emission with the scanning tunneling microscope. *Z. Phys. B: Condens. Matter*, 72(4):497–501, 1988. doi:10.1007/BF01314531.

[70] P. Johansson, R. Monreal, and P. Apell. Theory for light emission from a scanning tunneling microscope. *Phys. Rev. B*, 42(14):9210–9213, 1990. doi:10.1103/PhysRevB.42.9210.

[71] J. Aizpurua, S. P. Apell, and R. Berndt. Role of tip shape in light emission from the scanning tunneling microscope. *Phys. Rev. B*, 62(3):2065–2073, 2000. doi:10.1103/PhysRevB.62.2065.

[72] P. Günther, U. Ch. Fischer, and K. Dransfeld. Scanning near-field acoustic microscopy. *Appl. Phys. B: Lasers Opt.*, 48(1):89–92, 1989. doi:10.1007/BF00694423.

[73] F. J. Giessibl. Advances in atomic force microscopy. *Rev. Mod. Phys.*, 75:949–983, 2003. doi:10.1103/RevModPhys.75.949.

[74] F. J. Giessibl. A direct method to calculate tip–sample forces from frequency shifts in frequency-modulation atomic force microscopy. *Appl. Phys. Lett.*, 78(1):123–125, 2001. doi:10.1063/1.1335546.

[75] J. E. Sader and S. P. Jarvis. Accurate formulas for interaction force and energy in frequency modulation force spectroscopy. *Appl. Phys. Lett.*, 84(10):1801–1803, 2004. doi:10.1063/1.1667267.

[76] C. Lotze, M. Corso, K. J. Franke, F. von Oppen, and J. I. Pascual. Driving a Macroscopic Oscillator with the Stochastic Motion of a Hydrogen Molecule. *Science*, 338(6108):779–782, 2012. doi:10.1126/science.1227621.

[77] M. Langer, M. Kisiel, R. Pawlak, F. Pellegrini, G. E. Santoro, R. Buzio, A. Gerbi, G. Balakrishnan, A. Baratoff, E. Tosatti, and E. Meyer. Giant frictional dissipation peaks and charge-density-wave slips at the $NbSe_2$ surface. *Nat. Mater.*, 13:173, 2014. doi:10.1038/nmat3836.

[78] Y. Miyahara, A. Roy-Gobeil, and P. Grutter. Quantum state readout of individual quantum dots by electrostatic force detection. *Nanotechnology*, 28(6):064001, 2017. doi:10.1088/1361-6528/aa5261.

[79] L. L. Patera, F. Queck, P. Scheurer, and J. Repp. Mapping orbital changes upon electron transfer with tunnelling microscopy on insulators. *Nature*, 566:245, 2019. doi:10.1038/s41586-019-0910-3.

[80] J. E. Jones and S. Chapman. On the determination of molecular fields. —II. From the equation of state of a gas. *Proc. R. Soc. A*, 106(738):463–477, 1924. doi:10.1098/rspa.1924.0082.

[81] H.C. Hamaker. The London—van der Waals attraction between spherical particles. *Physica*, 4(10):1058 – 1072, 1937. doi:10.1016/S0031-8914(37)80203-7.

[82] L. Olsson, N. Lin, V. Yakimov, and R. Erlandsson. A method for in situ characterization of tip shape in ac-mode atomic force microscopy using electrostatic interaction. *J. Appl. Phys.*, 84(8):4060–4064, 1998. doi:10.1063/1.368618.

[83] C. Wagner, M. F. B. Green, P. Leinen, T. Deilmann, P. Krüger, M. Rohlfing, R. Temirov, and F. S. Tautz. Scanning Quantum Dot Microscopy. *Phys. Rev. Lett.*, 115(2):026101, 2015. doi:10.1103/PhysRevLett.115.026101.

[84] N. Kocić, S. Decurtins, S.-X. Liu, and J. Repp. Forces from periodic charging of adsorbed molecules. *J. Chem. Phys.*, 146(9):092327, 2017. doi:10.1063/1.4975607.

[85] L. Gross, F. Mohn, P. Liljeroth, J. Repp, F. J. Giessibl, and G. Meyer. Measuring the Charge State of an Adatom with Noncontact Atomic Force Microscopy. *Science*, 324(5933):1428–1431, 2009. doi:10.1126/science.1172273.

[86] F. Mohn, L. Gross, N. Moll, and G. Meyer. Imaging the charge distribution within a single molecule. *Nat. Nanotechnol.*, 7:227–231, 2012. doi:10.1038/nnano.2012.20.

[87] B. Schuler, S.-X. Liu, Y. Geng, S. Decurtins, G. Meyer, and L. Gross. Contrast Formation in Kelvin Probe Force Microscopy of Single π-Conjugated Molecules. *Nano Letters*, 14(6):3342–3346, 2014. doi:10.1021/nl500805x.

[88] P. Hohenberg and W. Kohn. Inhomogeneous Electron Gas. *Phys. Rev.*, 136(3B):B864–B871, 1964. doi:10.1103/PhysRev.136.B864.

[89] W. Kohn and L. J. Sham. Self-Consistent Equations Including Exchange and Correlation Effects. *Phys. Rev.*, 140(4A):A1133–A1138, 1965. doi:10.1103/PhysRev.140.A1133.

[90] K. Kim and K. D. Jordan. Comparison of Density Functional and MP2 Calculations on the Water Monomer and Dimer. *J. Phys. Chem.*, 98(40):10089–10094, 1994. doi:10.1021/j100091a024.

[91] P. J. Stephens, F. J. Devlin, C. F. Chabalowski, and M. J. Frisch. Ab Initio Calculation of Vibrational Absorption and Circular Dichroism Spectra Using Density Functional Force Fields. *J. Phys. Chem.*, 98(45):11623–11627, 1994. doi:10.1021/j100096a001.

[92] J. W. Ochterski. Vibrational analysis in gaussian, 1999. http://gaussian.com/vib/ (visited 01.06.2018).

[93] M. J. Frisch, G. W. Trucks, H. B. Schlegel, G. E. Scuseria, M. A. Robb, J. R. Cheeseman, G. Scalmani, V. Barone, G. A. Petersson, H. Nakatsuji, X. Li, M. Caricato, A. Marenich, J. Bloino, B. G. Janesko, R. Gomperts, B. Mennucci, H. P. Hratchian, J. V. Ortiz, A. F. Izmaylov, and *et al.* Gaussian 09, Revision D.01, 2009. Gaussian Inc. Wallingford CT.

[94] Gunnar Schulze. PhD thesis, Freie Universität Berlin, 2009. http://www.diss.fu-berlin.de/diss/receive/FUDISS_thesis_000000016942.

[95] F. J. Giessibl. Atomic resolution on Si(111)-(7×7) by noncontact atomic force microscopy with a force sensor based on a quartz tuning fork. *Appl. Phys. Lett.*, 76(11):1470–1472, 2000. doi:10.1063/1.126067.

[96] S. Helveg, J. V. Lauritsen, E. Lægsgaard, I. Stensgaard, J. K. Nørskov, B. S. Clausen, H. Topsøe, and F. Besenbacher. Atomic-Scale Structure of Single-Layer MoS_2 Nanoclusters. *Phys. Rev. Lett.*, 84(5):951–954, 2000. doi:10.1103/PhysRevLett.84.951.

[97] M. V. Bollinger, J. V. Lauritsen, K. W. Jacobsen, J. K. Nørskov, S. Helveg, and F. Besenbacher. One-Dimensional Metallic Edge States in MoS_2. *Phys. Rev. Lett.*, 87(19):196803, 2001. doi:10.1103/PhysRevLett.87.196803.

[98] S. G. Sørensen, H. G. Füchtbauer, A. K. Tuxen, A. S. Walton, and J. V. Lauritsen. Structure and electronic properties of in situ synthesized single-layer MoS_2 on a gold surface. *ACS Nano*, 8(7):6788–6796, 2014. doi:10.1021/nn502812n.

[99] S. S. Grønborg, S. Ulstrup, M. Bianchi, M. Dendzik, . E. Sanders, J. V. Lauritsen, P. Hofmann, and J. A. Miwa. Synthesis of Epitaxial Single-Layer MoS_2 on Au(111). *Langmuir*, 31(35):9700–9706, 2015. doi:10.1021/acs.langmuir.5b02533.

[100] M. Dendzik, A. Bruix, M. Michiardi, A. S. Ngankeu, M. Bianchi, J. A. Miwa, B. Hammer, P. Hofmann, and C. E. Sanders. Substrate-induced semiconductor-to-metal transition in monolayer WS_2. *Phys. Rev. B*, 96(23):235440, 2017. doi:10.1103/PhysRevB.96.235440.

[101] J. A. Miwa, S. Ulstrup, S. G. Sørensen, M. Dendzik, A. Grubišić Čabo, M. Bianchi, J. V. Lauritsen, and P. Hofmann. Electronic Structure of Epitaxial Single-Layer MoS_2. *Phys. Rev. Lett.*, 114(4):046802, 2015. doi:10.1103/PhysRevLett.114.046802.

[102] A. Grubišić Čabo, J. A. Miwa, S. S. Grønborg, J. M. Riley, J. C. Johannsen, C. Cacho, O. Alexander, R. T. Chapman, E. Springate, M. Grioni, J. V. Lauritsen, P. D. C. King, P. Hofmann, and S. Ulstrup. Observation of Ultrafast Free Carrier Dynamics in Single Layer MoS_2. *Nano Lett.*, 15(9):5883, 2015. doi:10.1021/acs.nanolett.5b01967.

[103] A. Bruix, J. A. Miwa, N. Hauptmann, D. Wegner, S. Ulstrup, S. S. Grønborg, C. E. Sanders, M. Dendzik, A. Grubišić Čabo, M. Bianchi, J. V. Lauritsen, A. A. Khajetoorians, B. Hammer, and P. Hofmann. Single-layer MoS_2 on Au(111): Band gap renormalization and substrate interaction. *Phys. Rev. B*, 93(16):165422, 2016. doi:10.1103/PhysRevB.93.165422.

[104] N. Takeuchi, C. T. Chan, and K. M. Ho. Au(111): A theoretical study of the surface reconstruction and the surface electronic structure. *Phys. Rev. B*, 43(17):13899–13906, 1991. doi:10.1103/PhysRevB.43.13899.

[105] Y. Shi, W. Zhou, A.-Y. Lu, W. Fang, Y.-H. Lee, A. L. Hsu, S. Min Kim, K. K. Kim, H. Y. Yang, L.-J. Li, J.-. Idrobo, and J. Kong. van der Waals Epitaxy of MoS2 Layers Using Graphene As Growth Templates. *Nano Lett.*, 12(6):2784–2791, 2012. doi:10.1021/nl204562j.

[106] C. Gong, L. Colombo, R. M. Wallace, and K. Cho. The Unusual Mechanism of Partial Fermi Level Pinning at Metal–MoS_2 Interfaces. *Nano Lett.*, 14(4):1714–1720, 2014. doi:10.1021/nl403465v.

[107] C. Tsai, F. Abild-Pedersen, and J. K. Nørskov. Tuning the MoS_2 Edge-Site Activity for Hydrogen Evolution via Support Interactions. *Nano Lett.*, 14(3):1381–1387, 2014. doi:10.1021/nl404444k.

[108] M. Farmanbar and G. Brocks. Controlling the Schottky barrier at MoS_2/metal contacts by inserting a BN monolayer. *Phys. Rev. B*, 91(16):161304, 2015. doi:10.1103/PhysRevB.91.161304.

[109] M. Rösner, C. Steinke, M. Lorke, C. Gies, F. Jahnke, and T. O. Wehling. Two-Dimensional Heterojunctions from Nonlocal Manipulations of the Interactions. *Nano Lett.*, 16(4):2322, 2016. doi:10.1021/acs.nanolett.5b05009.

[110] W. Zhou, X. Zou, S. Najmaei, Z. Liu, Y. Shi, J. Kong, J. Lou, P. M. Ajayan, B. I. Yakobson, and J.-C. Idrobo. Intrinsic Structural Defects in Monolayer Molybdenum Disulfide. *Nano Lett.*, 13(6):2615–2622, 2013. doi:10.1021/nl4007479.

[111] Q. Ma, P. M. Odenthal, J. M., D. Le, C. S. Wang, Y. Zhu, T. Chen, D. Sun, K. Yamaguchi, T. Tran, M. Wurch, J. L. McKinley, J. Wyrick, K. Magnone, T. F. Heinz, T. S. Rahman, R. Kawakami, and L. Bartels. Controlled argon beam-induced desulfurization of monolayer molybdenum disulfide. *J. Phys.: Condens. Matter*, 25(25):252201, 2013. doi:10.1088/0953-8984/25/25/252201.

[112] J.-Y. Noh, H. Kim, and Y.-S. Kim. Stability and electronic structures of native defects in single-layer MoS_2. *Phys. Rev. B*, 89(20):205417, 2014. doi:10.1103/PhysRevB.89.205417.

[113] K. C. Santosh, R. C. Longo, R. Addou, R. M. Wallace, and K. Cho. Impact of intrinsic atomic defects on the electronic structure of MoS_2 monolayers. *Nanotechnology*, 25(37):375703, 2014. doi:10.1088/0957-4484/25/37/375703.

[114] R. Addou, L. Colombo, and R. M. Wallace. Surface Defects on Natural MoS_2. *ACS Appl. Mater. Interfaces*, 7(22):11921–11929, 2015. doi:10.1021/acsami.5b01778.

[115] C. González, B. Biel, and Y. J. Dappe. Theoretical characterisation of point defects on a MoS_2 monolayer by scanning tunnelling microscopy. *Nanotechnology*, 27(10):105702, 2016. doi:10.1088/0957-4484/27/10/105702.

[116] C. González, Y. J. Dappe, and B. Biel. Reactivity Enhancement and Fingerprints of Point Defects on a MoS_2 Monolayer Assessed by ab Initio Atomic Force Microscopy. *J. Phys. Chem. C*, 120(30):17115–17126, 2016. doi:10.1021/acs.jpcc.6b05998.

[117] J. Kunstmann, T. B. Wendumu, and G. Seifert. Localized defect states in MoS_2 monolayers: Electronic and optical properties. *Phys. Status Solidi B*, 254(4):1600645, 2017. doi:10.1002/pssb.201600645.

[118] T. Frederiksen, K. J. Franke, A. Arnau, G. Schulze, J. I. Pascual, and N. Lorente. Dynamic Jahn-Teller Effect in Electronic Transport through Single C_{60} Molecules. *Phys. Rev. B*, 78(23):233401, 2008. doi:10.1103/PhysRevB.78.233401.

[119] T. L. Cocker, D. Peller, P. Yu, J. Repp, and R. Huber. Tracking the Ultrafast Motion of a Single Molecule by Femtosecond Orbital Imaging. *Nature*, 539:263–267, 2016. doi:10.1038/nature19816.

[120] L. Zhang, F. Liu, Y. Diao, H. S. Marsh, N. S. Colella, A. Jayaraman, T. P. Russell, S. C.B. Mannsfeld, and A. L. Briseno. The Good Host: Formation of Discrete One-Dimensional Fullerene “Channels" in Well-Ordered Poly(2,5-bis(3-alkylthiophen-2-yl)thieno[3,2-b]thiophene) Oligomers. *J. Am. Chem. Soc.*, 136(52):18120–18130, 2014. doi:10.1021/ja510976n.

[121] A. Sadeghi, A. Baratoff, S. A. Ghasemi, S. Goedecker, T. Glatzel, S. Kawai, and E. Meyer. Multiscale approach for simulations of Kelvin probe force microscopy with atomic resolution. *Phys. Rev. B*, 86(7):075407, 2012. doi:10.1103/PhysRevB.86.075407.

[122] J. L. Neff and P. Rahe. Insights into Kelvin probe force microscopy data of insulator-supported molecules. *Phys. Rev. B*, 91(8):085424, 2015. doi:10.1103/PhysRevB.91.085424.

[123] N. A. Pradhan, N. Liu, C. Silien, and W. Ho. Atomic Scale Conductance Induced by Single Impurity Charging. *Phys. Rev. Lett.*, 94(7):076801, 2005. doi:10.1103/PhysRevLett.94.076801.

[124] K. Teichmann, M. Wenderoth, S. Loth, R. G. Ulbrich, J. K. Garleff, A. P Wijnheijmer, and P. M. Koenraad. Controlled Charge Switching on a Single Donor with a Scanning Tunneling Microscope. *Phys. Rev. Lett.*, 101(7):076103, 2008. doi:10.1103/PhysRevLett.101.076103.

[125] I. Fernández-Torrente, D. Kreikemeyer-Lorenzo, A. Stróżecka, K. J. Franke, and J. I. Pascual. Gating the Charge State of Single Molecules by Local Electric Fields. *Phys. Rev. Lett.*, 108(3):036801, 2012. doi:10.1103/PhysRevLett.108.036801.

[126] G. Reecht, F. Scheurer, V. Speisser, Y. J. Dappe, F. Mathevet, and G. Schull. Electroluminescence of a Polythiophene Molecular Wire Suspended between a Metallic Surface and the Tip of a Scanning Tunneling Microscope. *Phys. Rev. Lett.*, 112(4):047403, 2014. doi:10.1103/PhysRevLett.112.047403.

[127] B. Warner, F. El Hallak, H. Prüser, J. Sharp, M. Persson, A. J. Fisher, and C. F. Hirjibehedin. Tunable magnetoresistance in an asymmetrically coupled single-molecule junction. *Nat. Nanotechnol.*, 10:259, 2015. doi:10.1038/NNANO.2014.326.

[128] D. Prezzi, D. Varsano, A. Ruini, and E. Molinari. Quantum dot states and optical excitations of edge-modulated graphene nanoribbons. *Phys. Rev. B*, 84:041401, 2011. doi:10.1103/PhysRevB.84.041401.

[129] S. Wang, N. Kharche, E. Costa Girão, X. Feng, K. Müllen, V. Meunier, R. Fasel, and P. Ruffieux. Quantum dots in graphene nanoribbons. *Nano Letters*, 17(7):4277–4283, 2017. doi:10.1021/acs.nanolett.7b01244.

[130] E. Carbonell-Sanromà, P. Brandimarte, R. Balog, M. Corso, S. Kawai, A. Garcia-Lekue, S. Saito, S. Yamaguchi, E. Meyer, D. Sánchez-Portal, and J. I. Pascual. Quantum dots embedded in graphene nanoribbons by chemical substitution. *Nano Letters*, 17(1):50–56, 2017. doi:10.1021/acs.nanolett.6b03148.

[131] Y.-W. Son, M. L. Cohen, and S. G. Louie. Energy Gaps in Graphene Nanoribbons. *Phys. Rev. Lett.*, 97:216803, 2006. doi:10.1103/PhysRevLett.97.216803.

[132] S. Wang, L. Talirz, C. A. Pignedoli, X. Feng, K. Müllen, R. Fasel, and P. Ruffieux. Giant edge state splitting at atomically precise graphene zigzag edges. *Nat. Commun.*, 7:11507. doi:10.1038/ncomms11507.

[133] Y. Lu, S. Wei, J. Jin, W. Lu, and L. Wang. Competition of edge effects on the electronic properties and excitonic effects in short graphene nanoribbons. *New J. Phys.*, 18(12):123033, 2016. doi:10.1088/1367-2630/aa5116.

— Appendix A —

Publications

Publications Related to this Thesis

The following list comprises all publications discussed in this thesis and is ordered by their date of publication. The experiments and analyses were conducted by the author of this thesis under supervision of Katharina Franke and Christian Lotze.

- **Nano Letters 16, 5163 (2016):** The author of this thesis performed most experimental measurements and analyses. The electroluminiscence experiments were carried out by Christian Lotze. All authors contributed to the interpretation of the data. The initial draft was written by Christian Lotze in close collaboration with the author of this thesis. All authors contributed to the writing of the final version of this manuscript.

- **Surface Science 678, 136 (2018)**: The author of this thesis performed the experimental measurements and analyses. The DFT calculation of the MoS_2 band structure was performed by Christian Lotze. All authors contributed to the interpretation of the data. The initial draft was written by the author of this thesis and all authors contributed to the writing of the final version of this manuscript.

- **ACS Nano 12, 11698 (2018)**: The author of this thesis performed the experimental measurements and analyses as well as the DFT calculations. All authors contributed to the interpretation of the data. The initial draft was written by the author of this thesis and all authors contributed to the writing of the final version of this manuscript. Lei Zhang and Alejandro Briseno provided the oligothiophene-based molecules.

- **Physical Review B 100, 035410 (2019)**: The author of this thesis performed the experimental measurements and analyses as well as the DFT calculations. All authors contributed to the interpretation of the data. The initial draft was written by the author of this thesis and all authors contributed to the writing of the final version of this manuscript. Lei Zhang and Alejandro Briseno provided the oligothiophene-based molecules.

Publications not Related to this Thesis

- **Physical Review B 89, 235409 (2014)**
  T. R. Umbach, M. Bernien, C. F. Hermanns, L. L. Sun, H. Mohrmann, K. E. Hermann, A. Krüger, N. Krane, Z. Yang, F. Nickel, Y.-M. Chang, K. J. Franke, J. I. Pascual, and W. Kuch

  Title: Site-specific bonding of copper adatoms to pyridine end groups mediating the formation of two-dimensional coordination networks on metal surfaces

  doi: 10.1103/PhysRevB.89.235409

- **ACS Nano 13, 7031 (2019)**
  G. Reecht, N. Krane, C. Lotze, K. J. Franke

  Title: π -Radical Formation by Pyrrolic H Abstraction of Phthalocyanine Molecules on Molybdenum Disulfide

  doi: 10.1021/acsnano.9b02117

- **In Preparation**
  G. Reecht, N. Krane, C. Lotze, L. Zhang, A. L. Briseno, K. J. Franke

  Working title: Inelastic Excitation Mechanisms in Tunneling Spectroscopy Beyond the Franck-Condon Model

A.1. Nano Letters 16, 5163 (2016)

Nils Krane, Christian Lotze, Julia M. Läger, Gaël Reecht, and Katharina J. Franke

Electronic Structure and Luminescence of Quasi-Freestanding MoS_2 Nanopatches on Au(111)

doi: 10.1021/acs.nanolett.6b02101

A.2. Surface Science 678, 136 (2018)

Nils Krane, Christian Lotze, and Katharina J. Franke

Moiré structure of MoS_2 on Au(111): Local structural and electronic properties

doi: 10.1016/j.susc.2018.03.015

A.3. ACS Nano 12, 11698 (2018)

Nils Krane, Christian Lotze, Gaël Reecht, Lei Zhang, Alejandro L. Briseno and Katharina J. Franke

High Resolution Vibronic Spectra of Molecules on Molybdenum Disulfide Allow for Rotamer Identification

doi: 10.1021/acsnano.8b07414

A.4. Physical Review B 100, 035410 (2019)

Nils Krane, Christian Lotze, Nils Bogdanoff, Gaël Reecht, Lei Zhang, Alejandro L. Briseno and Katharina J. Franke

Mapping the perturbation potential of metallic and dipolar tips in tunneling spectroscopy on MoS_2

doi: 10.1103/PhysRevB.100.035410

Editors' Suggestion

Mapping the perturbation potential of metallic and dipolar tips in tunneling spectroscopy on MoS_2

Nils Krane,[1] Christian Lotze,[1,*] Nils Bogdanoff,[1] Gaël Reecht,[1] Lei Zhang,[2] Alejandro L. Briseno,[2] and Katharina J. Franke[1]

[1]*Fachbereich Physik, Freie Universität Berlin, Arnimallee 14, 14195 Berlin, Germany*

[2]*Department of Polymer Science and Engineering, University of Massachusetts, Amherst, Massachusetts 01003, USA*

(Received 24 April 2019; published 9 July 2019)

Scanning tunneling spectroscopy requires the application of a potential difference between the sample and a tip. In metal-vacuum-metal junctions, one can safely assume that the potential is constant along the metallic substrate. Here, we show that the inhomogeneous shape of the electric potential has to be taken into account when probing spatially extended molecules on a decoupling layer. To this end, oligothiophene-based molecules were deposited on a monolayer of molybdenum disulfide (MoS_2) on a Au(111) surface. By probing the delocalized molecular orbital along the thiophene backbone, we found an apparent intramolecular shift of the positive ion resonance, which can be ascribed to a perturbation potential caused by the tip. Using a simple model for the electrostatic landscape, we show that such a perturbation is caused by the inhomogeneity of the applied bias potential in the junction and may be further modified by an electric dipole of a functionalized tip. The two effects can be disentangled in tunneling spectra by probing the apparent energy shift of vibronic resonances along the molecular backbone. We suggest that extended molecules on MoS_2 can be used as a sensor for the shape of the electrostatic potential of arbitrary tips.

DOI: 10.1103/PhysRevB.100.035410

I. INTRODUCTION

Scanning tunneling microscopy (STM) is frequently employed for the determination of energy levels of individual molecules on surfaces. Because STM relies on conducting surfaces, metals are the most frequent choice as a substrate for the molecules. However, the molecular states are strongly modified by hybridization and screening from the metal substrate. To preserve the character of isolated molecules, thin decoupling layers are inserted between the molecule and the metal. Prominent examples are thin layers of ionic materials, such as NaCl [1–4] or Al_2O_3 [5,6]. Alternatively, monolayers of molecules [7,8], h-BN [9–11], or graphene [12–14] have been employed.

The incorporation of thin insulating layers implies a second tunneling barrier between an adsorbate and the metal substrate, such that the molecular states are no longer pinned to the Fermi level of the substrate. Because of the second tunneling barrier, the molecules do not lie on the same potential as the metallic substrate. The finite voltage drop across the decoupling layer requires a larger absolute bias voltage for probing the molecular energy levels than without decoupling interlayer [5,15]. As the fraction of the potential drop across the layer is tunable by the tip–sample distance, it has been suggested to utilize this effect as a gating potential, enabling controlled charging of single molecules [15–17] or buried impurities [18]. Such a gating effect of the tip is also important on semiconducting substrates as band bending shifts all states, causing new quantum well states [19–21].

Furthermore, it has been shown that the gating potential does not only depend on the vertical tip–sample distance, but also on the lateral distance from the molecule/impurity [15–18]. The qualitative distance dependence of the charging peaks could be understood with a pointlike tip model with the distance scaling according to simple geometrical considerations. Hence, the spatial distribution of the potential within both tunneling barriers could be neglected. We note that the peaks signaling the charging event were of several tens of millielectronvolt (meV) width.

Recently, a single layer of MoS_2 has been suggested as a decoupling layer, where tunneling through electronic states of molecules revealed sharp resonances of only a few (meV) width [22]. In this work, we show that the molecular resonances exhibit an apparent shift along the molecular backbone by some tens of meV. At first sight, this is in disagreement with the resonances originating from the same molecular orbital. However, we explain that this apparent shift occurs as a result of the inhomogeneous potential in the molecular plane. Hence, we suggest that these narrow resonances are an ideal sensor for mapping the shape of the potential at the position of the molecule within the junction. To benchmark the sensor, we functionalize the STM tip with a Cl atom yielding an additional dipolar potential.

As a model system we use 2,5-bis(3-dodecylthiophen-2-yl)thieno[3,2-b]thiophene (BTTT) molecules [23] adsorbed on a monolayer of MoS_2 on Au(111). The molecule consists of a thiophene and thienothiophene based backbone with two $C_{12}H_{25}$ chains attached to the two terminal thiophene groups [see Fig. 1(b)].

II. METHODS

A monolayer of MoS_2 was grown on a clean Au(111) surface by deposition of Mo and subsequent heating in an H_2S atmosphere [25,26]. BTTT molecules were evaporated

*c.lotze@fu-berlin.de

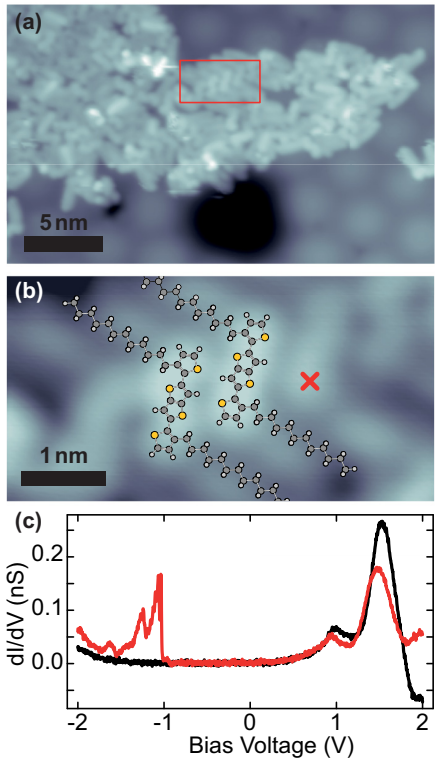

FIG. 1. (a) Island of BTTT on MoS_2/Au(111). The dark area in the bottom is due to a vacancy island in the underlying Au(111) surface [24](1 V/20 pA). (b) Zoom into ordered one-dimensional phase with overlayed stick-and-ball models of BTTT molecules (1 V/20 pA). The red cross marks the tip position of the dI/dV spectrum taken on BTTT. (c) dI/dV spectrum of MoS_2 (black) and BTTT (red): The PIR and the onset of the NIR of BTTT can be observed at -1 V and 2 V, respectively [22]. (Feedback opened at 2 V/100 pA; $V_{rms} = 5$ mV)

from a Knudsen cell evaporator (365 K) onto the sample held at 200 K. All STM measurements were carried out at 4.6 K. Differential conductance spectra were recorded using a standard lock-in technique (modulation frequency of $f = 921$ Hz). A metallic gold tip was prepared by controlled indentation of a tungsten tip into the clean Au(111) substrate. Its quality was regularly assured by reference spectra on Au(111) and MoS_2. For a single BTTT molecule in gas phase, we performed DFT calculations, using the GAUSSIAN09 package with the B3PW91 functional and the 6-31g(d,p) basis set [27].

III. RESULTS AND DISCUSSION

A. Adsorption structure and electronic resonances of BTTT on MoS_2

When evaporated onto a MoS_2/Au(111) sample held at 200 K the majority of the BTTT molecules form large islands on the Au(111) surface. A smaller fraction of the molecules forms partially ordered islands on the MoS_2 as shown in Fig. 1(a). The most common structure in the short-ranged order is a quasi-one-dimensional arrangement, where the BTTT molecules are lying with their thiophene backbone and alkyl chains parallel next to each other [Fig. 1(b)].

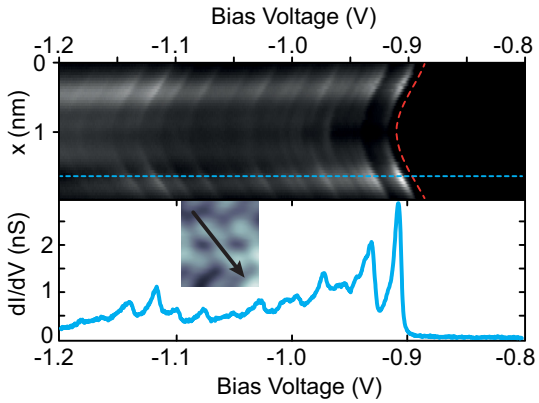

FIG. 2. Line of 50 dI/dV spectra along the thiophene backbone of BTTT (see inset), displaying the PIR and its vibronic satellites. The red dashed line highlights the shift of the elastic and inelastic peaks to larger negative bias voltages at the center of the molecule. A single spectrum taken at the end of the molecule (marked by blue dashed line) is displayed in the bottom panel. (Feedback opened at the end of the thiophene backbone: -1.2 V/300 pA; $V_{rms} = 0.5$ mV)

To investigate the electronic properties of BTTT on MoS_2 we performed constant-height tunneling spectroscopy [see Fig. 1(c)]. The reference spectrum on MoS_2 shows the typical conduction band states at 0.9 V and 1.4 V, as well as the onset of the valence band at -2 V [26]. The spectrum taken on a BTTT molecule shows a narrow positive ion resonance (PIR) at -1 V, which can be ascribed to tunneling through the highest occupied molecular orbital (HOMO). The negative ion resonance (NIR) reflecting tunneling through the lowest unoccupied molecular orbital (LUMO) lies outside of the MoS_2 gap (>2 V) [22]. Because the PIR is located inside the electronic gap of MoS_2, it is electronically decoupled from the environment and exhibits a very narrow line width of 6 meV. The narrow line width allows for the observation of vibronic satellite peaks at larger negative bias voltages. These were analyzed in more detail in a previous work [22].

To probe the effect of the tip's location on the measured electronic resonances, we plot a set of 50 spectra taken along the BTTT backbone in Fig. 2. The onset of tunneling through the HOMO is shifted by ~25 mV to larger negative bias voltages in the center of the molecule than at its terminations (see red dashed line as guide to the eye). The set of vibronic peaks follows the same trend. We note that the strongest dI/dV signal is observed at the terminations of the thiophene unit with less signal in the center, even though the HOMO is delocalized along the thiophene backbone. This intensity distribution can be simulated employing an *s*-wave tip and calculating the tunneling matrix element using Bardeen's approach [28] at a certain height above the molecule (see Appendix A).

B. Spatial variation of molecular resonances due to an inhomogeneous tip–substrate potential

To understand the apparent intramolecular shift of the PIR, we have to take the shape of the electric potential in the STM

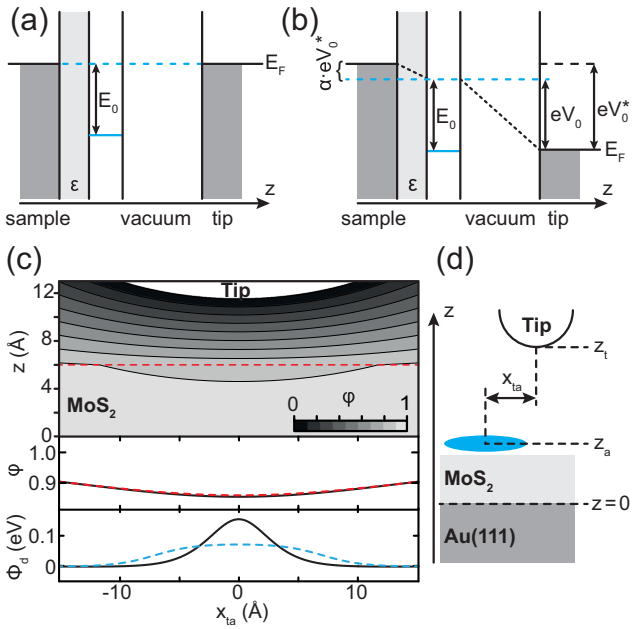

FIG. 3. [(a) and (b)] Plate capacitor model of the tunneling junction without (a) and with (b) applied bias voltage. The solid blue line represents the electronic state of an adsorbate. (c) (Top) Simple two charge model of $\varphi(x, z)$ in the tunnel junction (see Appendix), with tip radius $R = 20$ Å, and tip–sample distance $z_t = 6.5$ Å. The effect of the dielectric constant of MoS_2 was approximated by stretching the vertical axis within the MoS_2 layer (below the dashed red line) by a factor of 6. (Middle) Shape of $\varphi(x_{ta}, z_a)$ (black solid) above the MoS_2 layer (along the dashed line in top panel) as well as effective bias potential $\langle\phi_b(x_{ta}, z_a)\rangle$ obtained by perturbation theory (dashed red line). (Bottom) Electric potential $\phi_d(x_{ta}, z_a)$ (black) due to a dipole located at the tip with positive charge pointing towards the surface ($p = -3$ D) and distance $d = 3$ Å between the charges. The effective dipole potential $\langle\phi_d(x_{ta}, z_a)\rangle$ from perturbation theory is plotted by the dashed blue line. (d) Sketch of the junction and the used labels.

junction into account. Because the decoupling layer acts as an insulator, the junction can be described as a double tunneling barrier. We consider an electronic state of an adsorbate between these barriers with an energy of E_0 with respect to the aligned Fermi levels of the two leads [Fig. 3(a)]. When a bias voltage V_b is applied between surface and tip, it drops over both barriers as depicted in Fig. 3(b). Hence the effective bias voltage, applied to the adsorbate, is reduced by a factor of $\alpha \leqslant 1$. In order to measure the adsorbate's state, the voltage drop across the decoupling layer needs to be compensated and the bias voltage has to be increased to $V > E_0/e$. In fact, the adsorbate state appears in a dI/dV spectrum at a bias voltage of [5,15]

$$V_0^* = \frac{E_0}{e(1-\alpha)} = \frac{V_0}{1-\alpha}. \tag{1}$$

In the often used model of a plate capacitor for the tunneling junction, the potential is constant within a plane parallel to the substrate. The factor α is therefore independent of the lateral distance between tip and adsorbate. For a more realistic tip model, however, the electrostatic potential at a certain point in the junction depends not only on the vertical but also on the lateral distance to the tip. A position-independent factor α is no longer sufficient to account for the voltage drop across the decoupling layer.

In first order, the inhomogeneous electric potential in the junction scales with the applied bias voltage and depends on the position. It can be described by $\phi_b(\vec{r}) = V_b\,\varphi(\vec{r})$, with $\varphi(\vec{r})$ being the potential shape of dimension unity and V_b the applied bias voltage. As the tip is grounded, the potential vanishes there [$\phi_b(\text{tip}) = 0$], whereas at the metal surface it is equal to the bias voltage [$\phi_b(\text{metal substrate}) = V_b$]. The voltage between an adsorbate at position $\vec{r}_a$ and the tip is then $V_b\,\varphi(\vec{r}_a)$. Accordingly, the voltage drop across the decoupling layer is $V_b\,(1 - \varphi(\vec{r}_a)) = V_b\,\alpha(\vec{r}_a)$. Here, we approximate a vanishing contact potential difference (CPD), which would introduce a bias offset [29] (see Appendix E).

Due to the position-dependent voltage drop, the energy level of the adsorbate can be tuned with respect to the sample, which has been employed for an effective gating of the adsorbate state [15,16,18]. It depends on the distance of the tip from the molecule, both in the lateral as well as vertical direction. As a result charging rings appear when the adsorbate's state crosses the Fermi level of the substrate.

In the following, we explain that the shape $\varphi(\vec{r})$ of the potential in the tunneling barrier is responsible for the aforementioned apparent shift of the molecular resonance across the molecule. For this we use a simple model to describe $\varphi(\vec{r})$ between tip apex and sample. The tip is approximated by a point charge and the constant electric potential of the sample surface is ensured by a mirror charge of opposite sign in the metal substrate. A more detailed description of the model is given in the Appendix. The resulting $\varphi(x, z)$ is represented by several contour lines in the top panel of Fig. 3(c). In accordance with our experimental setup the tip is grounded [$\varphi(\text{tip}) = 0$] and the bias voltage (here normalized to 1) is applied to the surface [$\varphi(x, 0) = 1$].

The resulting potential shape at the height z_a of an adsorbate on the decoupling layer $\varphi(x_{ta}, z_a)$ is shown in the mid panel of Fig. 3(c) (solid black line) with x_{ta} being the lateral distance between tip and adsorbate. In order to account for the dielectric constant ϵ_{lay} of the MoS_2 layer, we approximated $z_a = d_{lay}/\epsilon_{lay} = 6.1$ Å$/6.4 \sim 1$ Å, with d_{lay} being the thickness of a MoS_2 monolayer [30]. Because of the curvature of the tip apex, $\varphi(x_{ta}, z_a)$ is minimal when the tip is placed right above the adsorbate ($x_{ta} = 0$).

To analyze the effect of the inhomogeneous potential on molecular states of an adsorbate, we employ a simple perturbation model (for details see Appendix). We represent the molecular orbital of the BTTT by the seventh mode of a particle in a one-dimensional box (PiB) of length 14 Å. The perturbation potential within the box is given by the inhomogeneous potential along the molecule as determined in Fig. 3(c) (solid black line). The effective potential shape $\langle\varphi(x_{ta})\rangle$ of the PiB was calculated in first order perturbation theory and displayed in Fig. 3(c) (dashed red line). In this simple model, the effective potential can be roughly approximated as an average of the bias potential along the molecule. Since $\langle\varphi(x_{ta})\rangle$ depends on the tip position, the required bias voltage

to measure a delocalized state [$V_0^* = E_0/e\langle\varphi(x_{\mathrm{ta}})\rangle$] depends on x_{ta}. Hence, the molecular energy levels appear to lie at different energies along the molecule, with the shift being strongest in the order of a few percent when the tip is located at the center of the molecule. This is in agreement with our experimental observation of a larger negative bias voltage being required for probing the PIR in the molecule's center (Fig. 2).

C. Inhomogeneous potential due to a tip dipole

In addition to the inherent inhomogeneous potential in the tip–substrate junction, the tip may carry a local dipole moment at its apex. STM tips are known to provide a dipole moment of up to a few Debye [31,32], depending on their termination. Hence, the applied potential to an adsorbate on a decoupling layer would be a superposition of the potential set by the applied bias voltage ϕ_b and the dipole potential ϕ_d. The effect of an additional potential in a tunneling junction has been utilized in a slightly different configuration for scanning quantum dot microscopy [33]. Considering the effect of the dipole in a similar perturbation model as above leads to a shift of the electronic energy levels in the dI/dV spectrum to $V_0^* = E_0/e - \phi_d$ (now neglecting the effect of the inhomogeneity of the applied bias voltage). For a metal tip, the dipole usually points with the positive charge towards the sample, i.e., $\phi_d > 0$ within the junction, thus requiring a larger negative bias voltage for measuring an electronic state in the dI/dV spectrum. The effective potential of a tip dipole also depends strongly on the lateral distance between tip and adsorbate, as shown in the bottom panel of Fig. 3(c) (solid black). Employing an equivalent perturbation model as above for the effect of a dipole potential (see Appendix) on a PiB state we obtain the effective potential $\langle\phi_d(x_{\mathrm{ta}})\rangle$, shown as the dashed blue line across the molecule. For the measurement of the PIR of BTTT with a metal tip, this would also cause an apparent shift of the state to more negative bias voltages in the center of the molecule. Hence, a dipole of a metal tip qualitatively shifts the states in the same direction as the inhomogeneity of the potential in the tip–sample junction itself.

D. Comparison of metal and Cl tip

To illustrate the shift originating from the inhomogeneity of the junction and a possible tip dipole, we impose a tip dipole in the opposite direction on the tip. To this end, we pick up a Cl atom from co-deposited Fe-octaethyl-chloride molecules. The Cl is expected to be negatively charged at the tip apex, and, thus, exhibit a dipole oriented away from the substrate [31]. To exclude any effects of the molecular environment, we first probe the shift of the PIR along a BTTT molecule as shown in Fig. 4(a). Afterward, we measure on the very same molecule again with a Cl functionalized tip. Now, we observe an inverted trend of the shift of all resonances along the molecule. A smaller negative bias voltage is required for PIR excitation in the center of the molecule than at its terminations. (The asymmetric intensity in the map is probably due to interaction with the neighboring molecule.) The inversion of the trend directly reflects that the dipole plays a significant role. At first sight, it may be surprising that the shift with both tips—though of opposite direction—

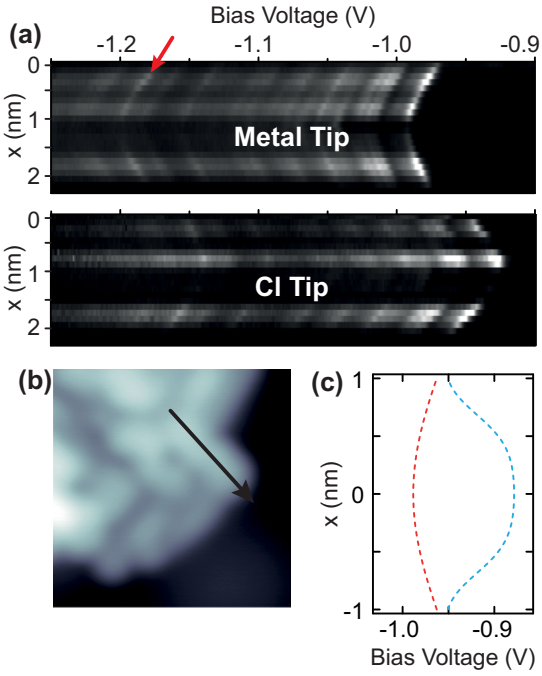

FIG. 4. (a) Line of 22 dI/dV spectra along a BTTT molecule [marked in (b)] measured with a metal (top) and a Cl functionalized (bottom) tip. While the peaks for the metal tip shift to more negative bias voltages, the Cl tip causes a shift to more positive bias voltages in the center of the molecule. The red arrow marks the vibronic state of the C–C stretching mode. (Feedback opened at the end of the thiophene backbone: −1.3 V/150 pA; $V_{\mathrm{rms}} = 1$ mV) (b) Topography of BTTT molecule, with line of spectra marked by black arrow (1 V/20 pA). (c) Simulated shift of an electronic state with energy −0.85 eV in a dI/dV spectrum due to a decoupling layer without (red) and with tip dipole of $p = 3$ D (blue).

is of approximately the same size. The dipole of the metal tip is expected to be much smaller than of the Cl tip [31]. However, the effect of the inhomogeneous junction geometry and a metal dipole add up, whereas the dipole of the Cl tip overcompensates the potential shift due to the junction geometry.

Adding up the effect of an inhomogeneous junction and of a tip dipole, the effective electric potential applied to the adsorbate is

$$\langle\phi_{\mathrm{a}}(x_{\mathrm{ta}})\rangle = V_b\,\langle\varphi(x_{\mathrm{ta}})\rangle + \langle\phi_d(x_{\mathrm{ta}})\rangle. \tag{2}$$

It consist of the bias-voltage-dependent term due to the position-dependent voltage drop, as well as a bias-voltage-independent term from the dipole potential. In accordance, an electronic state with energy E_0 is observed in the dI/dV spectrum at a bias voltage of

$$V_0^*(x_{\mathrm{ta}}) = \frac{E_0/e - \langle\phi_d(x_{\mathrm{ta}})\rangle}{\langle\varphi(x_{\mathrm{ta}})\rangle}. \tag{3}$$

Figure 4(c) displays the calculated $V_0^*(x_{\mathrm{ta}})$ of a decoupled state at $E_0 = -0.85$ eV for a tip without dipole moment (red) and with dipole moment of $p = 3$ D (blue). With these parameters we can reproduce the observed behavior of the measured data displayed in Fig. 4(a) with our simple model.

In order to disentangle the two origins for both metal and Cl functionalized tip, we utilize the shift of the vibronic resonances as compared to the elastic resonance. As example, we choose the vibronic resonance associated to the C–C stretching mode at about $\Delta V^* = 210$ mV [marked by red arrow in Fig. 4(a)].

The voltage difference $\Delta V^*(x_{\mathrm{ta}})$ between the elastic and the inelastic peak is accordingly

$$\Delta V^*(x_{\mathrm{ta}}) = |V^*_{\mathrm{inel.}} - V^*_{\mathrm{ela.}}| = \frac{\hbar\omega}{e\langle\varphi(x_{\mathrm{ta}})\rangle}, \tag{4}$$

with $\hbar\omega$ being the energy of the vibrational mode. Please note that ΔV^* depends solely on the spatially varying bias potential shape $\langle\varphi(x_{\mathrm{ta}})\rangle$ and not on the potential of the tip dipole. In Fig. 5(a), the calculated elastic (black) and the inelastic peaks are plotted along the molecule for a tip without (red) and with dipole (blue). The energy scale is shifted by $V_{\mathrm{ela.}}(x_{\mathrm{ta}})$, thus the elastic peak is always at 0 V. As a vibrational energy we use $\hbar\omega = 180$ meV to account for the 10%–15% voltage drop in our model and to reproduce the experimental values. The voltage difference $\Delta V^*(x_{\mathrm{ta}})$ is largest in the center of the molecule, where $\langle\varphi(x_{\mathrm{ta}})\rangle$ has a minimum. Since the dipole potential is canceled out by the subtraction, the inelastic peaks shift independently of the tip dipole.

In contrast, by normalizing the bias voltages with $V^*_{\mathrm{ela.}}(x_{\mathrm{ta}})$, the term $\langle\varphi(x_{\mathrm{ta}}\rangle)$ cancels out and we obtain the normalized voltage

$$v(x_{\mathrm{ta}}) = \frac{V^*_{\mathrm{inel.}}}{V^*_{\mathrm{ela.}}} = 1 + \left|\frac{\hbar\omega}{E_{\mathrm{ela.}} - \langle\phi_d(x_{\mathrm{ta}})\rangle}\right| \tag{5}$$

In the case of no tip dipole, $\langle\phi_d(x_{\mathrm{ta}})\rangle$ vanishes and v is independent of the position of the tip. Hence, a vibronic state is expected to appear at a constant normalized voltage as displayed by the red dashed line in Fig. 5(f). For a tip including a dipole moment, the normalized energy of the vibronic state changes in dependence of the tip position. When measuring a PIR ($E_{\mathrm{ela.}} < 0$) with a Cl functionalized tip [$\phi_d(x_{\mathrm{ta}}) < 0$] the normalized voltage of the vibronic state should shift to a higher normalized voltage at the center of the molecule [blue dashed line in Fig. 5(f)].

The dI/dV spectra measured with both tips along the BTTT are displayed in Fig. 5 with shifted [(b) and (c)] and normalized [(d) and (e)] voltage axis. The vibronic states of the C–C stretch mode are marked by the dashed white lines as a guide for the eye. In the case of a shifted voltage axis, both tips feature a similar shift of the vibronic state to more negative energies by a few percent, i.e., larger voltage difference between elastic and inelastic peak. In accordance with the calculation, this confirms the effect of the geometry-imposed inhomogeneous potential for both tips. Please note that the exact height for both tips are unknown, thus the experimental data can only be compared qualitatively between the two tips and the simulation.

For the normalized voltage axis the two tips behave differently. For the metal tip, the vibronic state is at nearly constant normalized voltage along the molecule, independent of the tip position. This implies a negligible dipole moment of the metal tip, when a vanishing CPD is assumed (see Appendix E).

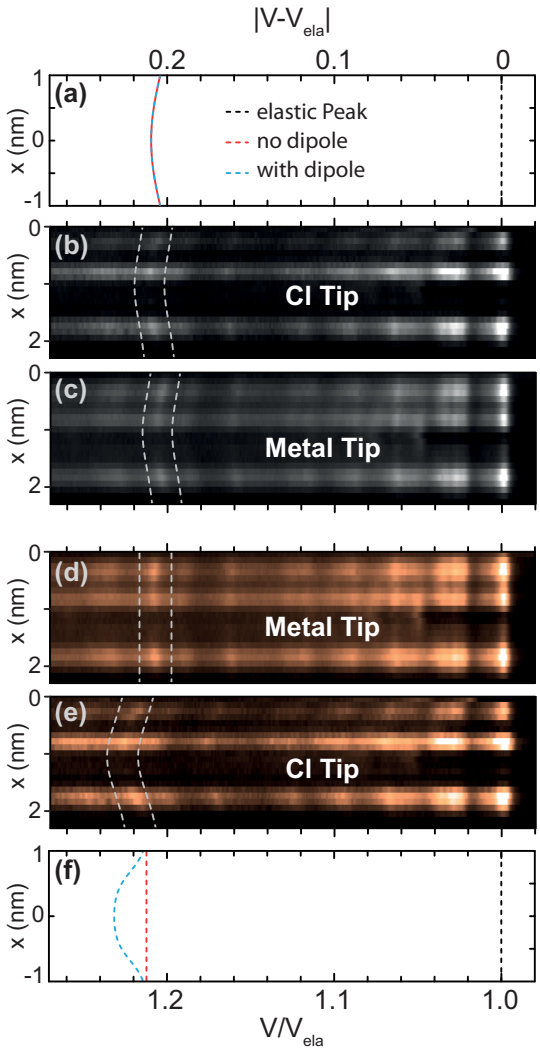

FIG. 5. (a) Calculated shifted bias voltage of elastic (black) and vibronic peak along a molecule for a tip with (blue) and without (red) tip dipole. The effect of the constant dipole potential cancels out, yielding an identical shift for both tips. [(b) and (c)] Measured dI/dV spectra with shifted bias voltage axis for Cl and metal tip, with white dotted lines as a guide for the eye. Both tips show a similar shift of the inelastic peak, indicating a similar effect due to the inhomogeneous bias potential. [(d) and (e)] dI/dV spectra with normalized bias-voltage axis for metal and Cl tip. For the metal tip, the inelastic peak is nearly constant, pointing towards a negligible tip dipole moment. (f) Calculated normalized bias voltage of elastic (black) and vibronic peak for a tip with (blue) and without (red) tip dipole.

Accordingly the energy shift along the molecule measured by a metal tip is almost exclusively due to the inhomogeneous potential within the junction. For the Cl tip, the vibronic state shifts strongly to higher normalized voltages as predicted and plotted in Fig. 5(f) for a nonzero dipole moment.

IV. CONCLUSION

In conclusion, we presented the perturbation effect of an inhomogeneous electric potential in the STM junction on a

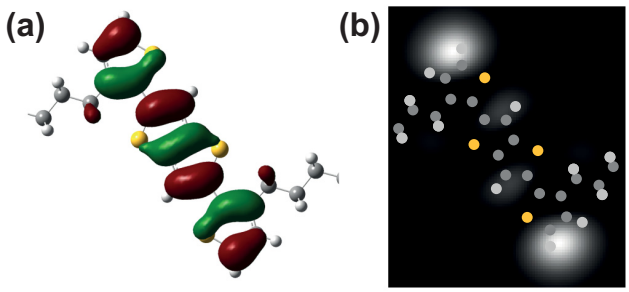

FIG. 6. (a) Highest occupied molecular orbital of the BTTT molecule. (b) Calculated constant-height image of the HOMO, measured with an *s*-wave tip.

delocalized molecular orbital. Utilizing the excellent decoupling properties of single-layer MoS_2, we demonstrated that this effect causes an apparent intramolecular shift of the PIR of the thiophene based BTTT molecule. The inhomogeneous potential in the junction does not only originate from the applied bias voltage, but also from a tip dipole of a functionalized tip. Using the vibronic resonances in the tunneling spectra we were able to distinguish between the two origins. This observation is important to take into account, because it is relevant for all adsorbates with delocalized electronic states on a decoupling layer. In turn, we suggest to use the resonances' shift as a sensor for inhomogeneous potentials and dipole components in the tip.

ACKNOWLEDGMENTS

We are grateful to the Deutsche Forschungsgemeinschaft for funding within the framework of the SFB 658 and TRR 227.

APPENDIX A: TUNNELING PROBABILITY INTO PIR

The BTTT molecule was calculated in gas phase, using the GAUSSIAN09 package with the B3PW91 functional and the 6-31g(d,p) basis set [27]. The constant-height dI/dV image [Fig. 6(b)] was then simulated by calculating the tunneling matrix element at each point of the flat-lying molecule [28]

$$M_{\mathrm{ta}} \propto \int d\mathbf{S}(\Psi_{\mathrm{t}}^{*}\nabla\Psi_{\mathrm{a}} - \Psi_{\mathrm{a}}\nabla\Psi_{\mathrm{a}}^{*}). \tag{A1}$$

Here, Ψ_a is the wave function of the molecule obtained by DFT calculations [Fig. 6(a)] and Ψ_t the spherical wave function of an *s*-wave tip. We choose our integration plane at 1.5 Å above the center of the molecule. The calculations reveal the largest tunneling probability at the terminations of the thiophene backbone. The images resemble the experimental data at negative bias voltage, thus evidencing tunneling via the HOMO.

APPENDIX B: JUNCTION MODEL

We model the STM junction as an almost spherical, grounded tip with radius R and distance z_t to a conducting surface, held at bias voltage V_b, as shown in Fig. 7(a). The potential within this junction can be approximated by a point charge q and its mirror charge $-q$ separated by $2(R + z_t)$ at $x = 0$ [Fig. 7(b)]. The resulting potential reads

$$\phi_b(x,z) = \frac{1}{4\pi\epsilon_0}\left[\frac{q}{\sqrt{x^2+(z-R-z_t)^2}} - \frac{q}{\sqrt{x^2+(z+R+z_t)^2}}\right] + C. \tag{B1}$$

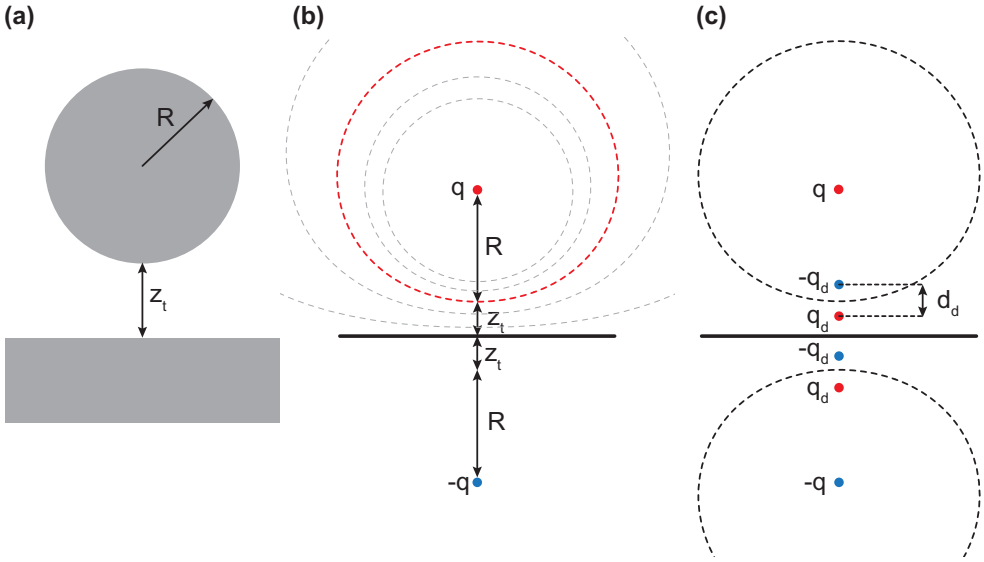

FIG. 7. Tip models: (a) spherical tip at distance z_t to the substrate. (b) Approximating the electric potential by two charges. The dashed lines represent isopotential surfaces of the dipole. The isopotential surface at distance R between charge and surface (red) is chosen as a model for the metal tip. (c) Approximating the tip dipole with two charges q_d and their mirror charges.

We choose the constant potential C in a way, that $\phi_b(0, z_t) = 0$, yielding

$$\phi_b(x,z) = \frac{q}{4\pi\epsilon_0}\left[\frac{1}{\sqrt{x^2+(z-R-z_t)^2}} - \frac{1}{\sqrt{x^2+(z+R+z_t)^2}} - \frac{1}{|R|} + \frac{1}{|R+2z_t|}\right]. \tag{B2}$$

Thus the isopotential surface around the charge q approximates the grounded tip with radius R [dashed red line in Fig. 7(b)].

The charge q is chosen to cause a certain bias voltage V_b applied to the sample [$\phi_b(x, 0) = V_b$]:

$$q = -4\pi\epsilon_0\left(\frac{R^2}{2z_t} + R\right)V_b \tag{B3}$$

Furthermore we can write the potential between surface and tip as

$$\phi_b(x,z) = V_b\,\varphi(x,z). \tag{B4}$$

Inserting Eqs. (B2) and (B3) yields

$$\varphi(x,z) = 1 - \left(\frac{R^2}{2z_t} + R\right)\left[\frac{1}{\sqrt{x^2+(z-R-z_t)^2}} - \frac{1}{\sqrt{x^2+(z+R+z_t)^2}}\right]. \tag{B5}$$

A map of $\varphi(x, z)$ is displayed in Fig. 3 of the main text, for $R = 20$ Å and $z_t = 6.5$ Å.

To account for the decoupling layer, we assume the molecule to be at $z_a = 1$ Å above the substrate.

APPENDIX C: DIPOLE MODEL

We approximate the tip dipole with two mirror charges centered to the tip apex as depicted in Fig. 7(c). For a tip with a dipole p and length d, the potential is

$$\phi_d(x,z) = \frac{p/d}{4\pi\epsilon_0}\left[\frac{1}{\sqrt{x^2+(z-z_t+d/2)^2}} - \frac{1}{\sqrt{x^2+(z-z_t-d/2)^2}} - \frac{1}{\sqrt{x^2+(z+z_t-d/2)^2}} + \frac{1}{\sqrt{x^2+(z+z_t+d/2)^2}}\right]. \tag{C1}$$

The potential at $z_a = 1$ Å is displayed in Fig. 3 of the main text, for $p = -3$ D and $d = 3$ Å.

APPENDIX D: PERTURBATION MODEL

In order to investigate the influence of an inhomogeneous potential to the energy of a molecular state, we use a simple perturbation model. The molecular orbital is represented by a particle in a one-dimensional box of length L. We choose the seventh mode, to emulate the six nodal planes of the HOMO of the BTTT molecule. Hence, the wave function is described by

$$\Psi(x) = \begin{cases} 0 & x < -\frac{L}{2} \\ \sqrt{\frac{2}{L}}\sin\frac{7\pi}{L}\left(x+\frac{L}{2}\right) & -\frac{L}{2} < x < \frac{L}{2} \\ 0 & x > -\frac{L}{2} \end{cases}$$

as depicted in Fig. 8.

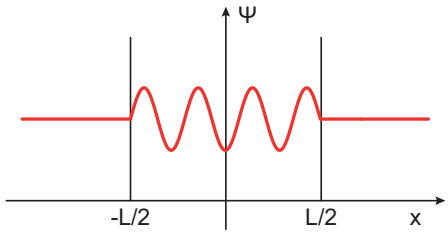

FIG. 8. Wave function of the seventh mode of a particle in a one-dimensional potential well with infinite walls.

The energy of the molecular state within a potential is then shifted by

$$E(x_{ta}) = e\int_{-\infty}^{+\infty}\Psi^*(x)\phi_0(x-x_{ta})\Psi(x)\,dx, \tag{D1}$$

whereas e is the elementary charge and x_{ta} the lateral position of the tip relative to the molecule.

For the inhomogeneous potential in the molecular plane, we use

$$\phi_0(x) = \phi_b(x) + \phi_d(x) \tag{D2}$$

$$= V_b\,\varphi(x) + \phi_d(x), \tag{D3}$$

with $\phi_b(x)$ and $\phi_d(x)$ being the bias and the dipole potential, respectively, at height z_a as described above.

Hence, the shift due to the perturbation is

$$E(x_{ta}) = eV_b\int_{-\infty}^{+\infty}\Psi^*(x)\varphi(x-x_{ta})\Psi(x)\,dx + e\int_{-\infty}^{+\infty}\Psi^*(x)\phi_d(x-x_{ta})\Psi(x)\,dx = eV_b\langle\varphi(x_{ta})\rangle + e\langle\phi_d(x_{ta})\rangle.$$

In the main text, $\langle\varphi(x_{ta})\rangle$ and $\langle\phi_d(x_{ta})\rangle$ are displayed in Fig. 3, for $L = 14$ Å, which corresponds to the length of the thiophene backbone of the BTTT molecule.

An electronic state at energy E_0 [see Fig. 3(a) in the main text] appears, thus, in a tunneling spectrum at bias voltage:

$$V_0^*(x_{ta}) = \frac{E_0/e - \langle\phi_d(x_{ta})\rangle}{\langle\varphi(x_{ta})\rangle} \tag{D4}$$

APPENDIX E: EFFECT OF CPD

In the main text, we approximated the contact potential difference (CPD) with $V_{CPD} = 0$. In this section the effect of a nonvanishing CPD in the junction is discussed. In good

approximation, we can assume the total potential to depend linearly on the CPD [29,34]:

$$\phi_{\text{tot}} = \varphi(\vec{r})\,(V_{\text{b}} + V_{\text{CPD}}). \tag{E1}$$

In case of an additional dipole at the tip, we have to expand the equation to

$$\phi_{\text{tot}}(\vec{r}) = \varphi(\vec{r})\,V_{\text{b}} + \varphi(\vec{r})\,V_{\text{CPD}} + \phi_d(\vec{r}). \tag{E2}$$

As can be seen, the bias-voltage-depended term is not affected by the CPD. The bias-voltage-independent part ϕ_{static} on the other hand, now consists of both the dipole potential, as well as the CPD:

$$\phi_{\text{static}}(\vec{r}) = \varphi(\vec{r})\,V_{\text{CPD}} + \phi_d(\vec{r}). \tag{E3}$$

Hence, the effect of a nonvanishing CPD can be viewed as a modification of the dipole term in our simple model. The observation in Sec. III D—no effective dipole on the metal tip—then implies that the CPD and the possible dipole field roughly cancel each other.

[1] J. Repp, G. Meyer, S. M. Stojković, A. Gourdon, and C. Joachim, Phys. Rev. Lett. **94**, 026803 (2005).

[2] L. Gross, N. Moll, F. Mohn, A. Curioni, G. Meyer, F. Hanke, and M. Persson, Phys. Rev. Lett. **107**, 086101 (2011).

[3] C. J. Villagomez, T. Zambelli, S. Gauthier, A. Gourdon, S. Stojkovic, and C. Joachim, Surf. Sci. **603**, 1526 (2009).

[4] C. Bombis, F. Ample, L. Lafferentz, H. Yu, S. Hecht, C. Joachim, and L. Grill, Angew. Chem. Int. Ed. **48**, 9966 (2009).

[5] X. H. Qiu, G. V. Nazin, and W. Ho, Phys. Rev. Lett. **92**, 206102 (2004).

[6] S. Li, D. Yuan, A. Yu, G. Czap, R. Wu, and W. Ho, Phys. Rev. Lett. **114**, 206101 (2015).

[7] K. J. Franke, G. Schulze, N. Henningsen, I. Fernández-Torrente, J. I. Pascual, S. Zarwell, K. Rück-Braun, M. Cobian, and N. Lorente, Phys. Rev. Lett. **100**, 036807 (2008).

[8] F. Matino, G. Schull, F. Köhler, S. Gabutti, M. Mayor, and R. Berndt, Proc. Natl. Acad. Sci. USA **108**, 961 (2011).

[9] P. Järvinen, S. Hämäläinen, K. Banerjee, P. Häkkinen, M. Ijäs, A. Harju, and P. Liljeroth, Nano Lett. **13**, 3199 (2013).

[10] S. Joshi, F. Bischoff, R. Koitz, D. Ecija, K. Seufert, A. P. Seitsonen, J. Hutter, K. Diller, J. I. Urgel, H. Sachdev, J. V. Barth, and W. Auwärter, ACS Nano **8**, 430 (2013).

[11] F. Schulz, R. Drost, S. Hämäläinen, and P. Liljeroth, ACS Nano **7**, 11121 (2013).

[12] J. Cho, J. Smerdon, L. Gao, Ö. Süzer, J. R. Guest, and N. P. Guisinger, Nano Lett. **12**, 3018 (2012).

[13] A. Riss, S. Wickenburg, L. Z. Tan, H.-Z. Tsai, Y. Kim, J. Lu, A. J. Bradley, M. M. Ugeda, K. L. Meaker, K. Watanabe, T. Taniguchi, A. Zettl, F. R. Fischer, S. G. Louie, and M. F. Crommie, ACS Nano **8**, 5395 (2014).

[14] S. Wickenburg, J. Lu, J. Lischner, H.-Z. Tsai, A. A. Omrani, A. Riss, C. Karrasch, A. Bradley, H. S. Jung, R. Khajeh, D. Wong, K. Watanabe, T. Taniguchi, A. Zettl, A. H. C. Neto, S. G. Louie, and M. F. Crommie, Nat. Commun. **7**, 13553 (2016).

[15] G. V. Nazin, S. W. Wu, and W. Ho, Proc. Natl. Acad. Sci. USA **102**, 8832 (2005).

[16] I. Fernández-Torrente, D. Kreikemeyer-Lorenzo, A. Stróżecka, K. J. Franke, and J. I. Pascual, Phys. Rev. Lett. **108**, 036801 (2012).

[17] N. Hauptmann, C. Hamann, H. Tang, and R. Berndt, Phys. Chem. Chem. Phys. **15**, 10326 (2013).

[18] K. Teichmann, M. Wenderoth, S. Loth, R. G. Ulbrich, J. K. Garleff, A. P. Wijnheijmer, and P. M. Koenraad, Phys. Rev. Lett. **101**, 076103 (2008).

[19] R. Dombrowski, C. Steinebach, C. Wittneven, M. Morgenstern, and R. Wiesendanger, Phys. Rev. B **59**, 8043 (1999).

[20] R. M. Feenstra, Surf. Sci. **603**, 2841 (2009).

[21] Y. Jiang, J. Mao, D. Moldovan, M. R. Masir, G. Li, K. Watanabe, T. Taniguchi, F. M. Peeters, and E. Y. Andrei, Nat. Nanotechnol. **12**, 1045 (2017).

[22] N. Krane, C. Lotze, G. Reecht, L. Zhang, A. L. Briseno, and K. J. Franke, ACS Nano **12**, 11698 (2018).

[23] L. Zhang, F. Liu, Y. Diao, H. S. Marsh, N. S. Colella, A. Jayaraman, T. P. Russell, S. C. Mannsfeld, and A. L. Briseno, J. Am. Chem. Soc. **136**, 18120 (2014).

[24] N. Krane, C. Lotze, J. M. Läger, G. Reecht, and K. J. Franke, Nano Lett. **16**, 5163 (2016).

[25] S. G. Sørensen, H. G. Füchtbauer, A. K. Tuxen, A. S. Walton, and J. V. Lauritsen, ACS Nano **8**, 6788 (2014).

[26] N. Krane, C. Lotze, and K. J. Franke, Surf. Sci. **678**, 136 (2018).

[27] M. J. Frisch *et al.*, "GAUSSIAN09" (Gaussian, Inc., Wallingford CT, 2009).

[28] J. Bardeen, Phys. Rev. Lett. **6**, 57 (1961).

[29] N. Kocić, S. Decurtins, S.-X. Liu, and J. Repp, J. Chem. Phys. **146**, 092327 (2017).

[30] A. Laturia, M. L. Van de Put, and W. G. Vandenberghe, npj 2D Mater. Appl. **2**, 6 (2018).

[31] L. Gross, B. Schuler, F. Mohn, N. Moll, N. Pavliček, W. Steurer, I. Scivetti, K. Kotsis, M. Persson, and G. Meyer, Phys. Rev. B **90**, 155455 (2014).

[32] D. Z. Gao, J. Grenz, M. B. Watkins, F. Federici Canova, A. Schwarz, R. Wiesendanger, and A. L. Shluger, ACS Nano **8**, 5339 (2014).

[33] C. Wagner, M. F. B. Green, P. Leinen, T. Deilmann, P. Krüger, M. Rohlfing, R. Temirov, and F. S. Tautz, Phys. Rev. Lett. **115**, 026101 (2015).

[34] J. L. Neff and P. Rahe, Phys. Rev. B **91**, 085424 (2015).

List of Abbreviations

AFM	Atomic force microscopy/microscope
Au	Gold
BTTT	2,5-bis(3-dodecylthiophen-2-yl)thieno[3,2-b]-thiophene
CB	Conduction band
CBM	Conduction band minimum
DFT	Density functional theory
DoS	Density of States
fcc	Face-centered cubic
GGA	Generalized gradient approximation
hcp	Hexagonal closed-packed
HOMO	Highest occupied molecular orbital
LDA	Local density approximation
LDoS	Local density of states
LN_2	Liquid nitrogen
LUMO	Lowest unoccupied molecular orbital
Mo	Molybdenum
OES	Occupied edge state
S	Sulfur
SPM	Scanning probe microscopy/microscope
STM	Scanning tunneling microscopy/microscope
STS	Scanning tunneling spectroscopy
TMD	Transition metal dichalcogenide
UES	Unoccupied edge state
UHV	Ultra high vaccum
VB	Valence band
VBM	Valence band maximum
vdW	van der Waals

Acknowledgments

First of all, I want—of course—thank Katharina Franke. Not only for allowing me to work and do science in her group, but also for supporting me in my research, while also giving me the freedom to do it on my own. I can't think of a higher praise to a supervisor, than to thank her, not for guidance, but for teaching me everything I needed to know, in order to find my own way through the mist of scientific research. I hope these words suffice, to express my gratitude.

Next I want to thank Chris. The problem is, that I want to avoid writing another dozen pages, so please imagine the long list I have to thank you for. Starting from all the fruitful discussions and crazy brainstorming, enduring my long monologues (which sometimes ended with me answering my own questions) or the great times in the lab. There is simply too much to thank you for and it is pretty safe to say, that this whole work (or basically any other work in this group) would not have been possible without you .

Then there are of course my long term office mates Olof and Micha. I really enjoyed the time in that office, with all the fun and teasing and loud music (looking at you Olof ;P). And sorry Micha for continuously breaking spectra fox :'(

Also a huge thank you to my students Julia, Max and Kristina, who contributed in one way or the other to this work. In especially to Julia, for living through the many frustrating hours filled with LabView and Princton Instruments. A special thank goes to Gaël with whom I had many discussions about the plethora of peaks that MoS_2 provided us with. We were lost in the forest (of peaks), but somehow it all makes sense now. Moreover, I want to thank the other Nils of the group for patiently telling me what I am allowed to do in quantum mechanics and what not. И спасибо, Сергей. Ты пришлось пережить выносить мою попытку говорить по-русски (and I probably butchered these sentences too). Keep the AFM and MoS_2 flag flying — proud and high. And of course all the other (ex-)members of the coffee/cake/volleyball/ice cream club or whatever other club there might be: Asieh, Ben, Daniela, Eva, Gelavizh, Idan, Laëtitia, Nino, Paul, Rika, Rory, and Tobi.

A special thank will go to Jörg and the ECM Technica 4 Profi, for all the fascinating discussions, relaxing chitchat, occasional IT support and stimulants for the central nervous system to keep me going.

In the end I want to thank my family, who always supported me on this long journey, that basically started in 2007. I am so glad to be a part of it and I will stop here, before it gets soppy. And finally I want to thank Jara. For finally being here and only sometimes there ;)

Selbstständigkeitserklärung

Hiermit erkläre ich, dass diese Dissertation von mir selbständig verfasst wurde. Sämtliche Hilfsmittel und Veröffentlichungen anderer auf die ich zurückgegriffen habe wurden entsprechend angegeben. Des Weiteren versichere ich, dass diese Arbeit in keinem vorhergehenden Promotionsverfahren eingereicht wurde.

_____

List of Titles of the Publications Presented in this Work

- **Electronic Structure and Luminescence of Quasi-Freestanding MoS_2 Nanopatches on Au(111)**
  Nano Letters 16, 5163 (2016)

- **Moiré structure of MoS_2 on Au(111): Local structural and electronic properties**
  Surface Science 678, 136 (2018)

- **High Resolution Vibronic Spectra of Molecules on Molybdenum Disulfide Allow for Rotamer Identification**
  ACS Nano 12, 11698 (2018)

- **Mapping the perturbation potential of metallic and dipolar tips in tunneling spectroscopy on** MoS_2
  Physical Review B 100, 035410 (2019)